THESIS FOR THE DEGREE OF LICENTIATE OF ENGINEERING

Nanowire Superinductors

DAVID NIEPCE

Department of Microtechnology and Nanoscience (MC2)

Quantum Technology Laboratory

CHALMERS UNIVERSITY OF TECHNOLOGY

Göteborg, Sweden 2018

Nanowire Superinductors
DAVID NIEPCE

Technical Report MC2-392
ISSN 1652-0769

Quantum Technology Laboratory
Department of Microtechnology and Nanoscience (MC2)
Chalmers University of Technology
SE-412 96 Göteborg
Sweden
Telephone: +46 (0)31-772 1000

Chalmers Reproservice
Göteborg, Sweden 2018

Nanowire Superinductors
Thesis for the degree of Licentiate of Engineering
DAVID NIEPCE
Department of Microtechnology and Nanoscience (MC2)
Chalmers University of Technology

Abstract

In this thesis, we demonstrate that a disordered superconductor with a high kinetic inductance can realize a low microwave loss, non-dissipative circuit element with an impedance greater than the quantum resistance ($R_Q = h/4e^2 \simeq 6.5\,\mathrm{k}\Omega$). This element, known as a superinductor, can produce a quantum circuit where charge fluctuations are suppressed.

We have fabricated and characterized 20 nm thick niobium-nitride nanowires with a width of 40 nm, implementing a superinductance with impedance $Z = 6.795\,\mathrm{k}\Omega$. We demonstrate internal quality factors $Q_i = 2.5 \times 10^4$ at single photon excitation, which is significantly higher than values reported in devices with similar materials and geometries. Moreover, we show that the dominant dissipation in our nanowires is not an intrinsic property of the disordered films, but can instead be fully understood within the well-studied framework of two-level systems.

Keywords: Nanowire, Superinductance, Superinductor, Resonator, TLS, Disordered Superconductors

Acknowledgements

I would like to express my sincere appreciation to everyone who has made this thesis possible. First and foremost, I wish to thank my supervisor, Jonas Bylander, for giving me the opportunity of carrying out this research project, for his constant support, his enthusiasm and his confidence in my work.

I am indebted to you, Jonathan Burnett, for your invaluable input and all the long hours we have spent together in the lab. Also thank you for the swift and insightful proof reading of this manuscript. Thank you, Sergey, for your valuable feedback on my work. Thank you to all the present and past members of QDP, QTL and in particular to all the members of the Equip research group: Per, Ben, Ida, Andreas, Maria, Gustav, Yong, Marina, Laure, Arsalan, Michael, Philip, Thomas and Seçkin for creating such a great work atmosphere. Special mention to Anita for carefully proof reading the fabrication chapter and to Marco for seeding some valuable last minute simulation !

I am also grateful toward Henrik, Johan, Mats, Marcus, Niclas, Bengt and the rest of the staff of the Nanofabrication Laboratory clean room for their help, input and support. Thank you also, Lars, for your help in the workshop and always putting up with us with our last minute machining jobs and back of the envelope designs...

Last but not least, I would like to thank my friends and family. Thank you for all your support and for always being there for me. Oh, and Chris, believe it or not, but your recurrent "Are you done yet ?" actually helped to keep the procrastination away !...

David Niepce, Göteborg, April 2018

List of Publications

This thesis is based on the work containted in the following appended papers:

Paper A D. Niepce, J. Burnett and J. Bylander. High Kinetic Inductance NbN Nanowire Superinductors. arXiv: 1802.01723

Other papers that are outside of the scope of this thesis:

Paper I J. Burnett, A. Bengtsson, D. Niepce and J. Bylander. Noise and loss of superconducting aluminium resonators at single photon energies. *Journal of Physics: Conference Series* **969**: 012131, 2018

List of Symbols

Constants

h	Planck constant	$h \simeq 6.626 \times 10^{-34}\,\mathrm{J\,s}$
$\hbar$	Reduced Planck constant	$h/2\pi \simeq 1.054 \times 10^{-34}\,\mathrm{J\,s}$
e	Elementary charge	$e \simeq 1.602 \times 10^{-19}\,\mathrm{C}$
m_e	Mass of an electron	$m_e \simeq 9.109 \times 10^{-31}\,\mathrm{kg}$
c	Speed of light in vacuum	$c \simeq 2.998 \times 10^{8}\,\mathrm{m\,s^{-1}}$
k_B	Boltzmann's constant	$k_B \simeq 1.380 \times 10^{-23}\,\mathrm{J\,K^{-1}}$
μ_0	Vacuum permeability	$4\pi \times 10^{-7}\,\mathrm{H\,m^{-1}}$
ϵ_0	Vacuum permittivity	$8.854 \times 10^{-12}\,\mathrm{F\,m^{-1}}$
R_K	Von Klitzing constant	$h/e^2 \simeq 25.812\,\mathrm{k\Omega}$
R_Q	Superconducting resistance quantum	$h/4e^2 \simeq 6.453\,\mathrm{k\Omega}$
γ	Euler-Mascheroni constant	$\gamma \simeq 5.772 \times 10^{-1}$
Φ_0	Magnetic flux quantum	$h/2e \simeq 2.067 \times 10^{-15}\,\mathrm{Wb}$

Chapter 1: Introduction

L_{nw}	Inductance per length of the nanowire
C_{nw}	Capacitance per length of the nanowire
Z_{nw}	Impedance of the nanowire

Chapter 2: Disordered Superconductors

T_c	Critical temperature of a superconductor
τ	Average time between scattering events
σ_n	Normal electrons conductivity (two-fluid model)
σ_s	Superconducting electrons conductivity (two-fluid model)
ω	Angular frequency
n_n	Density of normal electrons
n_s	Density of superconducting electrons
J_n	Current density of normal electrons (two-fluid model)
J_s	Current density of superconducting electrons (two-fluid model)
ε_f	Fermi energy
k_F	Fermi wavevector
v_F	Fermi velocity
ρ_n	Metal density of states
l	Electron mean free path
$\vec{E}$	Electric field
$\vec{B}$	Magnetic field
$\vec{H}$	Auxiliary magnetic field
$\vec{A}$	Magnetic vector potential

λ_L	London penetration depth
ψ	Superconducting order parameter
φ	Superconducting phase
F	Free energy
ξ_{GL}	Ginzburg-Landau coherence length
κ	Ginzburg-Landau parameter
H_c	Critical field
H_{c1}	Lower critical field
H_{c2}	Upper critical field
ρ_s	BCS density of states
Δ	Superconducting gap
Δ_0	Superconducting gap at zero temperature
ω_D	Debye frequency
ξ_0	BCS coherence length
$k_F l$	Ioffe-Regel parameter
λ_{dirty}	London penetration depth (dirty limit)
Λ	Effective penetration depth
L_m	Magnetic inductance (internal)
L_k	Kinetic inductane
E_{mag}	Magnetic energy
E_{kin}	Kinetic energy
Z_S	Surface impedance
δ	Skin depth
σ_1	Real part of Mattis-Bardeen conductivity
σ_2	Imaginary part of the Mattis-Bardeen conductivity
R_N	Normal state resistance
σ_{2D}	Fluctuations paraconductivity
T_{BKT}	Berezinskii-Kosterlitz-Thouless ordering temperature
U_{VAP}	Vortex-Antivortex Pair potential energy
$A(T)$	Vortex polarizability
$\mu_c(T)$	Vortex core energy
$\rho(T)$	Unbound VAP resistivity

Chapter 3: Superconducting Microwave Resonators

S	Scattering parameters matrix
S_{11}	Reflection coefficient
S_{21}	Transmission coefficient
Z_0	Transmission line characteristic impedance
γ	Propagation constant
α	Real part of the propagation constant
β	Imaginary part of propagation constant

Z_{in}	Input impedance
v_{ph}	Phase velocity
ω_0	Resonance frequency
$\Delta\omega$	Frequency detuning
Q_i	Internal quality factor
Q_c	Coupling quality factor
Q_l	Loaded quality factor
M	Mutual inductance
$\langle E_{int} \rangle$	Resonator internal energy
$\langle n \rangle$	Average number of photons
P_{in}	Input power
F	TLS Filling factor (participation ratio)
$F \tan \delta^i_{TLs}$	Intrinsinc loss tangent
R_{ESR}	Capacitor equivalent series resistor
P_γ	TLS switching rate ratio
γ_{min}	Minimum TLS switching rate
γ_{max}	Maximum TLS switching rate
$1/Q_{TLS}$	TLS induced loss
$1/Q_{qp}$	Quasiparticle induced loss
$1/Q_{disorder}$	Disorder induced loss
$1/Q_{rad}$	Radiation loss

Chapter 4: Nanofabrication Techniques

γ	Resist contrast
D_0	Threshold dose
D_1	Clearing dose
λ_e	De Broglie wavelength
D	EBL exposure dose
τ_{dwell}	EBL beam dwell time
I_{beam}	EBL beam current
δ	EBL beam step

Chapter 5: Measurement Techniques

A	Phase modulated signal
β	Phase modulation depth
Ω	Modulation frequency
ε	Error signal

V_{TLS}	TLS host volume
ε_{TLS}	Permittivity of the TLS host material
ε	Permittivity
Γ_S	Phase slip rate
R_H	Hall coefficient

List of Figures

List of Tables

Contents

Chapter 1

Introduction

Recent years have seen tremendous progress in the preservation of quantum coherent states in superconducting circuits. This progress has been driven by both device and materials engineering, and it is now common to see a variety of superconducting qubit architectures with relaxation times around 100 µs [1, 2]. Despite this progress, short dephasing times remain a significant problem in many quantum information processing architectures. Typically dephasing is understood to arise from charge or flux fluctuations and identifying the origin of these fluctuators is a topic of ongoing research [3, 4].

Charge fluctuations can be suppressed by embedding the superconducting circuit in a high-impedance microwave environment – a *superinductance* – which is a non-dissipative, inductive circuit element with impedance greater than the quantum resistance ($R_Q = h/4e^2 \simeq 6.5\,\mathrm{k}\Omega$) and low microwave losses. Purely electromagnetic inductances are incompatible with such requirements: due to unavoidable shunt capacitance, they are always bounded by the impedance of free space $\sqrt{\mu_0/\epsilon_0} \simeq 377\,\Omega$.

The impedance of free space limit can be surpassed by exploiting the kinetic inductance of a superconductor. Recently, an array of Josephson junctions was used to realize a superinductance [5, 6]. Embedding a superconducting qubit within a superinductance is known as a fluxonium [7, 8], these qubits have demonstrated the suppression of charge noise sensitivity to show relaxation times of the order of milliseconds [1]. However, these circuits also exhibit incredibly short dephasing times as low as 150 ns due to flux noise [9]. However, the fluxonium has a rich energy spectrum which can reveal low frequency qubit modes where gradient of qubit energy against flux is flat [10].

An attractive alternative to Josephson junction arrays is offered by the high kinetic inductance of strongly disordered superconducting thin films. When patterned into a nanowire, such films can produce inductances which are orders of magnitude higher than an ordinary geometric inductance, while keeping the capacitance arbitrarily small. Importantly, this approach does not feature the complex dynamics of a Josephson junction array and could therefore be insightful for examining the dephasing properties of superinductor-based qubits.

Previously, a superconducting nanowire based approach was overlooked as a variety of superconducting nanowire based circuits were found to exhibit significant internal dissipation [11, 12]. However, it has recently been shown that it is possible to fabricate superconducting nanowires embedded within resonators that do not exhibit high dissipation [13]. In addition, 100 nm wide resonators made from low-disorder superconductors have also shown high quality factors at the relatively high temperature of 300 mK [14]. Consequently, with sufficient material engineering, a nanowire patterned

from a strongly disordered superconducting thin film should be a viable route for realizing a superinductor.

In this work, we demonstrate a nanowire-based superinductor with an impedance of $Z_{nw} = \sqrt{L_{nw}/C_{nw}} = 6.795\,\mathrm{k}\Omega$. We developed a process based on dry etching a hydrogen silsesquioxane (HSQ) mask to pattern a 20 nm thick, strongly disordered film of niobium nitride (NbN) into a 40 nm wide and $\sim$680 µm long nanowire. These dimensions ensure a large inductance while exponentially suppressing unwanted phase slips in our devices [12]. We study both the microwave transmission and DC transport properties of several nanowires to characterize their impedance and microwave losses. These nanowire-based superinductors demonstrate a single photon quality factor of 2.5×10^4, which is comparable to JJA-based superinductors [5]. We find that the dominant loss mechanism is parasitic two level systems (TLS), which is exacerbated by the unfavorable TLS filling factor [15] that arises from the small dimensions required to obtain a high impedance.

Chapter 2

Disordered Superconductors

On April 8, 1911, while studying the resistance of solid mercury at cryogenic temperatures using liquid helium as refrigerant, Heike Kamerlingh Onnes observed that the resistance abruptly disappeared below a critical temperature T_c of 4.2 K [16]. This phenomenon, known as *superconductivity*, was soon observed in several other metals such as lead, in 1913 ($T_c = 7\,\mathrm{K}$) or niobium nitride, in 1941 ($T_c = 16\,\mathrm{K}$). About twenty years later, in 1933, Meissner and Ochsenfeld discovered that superconductors are ideal diamagnets that expel applied magnetic fields [17], and in 1935, Rjabinin and Shubnikov experimentally discovered the existence of type-II superconductors [18].

In 1934, Gorter and Casimir proposed the classical *two-fluid model* [19] to describe the electrodynamics of a superconductor at a finite temperature. A year later, the Meissner effect was phenomenologically described by the London brothers [20]. In 1950, Ginzburg and Landau proposed a semi-classical theory of the superconducting state [21] based on Landau's previously established theory of second-order phase transitions. This model was later extended by Abrikosov [22] and Gor'kov [23], in 1957 and 1959 respectively. Finally, a full microscopic quantum description of the superconducting state was published in 1957 by Bardeen, Cooper and Schrieffer (BCS) [24] and in 1958, Mattis and Bardeen extended the BCS theory and proposed the *Mattis-Bardeen theory* [25] to describe the electrodynamics of superconductors.

This chapter aims to give the reader a brief overview of the concepts of superconductivity relevant to this work. We start by reminiscing the key results of the various theories involved in the description of the superconducting state and then put them in the context of disordered superconductors.

2.1 Electronic Transport in Metals

2.1.1 Drude Conductivity

The conductivity of a normal metal can be derived using the Drude model where an electric field is applied to an electron gas [26–28]. The electrons respond to the field by being accelerated and gaining momentum until they scatter off an ion and are given some new random direction and velocity. The scattering process is characterized by an average time τ between scattering events and after many scattering events, the electrons will have some average momentum in the direction of the field. The derivation of the Drude model

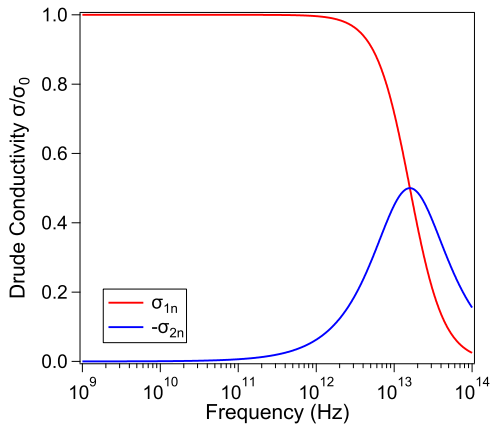

Figure 2.1: Drude conductivity for a typical metal ($\tau = 1 \times 10^{-14}$ s) as a function of frequency. The imaginary part σ_{2n} is negligible for frequencies below 1 THz.

leads to the following expression for the conductivity at a frequency ω

$$\sigma_n(\omega) = \frac{\sigma_0}{1 + i\omega\tau} = \frac{\sigma_0}{1 + \omega^2\tau^2}\,(1 - i\omega\tau) = \sigma_{1n} - i\sigma_{2n} \tag{2.1}$$

where $\sigma_0 = n_n e^2\tau/m_e$ with e the elementary charge, m_e the effective electron mass and n_n the electron density. In normal metals, the collision time is typically $\tau \simeq 1 \times 10^{-14}$ s, therefore, for frequencies < 1 THz, the term $\omega^2\tau^2$ is very small and can be ignored as shown in Fig. 2.1.

2.1.2 Drude-Sommerfeld Model

The Drude-Sommerfeld model, also known as the *free electron model*, is the simplest quantum mechanical description of the behaviour of charge carriers in a metallic solid. Introduced by Sommerfeld in 1927 [29], this model combines the classical Drude model with the quantum mechanical Fermic-Dirac statistic. It consists of the solutions of the time-independent Schrödinger equation for a gas of N free electrons, for which the electron-electron and electron-lattice interactions are neglected, confined in a space of volume V. This leads to the well established dispersion relation of the free electron model

$$\varepsilon(\vec{k}) = \frac{\hbar^2\vec{k}^2}{2m_e} \tag{2.2}$$

where ε is the energy and $\vec{k}$ is the wavevector. The *Fermi energy* ε_F, which corresponds to the energy of the highest populated level, can be derived by counting the number of

states in the sphere of radius k_F. Accounting for spin, we get

$$k_F = \left(3\pi^2 n_n\right)^{1/3} \tag{2.3}$$

with $n_n = N/V$, the density of electrons. By using Eq. 2.2 and Eq. 2.3, we can write

$$\varepsilon_F = \frac{\hbar^2}{2m_e}\left(3\pi^2 n_n\right)^{2/3} \tag{2.4}$$

Finally, the density of states, defined as the number of states per unit energy, is given by

$$\rho_n(\varepsilon) = \frac{\mathrm{d}n_n}{\mathrm{d}E} = \frac{m_e}{\pi^2\hbar^3}\sqrt{2m_e\varepsilon} \tag{2.5}$$

If we consider a similar scattering process as in the Drude model, characterized by an average time τ between scattering events, we can introduce the *mean free path* l, defined by the average distance an electron travels between successive scattering events. The mean free path is given by

$$l = v_F\tau \tag{2.6}$$

where $v_F = \sqrt{2\varepsilon_F/m_e}$ is the Fermi velocity.

Despite its simplicity (the crystal lattice and resulting band structure are not taken into account), this model is able to describe many important properties of metals.

In the case of the NbN thin-films considered in this work, the free electron model is of particular interest to asses the quality and level of disorder of the fabricated films (see sections 2.3 and 6.2.2 for more details).

2.2 Low-Temperature Superconductivity

2.2.1 The Two-Fluid Model

As stated previously, the two-fluid model is a classical description of the electrodynamics of a superconductor at a finite temperature: when the superconductor undergoes its transition into the superconducting state ($T < T_c$) the population of electrons is divided in two parts. One population of density n_n consists of normal single electrons, known as quasi-particles, subject to scattering and thus exhibiting losses. The other population of

density n_s consists of superconducting electrons, known in this model as *superelectrons*, immune to scattering effects hence exhibiting no loss. [1]

In the two fluid model, the current in a superconductor follows two paths: one path through the superconducting electrons (n_s) and one through normal electrons (n_n). The total density of charge carriers in the material is given by $n = n_s + n_n$ and the ratio n_s/n is given by

$$\frac{n_s}{n} = 1 - \left(\frac{T}{T_c}\right)^4 \tag{2.7}$$

The conductivity σ_n of the normal electrons is described by equation 2.1. The superconducting electrons do not scatter, therefore by taking $\tau \to \infty$, equation 2.1 leads to the conductivity σ_s of the superconducting electrons:

$$\sigma_s = -i\frac{n_s e^2}{\omega m_e} \tag{2.8}$$

This leads to the general expression of the conductivity for a superconductor in the two-fluid model

$$\sigma = \frac{n_n e^2 \tau}{m_e(1+\omega^2\tau^2)} - i\left(\frac{n_n e^2 \omega\tau^2}{m_e(1+\omega^2\tau^2)} + \frac{n_s e^2}{\omega m_e}\right) \tag{2.9}$$

In the DC regime ($\omega = 0$) at $T = 0\,\mathrm{K}$, the conductivity is purely imaginary and accounts for the zero resistance effect for which superconductors are famous. However, as we move to higher temperatures or frequencies, an increase of σ_n along with the decrease of σ_s means that a larger fraction of the current is shunted through the resistive path compared to lower temperatures or frequencies: the superconductor will exhibit losses as the temperature or frequency increases. Moreover, the inertia of the superconducting electrons produces a reactance leading to a large impedance at high frequencies: this is the *kinetic inductance*. Figure 2.2 gives a schematic representation of the two current paths.

In the microwave regime, where $\omega\tau \ll 1$, equation 2.9 can be simplified into

$$\sigma = \sigma_1 - i\sigma_2 = \frac{n_n e^2 \tau}{m_e} - i\frac{n_s e^2}{\omega m_e} \tag{2.10}$$

where σ_1 accounts for the conductivity of normal electrons and σ_2 for the superconducting electrons. Moreover, since for $T > T_c$ all electrons are in the normal state, we have

$$n_n = n \quad \text{and } \sigma = \sigma_n = \frac{n e^2 \tau}{m_e} \tag{2.11}$$

[1] In the two-fluid model, no other assumption is taken on the nature of the superelectrons. The concept of electrons paired in Cooper pairs is introduced by Cooper in 1956 [30].

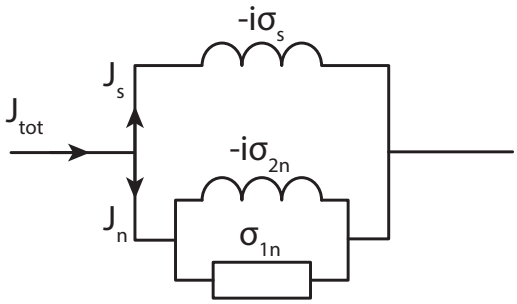

Figure 2.2: Two-fluid model current paths equivalent circuit. The supercurrent (J_s) flows through an inductive current path with zero loss. The normal electrons current (J_n) path takes the form of a resistive path in parallel with an inductive path accounting for both the real (σ_{1n}) and imaginary components (σ_{2n}) of the normal conductivity.

In the same way, at $T = 0\,\mathrm{K}$, all the electrons are in the superconducting state and we have

$$n_s = n \quad \text{and } \sigma = \sigma_s = \frac{ne^2}{\omega m_e} \tag{2.12}$$

Because the two-fluid model relies on the only assumption that two different populations of electrons exist in a superconductor, it is insufficient to explain the properties of superconductivity other than the absence of resistance. However, despite it's simplicity, the two-fluid model gives a good qualitative picture of the electrodynamics of superconductors.

The concept of kinetic inductance introduced by the two-fluid model will be further expanded in section 2.3.

2.2.2 The London Theory

Two years after the discovery of the Meissner effect, F. and H. London proposed a phenomenological model describing the ideal diamagnetism of a superconductor. This model introduces the *London equations*, which complement Maxwell's equations, to describe the behavior of fields and currents in and around a superconductor [20]:

$$\frac{\partial \vec{J}_s}{\partial t} = \frac{n_s e^2}{m_e}\vec{E} \tag{2.13}$$

$$\nabla \times \vec{J}_s = -\frac{n_s e^2}{m_e}\vec{B} \tag{2.14}$$

where $\vec{E}$ and $\vec{B}$ are the electric and magnetic fields respectively and $\vec{J}_s$ is the superconducting current density.

In contrast to Ohm's law, the first London equation (Eq. 2.13) describes a frictionless flow of superconducting current and implies that no electric field exists in the superconductor in the stationary state. The second equation (Eq. 2.14) describes the ideal diamagnetism of superconductors. By applying Ampère's law to the second London equation, we get

$$\nabla \times \vec{B} = \frac{\mu_0 n_s e^2}{m_e} \vec{B} = 1/\lambda_L^2 \vec{B} \quad \text{with } \lambda_L = \sqrt{m_e/\mu_0 n_s e^2} \tag{2.15}$$

The solution of this differential equation is a magnetic field that decays inside the superconductor on a length scale λ_L, known as the *London penetration depth*. In other words, any external magnetic field is exponentially screened inside the superconductor over a characteristic distance λ_L. Because of the temperature dependence of n_s, the London penetration depth also depends on temperature. Using Eq. 2.7, we get

$$\lambda_L(T) = \lambda_L(0) \left[1 - \left(\frac{T}{T_c} \right)^4 \right]^{-1/2} \tag{2.16}$$

with $\lambda_L(0) = \sqrt{m_e/\mu_0 n e^2}$, the London penetration depth at 0 K ($n_s = n$ at 0 K).

2.2.3 The Ginzburg-Landau Theory

In 1950, Ginzburg and Landau (GL) applied the results of Landau's mean field theory in the context of superconductivity. The GL theory introduces a pseudo wavefunction $\psi = \sqrt{n_s} e^{i\varphi}$ (the *order parameter*) and postulates that if ψ is small and varies slowly in space, the free energy of the superconductor can be expanded into a series of ψ^2:

$$F = F_n + \alpha |\psi|^2 + \frac{\beta}{2} |\psi|^4 + \frac{1}{2m_e} \left| (-i\hbar\nabla - 2e\vec{A})\psi \right|^2 + \frac{|\vec{B}|^2}{2\mu_0} \tag{2.17}$$

where F_n is the free energy of the normal state, $\vec{A}$ is the magnetic vector potential and α and β are parameters. Minimizing the free energy with respect to variations in the order parameter and the vector potential leads to the *Ginzburg-Landau equations*:

$$\alpha\psi + \beta|\psi|^2\psi + \frac{1}{2m_e} \left(-i\hbar\nabla - 2e\vec{A} \right)^2 \psi = 0 \tag{2.18}$$

$$\nabla \times \vec{B} = \mu_0 \vec{j} \quad \text{with } \vec{j} = \frac{2e}{m_e} \operatorname{Re} \left[\psi^* \left(-i\hbar\nabla - 2e\vec{A} \right) \psi \right] \tag{2.19}$$

The solutions to Eq. 2.18 and 2.19 rely on two characteristic length scales: in the superconductor, magnetic fields are exponentially suppressed and decay over a penetration depth λ_L, as introduced by the London theory. The second characteristic length scale is the *coherence length* ξ_{GL}, given by

$$\xi_{GL} = \sqrt{\frac{\hbar^2}{4m_e|\alpha|}} \tag{2.20}$$

The coherence length reflects the quantum mechanical character of the GL-theory and represents the minimum spatial length scale over which the order parameter varies. The ratio of these two length scales, $\kappa = \lambda_L/\xi_{GL}$, is known as the Ginzburg-Landau parameter.

Type-I and Type-II Superconductors

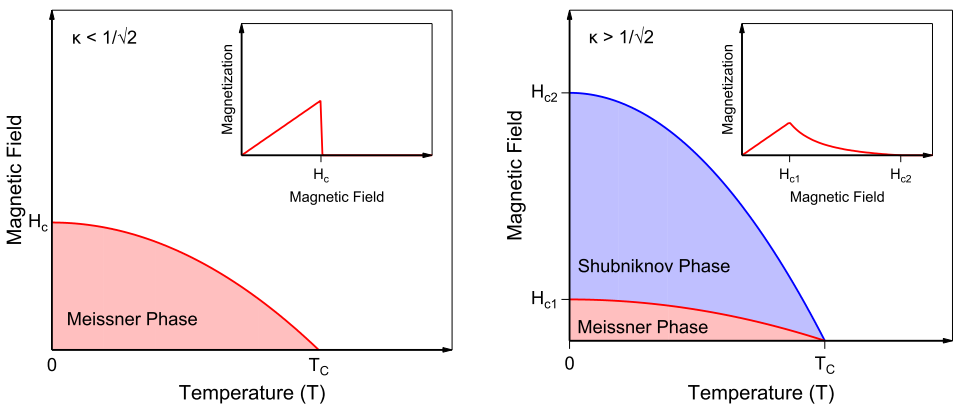

Figure 2.3: Phase diagram of a type-I **(left)** and type-II **(right)** superconductors. The insets show the magnetization as a function of the magnetic field for each case.

The GL-theory suggests the existence of two different types of superconductors depending on the energy of the interface between the normal and superconducting states.

When $\kappa < 1/\sqrt{2}$, the free energy at the interface is positive and it is therefore energetically favorable to form either a continuous superconducting or a continuous normal state: when in the superconducting phase, the superconductor completely rejects magnetic fields (Meissner effect), until a critical field H_c is reached and superconductivity is abruptly destroyed via a first order phase transition. These superconductors are known as type-I superconductors.

On the other hand, when $\kappa > 1/\sqrt{2}$, the free energy is negative. In this case, it becomes energetically favorable to form a composite state of the normal and superconducting phase for a wide range of applied magnetic fields. These superconductors, known as type-II, are

characterized by the existence of two critical fields: H_{c1}, below which no magnetic field penetrates the superconductor (Meissner phase). When the applied field becomes larger than H_{c1}, magnetic fields start to penetrate the superconductor, until another critical field H_{c2} is reached and the superconducting phase is completely destroyed. A schematic summary of the phase diagram and magnetization of type-I and type-II superconductors is shown in Fig. 2.3.

Abrikosov showed that the magnetic field penetrates type-II superconductors in the shape of quantized flux lines, known as *vortices*. The phase where vortices and the superconducting state cohabit is known as the *mixed state* or *Shubnikov phase*. Type-II superconductors are of particular interest in the laboratory as they exhibit very large critical fields ($\sim 16\,\mathrm{T}$ in the case of NbN) which allows for the preservation of superconducting state under a wide range of magnetic fields, however, as it will be discussed later, vortices can be a source of unwanted dissipation and special care should be taken to minimize their influence.

2.2.4 The BCS Theory

In 1956, Cooper showed [30] that in a metal, an arbitrarily small attraction between electrons can lead to the formation of a paired state of electrons with an energy lower than the Fermi energy. This bound state, known as a Cooper pair, consists of a pair of two electrons of opposite spin and momentum and is therefore of bosonic nature.

A year later, Bardeen, Cooper and Schrieffer demonstrated [24] that the electron-phonon interaction can lead to the formation of Cooper pairs below a critical temperature T_c. Moreover, they showed that due to their bosonic nature, the Cooper pairs tend to condense in the same coherent quantum state. This quantum-statistical condensation is accompanied by the development of an energy gap Δ around the Fermi energy and in order to break Cooper pairs, one needs to provide an energy 2Δ.

This energy gap is calculated to be, at $0\,\mathrm{K}$:

$$\frac{\Delta_0}{k_B T_c} = \frac{\pi}{e^\gamma} \simeq 1.764 \tag{2.21}$$

where k_B is the Boltzmann constant and γ is the Euler-Mascheroni constant. Moreover, the BCS theory predicts the dependence of the value of the energy gap on the temperature T with

$$\frac{1}{\rho_n} = \int_0^{\hbar\omega_D} \frac{\tanh\left[(\xi^2+\Delta^2)^{1/2}/2k_BT\right]}{(\xi^2+\Delta^2)^{1/2}} d\xi \tag{2.22}$$

where ω_D is the Debye frequency, which corresponds to the cut-off frequency above which no lattice vibration can occurs. Unfortunately, Eq. 2.22 has no analytical solution, but

the values of $\Delta(T)$ can be computed numerically [31]. Near T_c, the value of the energy gap can be approximated by

$$\Delta(T) \simeq 3.2 k_B T_c \left(1 - \frac{T}{T_c}\right)^{1/2} \tag{2.23}$$

Additionally, the BCS density of states is given by

$$\rho_s(\varepsilon) = \begin{cases} \dfrac{\varepsilon}{\sqrt{\varepsilon^2 - \Delta^2}} & \varepsilon > \Delta \\ 0 & \varepsilon < \Delta \end{cases} \tag{2.24}$$

Finally, like the London and GL theories, the BCS theory introduces a characteristic length scale, known as the BCS coherence length and given by

$$\xi_0 = \frac{\hbar v_F}{\pi \Delta_0} \tag{2.25}$$

All these length scales are key for understanding the influence of disorder on the properties of a superconductor, which will be discussed more in detail in section 2.3 below.

Weakly- and Strongly-coupled Superconductors

The BCS theory revealed the importance of the electron-phonon interaction for the existence of the superconducting state, however, the results are derived in the so-called *weak coupling* limit, where $\hbar\omega_D \gg k_B T_c$.

Niobium nitride is experimentally found to be a strongly coupled superconductor [32] and therefore does not fall under the case described by the BCS theory. The *strong coupling* limit ($\hbar\omega_D \ll k_B T_c$) has been studied by Thouless in details [33] and he concluded that the results of the weak-coupling BCS theory also apply for a strongly coupled superconductor, barring an adjustment of the prefactors in Eq. 2.21 and 2.23. In the case of NbN, we have

$$\begin{aligned} &\Delta(T) \simeq 3.45 k_B T_c \left(1 - \tfrac{T}{T_c}\right)^{1/2} \quad \text{near } T_c \\ &\Delta_0 = 2.08 k_B T_c \end{aligned} \tag{2.26}$$

Additionally, Thouless showed that the energy gap of a superconductor (in both the weak and strong coupling limit) can be self-consistently calculated from

$$\frac{\Delta(T)}{\Delta_0} = \tanh\left(\frac{T_c}{T}\frac{\Delta(T)}{\Delta_0}\right) \tag{2.27}$$

2.3 Disordered Superconductors

2.3.1 Length Scales Parameter Space

In the previous sections, we have introduced three characteristic length scales: the electron mean free path l, the London penetration depth λ_L and the BCS coherence length ξ_0. These length scales define a broad parameter space inside which various different regimes can be identified. In the context of this work, we will focus on the *local dirty limit*, where $l \ll \xi_0 \ll \lambda_L$. An in-depth review of the different regimes can be found in [34].

As detailed in the experimental results (see chapter 6), with values of l of the order of 100 pm, ξ_0 of the order of 200 nm and λ_L of the order of 1 µm, the NbN thin films considered in this work fall well inside the local dirty limit.

2.3.2 Ioffe-Regel Criterion

The study of crystalline materials has always played a prominent role in solid state physics. Perfect crystallinity introduces considerable simplifications in the formulation of theories for the physical properties, however, in many practical applications, a certain degree of disorder is present. Defects, vacancies or dislocations, that are frequently observed in real materials, are defined as *weak disorder* and are usually treated as a perturbation of the perfect crystalline order. On the other hand, *strong disorder* is characterized by an absence of long range translational order and signifies a marked departure from crystalline order.

Ioffe and Regel introduced a criterion that qualitatively quantifies the level of disorder in a system [35], knows as the *Ioffe-Regel parameter* and defined by the product $k_F l$ of the Fermi wavevector and the electron mean free path. Moreover, they predicted that when $k_f l \simeq 1$, a metal-insulation transition should be observed. An increasing amount of disorder translates into a diminishing electron mean free path which leads to a gradual localization of charge carriers [36] until an insulating state is reached (see section 2.4 for more details).

In a superconductor, disorder leads a competition between two interactions: on one hand, superconductivity is a manifestation of long-range phase coherence between electron pair states, however, on the other hand, localization involves a limitation of the spatial extent of the wavefunctions and should inhibit such pairing. Therefore, we can anticipate that superconductivity should disappear as disorder increases and states become localized. Such a phenomenon is known as the superconductor to insulator transition (SIT) and was reported as early as 1978 by Dynes [37], who observed that lead thin-films with resistances larger than 30 kΩ/□ were no longer superconducting (see Fig. 4 in [37]).

A big challenge of this work resides in the fabrication of strongly disordered thin-films close to the SIT (with $k_F l \simeq 1$) in order to maximize the kinetic inductance (see the following sections for more details). In such regime, the thin-film becomes extremely

sensitive to the deposition parameters and careful characterization and optimization is necessary.

2.3.3 Dirty Superconductor

Strongly disordered superconductors have extremely small electron mean free path and therefore fall under the regime of the local dirty limit. In this regime, several quantities defined in the previous sections become dependent on the electron mean free path and need to be adjusted [23, 38]. Most importantly for this work, the magnetic penetration depth at $T = 0\,\mathrm{K}$ is given by

$$\lambda_{dirty}(0) = \lambda_L(0)\sqrt{\frac{\xi_0}{l}} = \sqrt{\frac{\hbar}{\pi\mu_0\Delta_0\sigma_n}} \tag{2.28}$$

Additionally, the temperature dependence of the penetration depth is given by

$$\frac{\lambda_{dirty}(T)}{\lambda_{dirty}(0)} = \left[\frac{\Delta(T)}{\Delta_0}\tanh\left(\frac{\Delta(T)}{2k_BT}\right)\right] \tag{2.29}$$

Finally, in the limit of a thin-film ($t \ll \lambda_{dirty}$), the penetration depth is replaced by an *effective penetration depth* [38, 39]:

$$\Lambda(T) = \frac{2\lambda^2_{dirty}(T)}{t} \tag{2.30}$$

2.3.4 Kinetic Inductance

In section 2.2.1, we briefly introduced a concept known as *kinetic inductance*. Formally, kinetic inductance is the manifestation of the inertial mass of mobile charge carriers in alternating electric fields as an equivalent series inductance. In other words, in an alternating field, it takes time for the charge carriers to reach their final velocity and the current "lags" behind the voltage. Kinetic inductance is observed at very high frequencies in high carrier mobility conductors and also in superconductors at significantly lower frequencies.

In a superconductor, energy can be stored in two ways: one part is stored in the magnetic field penetrating the superconductor (with a depth λ_L). This energy depends on the geometry of the superconductor and is given by

$$E_{mag} = \int \frac{\mu_0\vec{H}^2}{2}dA = \frac{1}{2}L_mI^2 \tag{2.31}$$

A second part of the energy is associated with the kinetic energy of the Cooper pairs. We can write the kinetic energy E_{kin} of the Cooper pairs using $\vec{J}_s = n_s e \vec{v}$ with

$$E_{kin} = \int \frac{m_e n_s \vec{v}}{2} dA = \frac{m_e}{2 n_s e^2} \int \vec{J_s}^2 dA = \mu_0 \lambda_L^2 \int \vec{J_s}^2 dA = \frac{1}{2} L_k I^2 \tag{2.32}$$

where $\vec{v}$ is the average velocity of the charge carriers and L_k is the *kinetic inductance*. We can see from this last equation that an increase in density of Cooper pairs n_s leads to a decrease of the kinetic energy, reaching a minimum at $T = 0\,\mathrm{K}$. Additionally, from Eq. 2.10, we see that when the temperature increases and Cooper pairs break up into normal electrons, n_s and σ_2 decrease and n_n and σ_1 increase. For a given energy, a lower Cooper pair density forces the Cooper pairs to increase their velocity in order to provide the same supercurrent J_s, leading to a larger kinetic inductance.

The evaluation of the integrals has been derived by Doyle [40] for a superconducting strip of width w and thickness t and read as

$$L_k = \frac{\mu_0 \lambda_L}{4w} \left[\coth\left(\frac{t}{2\lambda_L}\right) + \left(\frac{t}{2\lambda_L}\right) \mathrm{cosec}^2\left(\frac{t}{2\lambda_L}\right) \right] \tag{2.33}$$

$$L_m = \frac{\mu_0 \lambda_L}{4w} \left[\coth\left(\frac{t}{2\lambda_L}\right) - \left(\frac{t}{2\lambda_L}\right) \mathrm{cosec}^2\left(\frac{t}{2\lambda_L}\right) \right] \tag{2.34}$$

Leading to the following expression for the total internal inductance

$$L_{int} = L_m + L_k = \frac{\mu_0 \lambda_L}{4w} \coth\left(\frac{t}{2\lambda_L}\right) \tag{2.35}$$

Fig. 2.4 shows a comparative plot of the magnetic and kinetic contributions to the inductance as a function of the film thickness. As the thickness decreases, the magnetic inductance is gradually suppressed while the kinetic inductance dramatically increases. In the case of a very thin superconducting strip of thickness t and width w, with $t \ll \lambda_L$, the geometric contribution is negligible, the current density is approximately constant and the kinetic inductance can immediately be calculated to

$$L_k = \frac{\lambda_L^2 \mu_0}{wt} \tag{2.36}$$

2.3.5 Surface Impedance in the Thin-Film Limit

The surface impedance Z_S is defined as the ratio of the transverse components of the electromagnetic field at the surface. It is well known that an electromagnetic field

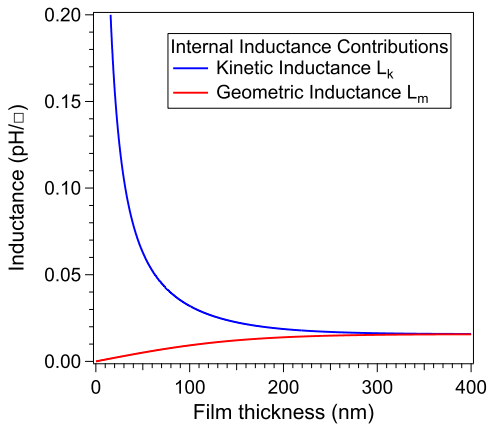

Figure 2.4: Internal inductance contributions calculated for $\lambda_L = 50\,\text{nm}$. The kinetic inductance greatly increases when the film thickness is reduced.

penetrates into a normal metal with a finite skin depth δ which can be calculated using Maxwell's equations and the local Ohm's law $\vec{J_n}(\vec{r}) = \sigma_n \vec{E}(\vec{r})$:

$$\delta = \sqrt{\frac{2}{\mu_0 \omega \sigma}} \tag{2.37}$$

This skin depth implies that the in-plane electromagnetic field components will decay exponentially inside the conductor. We can therefore write, for the electric field in the conductor:

$$E_x(z) = E_x(0) e^{-\frac{z}{\delta}(1+i)} \tag{2.38}$$

And by applying the Maxwell-Faraday equation, an expression for the magnetic field immediately follows

$$H_y(z) = \frac{1-i}{\mu_0 \omega \delta} E_x(z) \tag{2.39}$$

This finally leads to

$$Z_S = \frac{E_x(0)}{H_y(0)} = \sqrt{\frac{i\omega\mu_0}{\sigma}} \tag{2.40}$$

It was shown [41] that for a thick film ($t \gg l$) in the local dirty limit, the surface impedance of a superconductor can be simply obtained by replacing σ in Eq. 2.40 with

the conductivity from the two fluid model (Eq. 2.9). In the thin-film limit, the surface impedance expression should be modified to [41]

$$Z_S = \frac{1}{t(\sigma_1 - i\sigma_2)} \tag{2.41}$$

In the previous section, we demonstrated that in the case of a thin-film, the kinetic inductance dominates the internal inductance, therefore, if we define $Z_S = R_S + i\omega L_S$, from Eq. 2.41, we immediately get

$$R_S = \frac{\sigma_1}{t(\sigma_1^2 + \sigma_2^2)} \quad \text{and} \quad L_S \equiv L_k = \frac{\sigma_2}{t\omega(\sigma_1^2 + \sigma_2^2)} \tag{2.42}$$

Mattis-Bardeen Theory

The Mattis-Bardeen theory [25] was developed to describe the anomalous skin effect in metal and superconductors. Under the assumption that either $\xi_0 \gg \lambda_L$ or $\xi_0 \gg l$, the Mattis-Bardeen equations for the complex conductivity $\sigma(\omega) = \sigma_1 - i\sigma_2$ relative to the normal state conductivity σ_n read as:

$$\begin{aligned}\frac{\sigma_1}{\sigma_n} =& \frac{2}{\hbar\omega}\int_{\Delta}^{\infty} \frac{[f(\varepsilon) - f(\varepsilon+\hbar\omega)]\,(\varepsilon^2 + \Delta^2 + \hbar\omega\varepsilon)}{\sqrt{\varepsilon^2 - \Delta^2}\sqrt{(\varepsilon+\hbar\omega)^2 - \Delta^2}} d\varepsilon \\ &+ \frac{1}{\hbar\omega}\int_{\Delta-\hbar\omega}^{-\Delta} \frac{[1 - 2f(\varepsilon+\hbar\omega)]\,(\varepsilon^2 + \Delta^2 + \hbar\omega\varepsilon)}{\sqrt{\varepsilon^2 - \Delta^2}\sqrt{(\varepsilon+\hbar\omega)^2 - \Delta^2}} d\varepsilon\end{aligned} \tag{2.43}$$

$$\frac{\sigma_2}{\sigma_n} = \frac{1}{\hbar\omega}\int_{\max(-\Delta,\Delta-\hbar\omega)}^{\Delta} \frac{[1 - 2f(\varepsilon+\hbar\omega)]\,(\varepsilon^2 + \Delta^2 + \hbar\omega\varepsilon)}{\sqrt{\Delta^2 - \varepsilon^2}\sqrt{(\varepsilon+\hbar\omega)^2 - \Delta^2}} d\varepsilon \tag{2.44}$$

where f is the Fermi-Dirac distribution function $f(\varepsilon) = 1/(1 + \exp(\varepsilon/k_B T))$. In Eq. 2.43, the first integral represents the contribution of thermal excitations of quasi-particles. The second integral represents the creation of quasi-particles when an excitation larger than the superconducting gap splits Cooper pairs and therefore vanishes for $\hbar\omega < 2\Delta$. At low enough frequencies[2] ($\hbar\omega \ll 2\Delta$) and low temperatures ($T \ll T_c$), σ_1 will vanish and we can rewrite σ_2 as

$$\frac{\sigma_2}{\sigma_n} \simeq \frac{\pi\Delta_0}{\hbar\omega}\left[1 - \frac{1}{16}\left(\frac{\hbar\omega}{\Delta_0}\right)^2 - \frac{3}{1024}\left(\frac{\hbar\omega}{\Delta_0}\right)^4 + ...\right] \tag{2.45}$$

Since σ_1 vanishes at very low temperatures, by using a sufficiently low temperature one can make the microwave dissipation of a superconductor arbitrary low: the dissipative

[2] In the case of NbN, $\Delta \simeq 1$ meV, therefore the condition $\hbar\omega \ll 2\Delta$ is verified for microwave frequencies.

response of the electron system becomes very small compared to the reactive response ($\sigma_1 \ll \sigma_2$). In the limit that the film is thin compared to its London penetration depth ($t \ll \lambda_L$), we can use these results in equation 2.42 and a first order development (in σ_1/σ_2) leads to

$$L_k(T=0) = \frac{\sigma_2}{t\omega(\sigma_1^2+\sigma_2^2)} = \frac{\sigma_2}{t\omega\sigma_2^2(1+(\sigma_1/\sigma_2)^2)} \simeq \frac{1}{t\omega\sigma_2} = \frac{\hbar}{\pi\Delta_0 t\sigma_n} = \frac{\hbar R_N}{\pi\Delta_0} \quad (2.46)$$

where $R_N = 1/(\sigma_n t)$ represents the normal state sheet resistance of our film.

From Eq. 2.46, we see that the kinetic inductance is directly proportional to the normal state resistance of the film, and inversely proportional to its critical temperature. This implies that the kinetic inductance will scale with disorder in the film.

2.4 Electronic Transport in Disordered Superconductors

2.4.1 Weak Localization and Fluctuations Paraconductivity

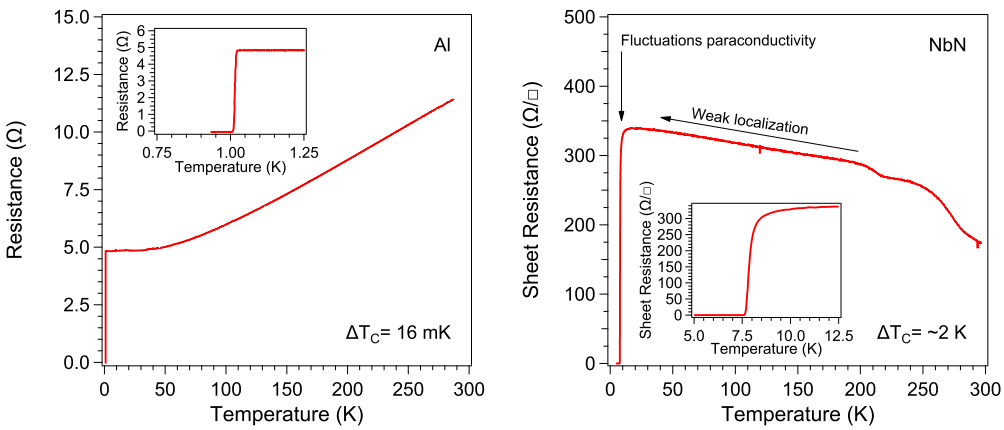

Figure 2.5: Resistance against temperature measurements for a conventional **(left)** and a strongly disordered (NbN) **(right)** superconductor. The insets correspond to a magnification of the R vs. T curve around the superconducting transition.

In a conventional superconductor, such as aluminium (Fig. 2.5 (left)), we observe a decrease of the resistance against decreasing temperature, due to out-freezing of the electron-phonon scattering processes. Finally, as the temperature reaches T_c, the resistance abruptly drops to zero. By contrast, in a strongly disordered superconductor like NbN (Fig. 2.5 (right)), the resistance increases with decreasing temperatures until a plateau is

reached. Further decreasing the temperature, the resistance gradually decreases and a broad superconducting transition is observed: in strongly disordered superconductors, there are several corrections to the conductivity at low temperatures that go beyond the classical Boltzmann transport equation [28].

The increasing resistance can be explained by the so-called *weak localization* scenario [36, 42], which finds its origin in coherent backscattering of electronic charge carriers and gives a positive contribution to the resistivity in the absence of a magnetic field. In a disordered electronic system, the electron motion is diffusive and because of random scattering events, there is a finite probability for self-crossing electron paths. If no inelastic scattering has occurred along the trajectory, quantum interference can happen at the intersection and the electron will localize in a circular motion. Localized electrons do not contribute to the conductivity anymore, therefore this leads to an increase in the net resistivity.

In principle, weak localization can happen in any system, however it is much more likely to find a self-crossing trajectory in system with low dimensionality, such as disordered superconductors. As the temperature decreases, more and more electrons are localized and the resistance gradually increases.

The broad superconducting transition in disordered superconductors can be fully described by two different mechanisms.

Above T_c, thermodynamic fluctuations give rise to short-lived Cooper pairs, which increase the conductivity: as the temperature decreases, more and more Cooper pairs come in and out of existence, gradually decreasing the overall resistance of the sample, until the condensation temperature is reached. These conductivity fluctuations have been described by Aslamasov and Larkin [38]. In the two-dimensional case relevant to our devices, the fluctuation term is given by

$$\sigma_{2D}(T) = \frac{e^2}{16\hbar t}\left(\frac{T_c}{T - T_c}\right) \tag{2.47}$$

The total conductivity above T_c is now expressed as $\sigma(T) = \sigma_n + \sigma_{2D}(T)$. This result is particularly remarkable by its simplicity and it is worth noting that it contains no adjustable parameters apart from T_c.

The second mechanism, contributing to the broad superconducting transition below T_c, is described in the following section.

2.4.2 Vortex-induced Dissipation

In a thin disordered superconductor, below T_c, the resistance doesn't immediately vanish. This can be explained by a Berezinskii–Kosterlitz–Thouless (BKT) topological phase transition [43, 44] where thermal fluctuations excite pairs of vortices. These vortex-antivortex pairs (VAP) are bound states, formed by vortices with supercurrents circulating in opposite directions [45–47]. Above the ordering temperature T_{BKT}, VAPs start to dissociate and their movement cause the observed finite resistance.

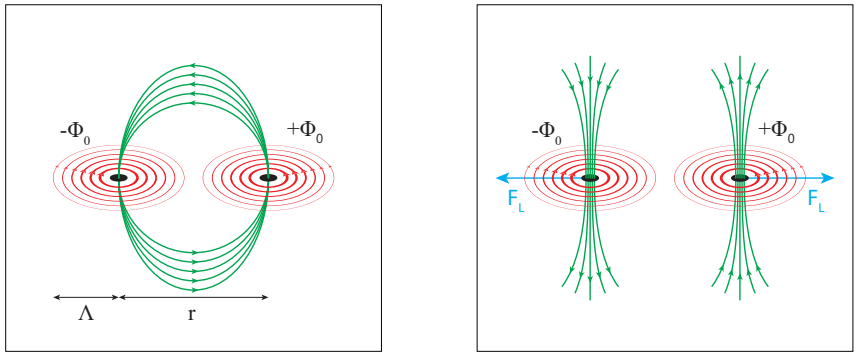

Figure 2.6: **(left)** Vortex-antivortex pair. The supercurrents (red) of the two individual vortices generate a magnetic flux quantum Φ_0 which electromagnetically binds the opposite vortex and circulate through both vortex cores (black). In a disordered superconductor, the relatively low vortex-interaction $A(T)$ allows for the thermal excitation of an ensemble of fluctuating vortex-antivortex pairs (VAPs) with statistically distributed core-to-core elongation r. **(right)** With increasing fluctuation strength k_BT, the averaged elongation increases until the VAP unbinds above T_{BKT}, the unbound vortices are now free to move due to the Lorentz force and cause dissipation. As the temperature increases further, more and more VAPs unbind and the resistive contribution gets bigger.

The necessary criterion for a BKT phase transition is a logarithmic dependence of the electromagnetic vortex interaction on the distance between the vortex centers. The potential energy of an isolated VAP is given by [48]

$$U_{\mathrm{VAP}}(r,T) = A(T)\ln\left(\frac{r}{\xi_{GL}}\right) + 2\mu_c(T) \tag{2.48}$$

where $\mu_c(T)$ is the vortex core energy and $A(T)$ is the vortex interaction constant. The vortex interaction constant is given by

$$A(T) = \frac{\Phi_0^2}{\pi\mu_0\Lambda(T)} \tag{2.49}$$

Using Eq. 2.29 and 2.30, we can calculate the effective penetration depth for a superconductor in the dirty limit

$$\Lambda(T) = \frac{2\Phi_0^2}{\pi^3\mu_0}\frac{R_N e^2}{\hbar}\left[\Delta(T)\tanh\left(\frac{\Delta(T)}{2k_BT}\right)\right]^{-1} \tag{2.50}$$

Using this, the vortex interaction constant becomes

$$A(T) = \frac{\pi^2}{2}\frac{\hbar}{R_N e^2}\Delta(T)\tanh\left(\frac{\Delta(T)}{2k_BT}\right) \tag{2.51}$$

In Eqs. 2.48 and 2.51, we immediately see that a high normal state resistance leads to a small vortex interaction constant, and in turn translates into a small VAP binding potential. The smaller the binding potential, the easier it becomes for thermal fluctuations to unbind VAPs and therefore the smaller the ordering temperature becomes. Unbound vortices move due to the Lorentz force and cause a finite resistance given by

$$\rho(T) = a \exp\left(-2\sqrt{b\frac{T_c - T}{T - T_{BKT}}}\right) \quad \text{with } T_{BKT} < T < T_c \tag{2.52}$$

where a, b are material dependent parameters.

Chapter 3

Superconducting Microwave Resonators

A resonator is by definition a device or system that exhibits resonance or resonant behavior, that is, it naturally oscillates at some frequencies, called its resonant frequencies. In particular, superconducting microwave resonators are of interest due to their extremely low losses and have found many applications in circuit QED [49].

This chapter first describes the basic concepts of microwave transmission lines and resonators and continues with a description of the different loss mechanism that limit performances of resonators.

In this work, we study the self-resonant modes of high-impedance superconducting nanowires and characterize their losses. The concepts and models introduced in this chapter will provide the necessary framework to understand the origin of these losses.

3.1 Two-port Network

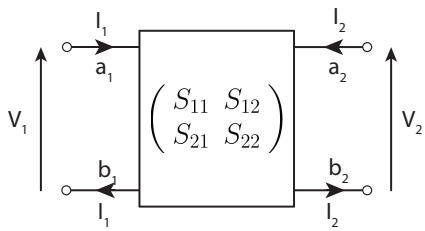

Figure 3.1: Schematic of a two-port network characterized by its scattering matrix. The properties of the two-port network can either be expressed as a function of voltage and currents at each port (V_1, I_1, V_2, I_2) or as a function of incident and reflected waves (a_1, b_1, a_2, b_2).

A two-port network (Fig. 3.1) is an electric circuit with two pairs of terminals. By definition, two terminals constitute a *port* if and only if the electric current entering one terminal equals the current emerging from the other terminal. Mathematically, a two-port network is fully described by a 2×2 matrix of complex numbers that establish relations between the voltage and current across the ports [50].

A convenient way of expressing the properties of a two-port network is the *ABCD matrix*,

given by

$$\begin{pmatrix} V_1 \\ I_1 \end{pmatrix} = \begin{pmatrix} A & B \\ C & D \end{pmatrix} \begin{pmatrix} V_2 \\ -I_2 \end{pmatrix} \tag{3.1}$$

For a combination of several two-port networks, the total ABCD matrix is simply the product of the ABCD matrix of each two-port network. Morever, the ABCD matrix description is particularly convenient as series and shunts impedances are simply given by

$$ABCD_{series} = \begin{pmatrix} 1 & Z_{series} \\ 0 & 1 \end{pmatrix} \quad \text{for a series impedance } Z_{series}$$

$$ABCD_{shunt} = \begin{pmatrix} 1 & 0 \\ Z_{shunt}^{-1} & 1 \end{pmatrix} \quad \text{for a shunt impedance } Z_{shunt}$$

A two-port network is said to be *reciprocal* if the voltage appearing at port 2 due to a current applied at port 1 is the same as the voltage appearing at port 1 when the same current is applied to port 2. In the ABCD matrix description, this translates into $\det[ABCD] = AD - BC = 1$.

Finally, a two-port network is said to be *symmetrical* if its input and output impedances are equal, which translates into $A = D$ in the ABCD matrix.

3.1.1 Scattering Parameters

At high frequencies (microwave frequencies), it is generally difficult to accurately measure voltages and currents directly and the use of power and energy variables is more appropriate. The scattering matrix describes the relationship between the incident (a_1, a_2) and reflected (b_1, b_2) waves and is given by

$$\begin{pmatrix} b_1 \\ b_2 \end{pmatrix} = \begin{pmatrix} S_{11} & S_{12} \\ S_{21} & S_{22} \end{pmatrix} \begin{pmatrix} a_1 \\ a_2 \end{pmatrix} \tag{3.2}$$

Each scattering parameter (S parameter) consists of a unitless complex number that represents the magnitude and phase response of the device at a given frequency. S_{11} (S_{22}) are known as the reflection coefficients from port 1 (port 2), S_{21} (S_{12}) correspond to the transmission from port 1 to port 2 (port 2 to port 1). For a reciprocal two-port network, we have $S_{12} = S_{21}$ and for a symmetrical network $S_{11} = S_{22}$.

The scattering parameters are of particular importance for real devices as they are directly accessible to the experimentalist through measurement equipment such as a vector network analyzer (VNA).

Additionally, the S-parameters can be expressed in term of the ABCD matrix elements. For a reciprocal and symmetrical network, and assuming the ports are loaded with loads of characteristic impedance Z_0, the scattering matrix is given by [51]

$$S_{11} = \frac{A + B/Z_0 - CZ_0 - D}{A + B/Z_0 + CZ_0 + D} \tag{3.3}$$

$$S_{21} = \frac{2}{A + B/Z_0 + CZ_0 + D} \tag{3.4}$$

3.2 Transmission Lines

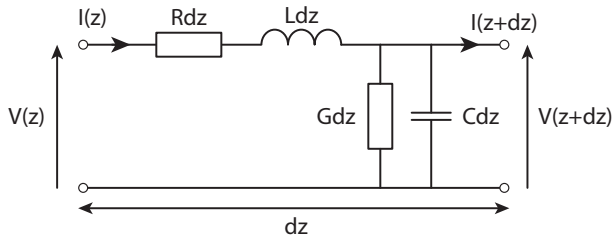

Figure 3.2: Lumped element representation of a segment of length dz of a transmission line with the resistance R, inductance L, capacitance C and shunt conductance G per unit length.

A transmission line is a specialized structure designed to conduct alternating currents with a frequency high enough that their wave nature must be taken into account. The properties of a transmission line can be studied by the telegraph equations [50] where the transmission line is represented by a succession of infinitesimally short segments of length dz as depicted in figure 3.2. The voltage and current can be written as

$$\begin{cases} V(z) = V^+ e^{-\gamma z} + V^- e^{\gamma z} \\ I(z) = I^+ e^{-\gamma z} + I^- e^{\gamma z} \end{cases} \tag{3.5}$$

where $\gamma = \alpha + i\beta = \sqrt{(R + i\omega L)(G + i\omega C)}$ is the complex propagation constant for a travelling wave at the frequency ω. From these, the characteristic impedance of the transmission line follows

$$Z_0 = \frac{V^+}{I^+} = -\frac{V^-}{I^-} = \sqrt{\frac{R + i\omega L}{G + i\omega C}} \tag{3.6}$$

For a superconducting transmission line, we can neglect R and G due to the absence of

resistive losses, and therefore rewrite the previous expressions as

$$\gamma = i\beta = i\omega\sqrt{LC} \tag{3.7}$$

$$Z_0 = \sqrt{\frac{L}{C}} \tag{3.8}$$

The transmission lines used in this work are *coplanar waveguides* (CPW). CPWs were originally introduced by Wen [52] and consist of a conducting track of width w together with a pair of return conductors on a substrate (see Fig. 3.2). All three conductors are on the same side of the substrate, and hence are *coplanar*. The return conductors are separated from the central track by a small gap g. The capacitance and inductance per length and the characteristic impedance of a CPWs is directly dependent on w and g, and is calculated with a technique known as *conformal mapping*. The detailed calculations can be found in appendix B. As standard microwave equipment have a characteristic impedance of $50\,\Omega$, the CPWs in this work are designed to the same $50\,\Omega$ characteristic impedance in order to avoid unwanted reflections.

3.3 Half-wavelength Resonators

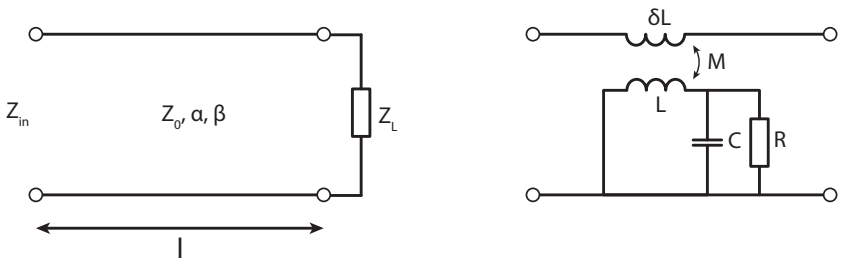

Figure 3.3: **(left)** Portion of transmission line of length l loaded with an impedance Z_L **(right)** Half-wavelength resonator inductively coupled to a transmission line. Energy is exchanged through the mutual inductance between the probing line and the resonator.

Let's consider a length l of transmission line of characteristic impedance Z_0 and loaded by an impedance Z_L (Fig. 3.3 (left)). The input impedance is given by [50]

$$Z_{in} = Z_0 \frac{Z_L + Z_0 \tanh\left[(\alpha + i\beta)l\right]}{Z_0 + Z_L \tanh\left[(\alpha + i\beta)l\right]} \tag{3.9}$$

For an open-ended transmission line, $Z_L \to \infty$ and Eq. 3.9 becomes

$$Z_{in} = Z_0 \coth\left[(\alpha + i\beta)l\right] = Z_0 \frac{1 + i\tan\beta l \tanh\alpha l}{\tanh\alpha l + i\tan\beta l} \tag{3.10}$$

This forms a half-wavelength resonator with a fundamental mode resonance frequency ω_0 verifying $l = \lambda/2 = \pi v_{ph}/\omega_0$, where v_{ph} is the phase velocity in the transmission line. If we introduce $\Delta\omega = \omega - \omega_0$, a small detuning from the resonance frequency, we can write

$$\beta l = \frac{\omega l}{v_{ph}} = \frac{\omega_0 l}{v_{ph}} + \frac{\Delta\omega l}{v_{ph}} = \pi + \frac{\pi\Delta\omega}{\omega_0} \tag{3.11}$$

For small detunings ($\Delta\omega \ll \omega_0$) and for a superconducting transmission line, for which we can assume $\alpha l \ll 1$, we have:

$$\tanh \alpha l \simeq \alpha l \quad \text{and} \quad \tan \beta l \simeq \frac{\pi\Delta\omega}{\omega_0} \tag{3.12}$$

Using this and introducing the internal quality factor Q_i of the resonator with $Q_i = \beta/2\alpha = \pi/2\alpha l$, Eq. 3.10 becomes

$$Z_{in} = Z_0 \frac{1 + i\frac{\Delta\omega}{\omega_0}\pi\alpha l}{\alpha l + i\frac{\Delta\omega}{\omega_0}\pi} \simeq Z_0 \frac{1}{\frac{\pi}{2Q_i} + i\pi\frac{\Delta\omega}{\omega_0}} = \frac{2Z_0 Q_i/\pi}{1 + 2iQ_i\frac{\Delta\omega}{\omega_0}} \tag{3.13}$$

Eq. 3.13 represents the impedance response of a superconducting half-wavelength resonator for frequencies close to its resonance frequency ω_0. The internal quality factor represents the ratio of the energy stored in the resonator divided by the energy dissipated in the resonator in a single cycle. The study of Q_i gives valuable insight on the nature of dissipation in a device.

Additionally, near the resonance frequency, the resonator can be modeled by a lumped element parallel RLC circuit with the following circuit parameters [50]:

$$R = \frac{Z_0}{\alpha l} = \frac{2Q_i Z_0}{\pi}, \quad C = \frac{\pi}{2\omega_0 Z_0} \quad \text{and } L = \frac{1}{\omega_0 C} \tag{3.14}$$

3.3.1 Inductive Coupling

In order to interact with the resonator, the resonator needs to be coupled to the outside world. In this work, the resonators are inductively coupled to a probing transmission line of characteristic impedance Z_0 (see Fig. 3.3 (right)). In an inductive coupling scheme, energy is exchanged between the resonator and the transmission line through a mutual inductance M. A half-wavelength resonator of impedance Z_r inductively coupled to a portion of transmission line of inductance δL will have an input impedance [53, 54]:

$$Z_{in} = i\omega\delta L + \frac{\omega^2 M^2}{Z_r} \tag{3.15}$$

Loading the resonator has for effect to change its resonant frequency. Indeed, from Eqs. 3.13 and 3.15, we immediately see that the resonance condition $\mathrm{Im}(Z_{in}) = 0$ will be verified for different frequencies. However, assuming that the coupling is weak, the frequency shift due to the coupling can be neglected and, at resonance, we have

$$Z_{in} \simeq \frac{\omega_0^2 M^2}{Z_r} \tag{3.16}$$

Using Eq. 3.13, we get

$$Z_{in} = \frac{\pi \omega_0^2 M^2}{2 Z_0 Q_i} \left(1 + 2iQ_i \frac{\Delta\omega}{\omega_0}\right) \tag{3.17}$$

The coupling quality factor Q_c is defined by the ratio of the energy stored in the resonator and the power exchanged between the resonator and the transmission line each cycle. The coupling quality factor Q_c for an inductively coupled resonator is given by [54]

$$Q_c = \frac{\pi \omega_0^2 M^2}{4 Z_0^2} \tag{3.18}$$

Additionally, we define the loaded quality factor Q_l as the total quality factor of the resonator and coupling. The loaded quality factor is given by

$$\frac{1}{Q_l} = \frac{1}{Q_i} + \frac{1}{Q_c} \tag{3.19}$$

Finally, using Eqs. 3.17, 3.18 and 3.19, we can derive the expression for the S_{21} parameter of the resonator coupled to the transmission line, which corresponds to the quantity measured in experiments. S_{21} is given by

$$S_{21} = \frac{1}{1 + Z_0/2Z_{in}} = \frac{1}{1 + Q_i/Q_c(1 + 2iQ_i\Delta\omega/\omega_0)^{-1}} = 1 - \frac{Q_l Q_c^{-1}}{1 + 2iQ_l\Delta\omega/\omega_0} \tag{3.20}$$

3.3.2 Number of Photons

In quantum physics, the electromagnetic field inside the resonator can be quantized and is therefore usually expressed as an average number of photons $\langle n \rangle$ instead of the more traditional (and classical) microwave power.

When probed with an applied power P_{in} at $\omega = \omega_0$, the average energy stored in a resonator of characteristic impedance Z_r is given by [55]

$$\langle E_{int} \rangle = \frac{2}{\pi} \frac{Z_0}{Z_r} \frac{Q_l^2}{Q_c} \frac{P_{in}}{\omega_0} \tag{3.21}$$

This energy corresponds to an average number of microwave photons $\langle n \rangle$ given by

$$\langle n \rangle = \frac{\langle E_{int} \rangle}{\hbar \omega_0} \tag{3.22}$$

3.3.3 Generalized Resonator

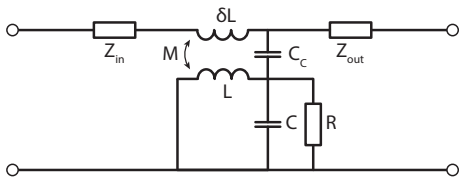

Figure 3.4: Generalized resonator model. The resonator is coupled to the transmission line through both capacitive and inductive coupling. Additionally, the transmission line is not perfectly matched.

The circuit described in the previous section consists of an *ideal* resonator. Unfortunately, non-idealities in the experimental setup, such as impedance mismatch in the probing line, can lead to significant asymmetry in the resonance line shape. Moreover, in practice, the resonator coupling is always a combination of both capacitive and inductive coupling, which significantly complicates calculations.

A generalized model (see Fig. 3.4) that accounts for these imperfections has been proposed by Khalil [56]. In this model, the coupling quality factor Q_c is replaced by a complex quality factor $|Q_c| \exp(-i\varphi)$ that accounts for both inductive and capacitive coupling, and for any impedance mismatch of the probing line. Additional terms are also introduced to compensate for the effects of the environment, such as an imperfect background and propagation delays caused by the length of the cables. Eq. 3.20 becomes

$$S_{21} = a e^{i\alpha} e^{-\omega i \tau} \left[1 - \frac{Q_l |Q_c|^{-1} e^{i\varphi}}{1 + 2iQ_l \Delta\omega/\omega_0} \right] \tag{3.23}$$

where a, α and τ are respectively an amplitude, a phase shift and the electrical delay, and all account for the influence of the environment: a and α account for a non-ideal background signal, while τ accounts for the propagation delay in the cables. Fig. 3.5 shows simulated examples of two resonators with similar parameters ($Q_l = 10000$, $Q_c = 20000$, $\omega_0 = 4\,\mathrm{GHz}$). In Fig. 3.5, the resonator responses are plotted in two different ways. The top panels show the magnitude and phase response of the resonator as a function of the probing frequency. The bottom panels are plots of the imaginary part of the S_{21} parameter as a function of its real part. The resonator on the left is an ideal resonator in an ideal environment. The magnitude and phase responses are perfectly symmetrical and the real and imaginary components form a perfect circle. The resonator on the right,

on the other hand, was placed in an environment with significant impedance mismatch, attenuation and a large electrical delay and its response is significantly distorted.

In this work, we fit our experimental data to Eq. 3.23 using a traceable fit routine originally introduced by Probst [57]. This method rely on fitting the real and imaginary components of the S_{21} transmission response of the resonator to a circle and accounts for all imperfections.

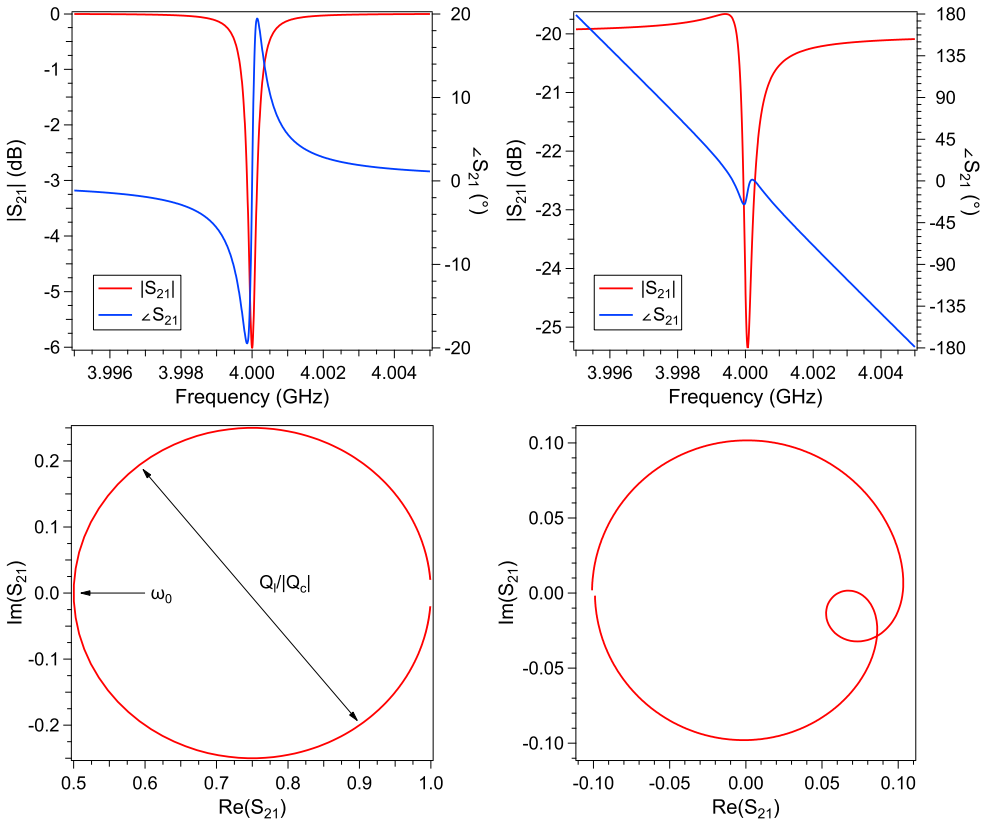

Figure 3.5: **(left)** Magnitude and phase response of an ideal resonator along with its resonance circle. The diameter of the resonance circle corresponds to the ratio of the quality factors and the resonance frequency corresponds to $\mathrm{Im}\, S_{21} = 0$. **(right)** Skewed resonator response due to several imperfections. The resonance line shape is asymmetric due to impedance mismatch in the probing line and the resonance circle is distorted due to significant electrical delay.

3.4 Loss Mechanisms in Superconducting Resonators

In the previous section, we introduced the concept of quality factor for a microwave resonator. More specifically, we showed in Eq. 3.14 that a resonator internal quality factor is related to a shunt resistor in the parallel RLC equivalent circuit of the resonator. Here, it is crucial to point out that while this resistance is infinite at DC and no dissipation takes place, at microwave frequencies, this resistance is finite and dissipation occurs. This finite resistance can be split between two general mechanisms: quasiparticles and dielectric loss.

3.4.1 Resistive Loss: Quasiparticles

At microwave frequencies, current is forced to flow within the skin depth of a conductor (see section 2.3.5). For our thin-films, the skin depth is typically greater than the film thickness. This constraint means that unlike at DC, where conduction can occur by the path of least resistance, at microwave frequencies some current is carried by quasiparticles. The current carried by quasiparticles can then exhibit resistance and therefore limit the quality factor.

The easiest example of this is to examine the temperature dependence of a microwave resonator below T_c. Unlike at DC, where dissipation-less conduction is found for all temperatures below T_c, a microwave resonator will demonstrate a strongly temperature dependent quality factor, which is due to the thermally varying population of quasiparticles.

Temperature is not the only cause of quasiparticles: they can also arise from pair-breaking photons, which are photons with an energy greater than the superconducting gap. These are the motivation behind the kinetic inductance detector [58], where the pair-breaking photons lead to a cloud of quasiparticles. These quasiparticles produce both a change in the kinetic inductance (see section 2.3.4 and 2.3.5) and the dissipation of the resonator. In non-detector applications, the pair-breaking photons are an unwanted effect and cryostats are equipped to attenuate these pair-breaking photons. This attenuation is performed by a combination of lossy in-line filters [59] and absorptive coatings [60] on components below the mixing chamber (see section 5 for additional details on the experimental setup used in this work). Despite these efforts, larger than expected residual quasiparticle populations are often found in a variety of quantum circuits [61–65]. While these may arise from non-ideal superconductor behaviour, poor filtering or poor thermalization, it has also been shown that external sources such as ionizing radiation from the atmosphere can lead to significant pair-breaking effects [66].

Disorder Induced Loss

A variety of disordered superconducting thin-films are experimentally found to exhibit significant internal dissipation [11, 12, 67]. Additionally, Coumou [68] observed that the internal quality factor of disordered titanium nitride resonators is reduced as the

thickness of the film decreases. This decrease in thickness corresponds to a reduction of the Ioffe-Regel parameter, ie. an increase in disorder.

These results hint toward the existence of a disorder induced residual quasiparticle density that intrinsically limits the microwave performance of devices made with highly disordered superconductors. The microscopic origin of this loss mechanism is still debated, however recent theoretical work hints at the presence of low-lying sub gap states in the proximity of the SIT [69].

3.4.2 Resistive Loss: Two-level Systems (TLS)

The lumped element model of a capacitor includes a lossless ideal capacitor in series with a resistor called the equivalent series resistance (ESR). The ESR is a measure of the non-ideality of the capacitor and accounts for dielectric losses in the capacitor. The impedance of a non-ideal capacitor is therefore rewritten as $Z_c = R_{ESR} + 1/iC\omega$. The presence of the non-imaginary term means that the impedance points at some angle δ from the imaginary axis. By examining the absolute value of $\tan\delta$, we arrive at $\tan\delta = \omega R_{ESR} C$, which is a quality factor. This expression is known as the *loss tangent* and is used to describe the dissipation within a capacitor. The loss tangent is generally frequency dependent due to the dipole relaxation within dielectrics. Additionally the dipole relaxation itself is usually temperature dependent.

Within superconducting resonators, the loss tangent of the effective capacitance per unit length can limit the quality factor. This effect was first quantified by O'Connell [70] where in the low temperature, low microwave power limit, dipoles within the dielectric become desaturated and can absorb microwave photons as a general two level system (TLS). Here, the resonator is directly probing the density of dipoles which are within a narrow energy spectrum that is centered on the resonator frequency. When the microwave power is increased, these dipoles become saturated, leading to a reduction in the amount of power absorbed by the dipoles. Equivalently, Macha [71] demonstrated that within the temperature range of $20 - 900\,\mathrm{mK}$, the dipoles can become thermally saturated, which also leads to a reduction of the amount of power absorbed by the dipoles. A Kramers-Kronig relation can translate between the real and imaginary parts of the dipole absorption properties. Correspondingly, Gao [15] and Lindström [72] showed that the thermal desaturation of the dipoles leads to a temperature-dependent permittivity. Importantly, this leads to a frequency shift that provides an independent measure of dielectric loss that can be insensitive to other loss mechanisms.

A recent development in understanding dielectric loss is that the dipole energies are not stationary. Qualitatively slow drifts in energy of an individual dipole two-level system was reported by Grabovskij [73]. In further work, Lisenfeld [74] found that these two-level systems interact with one another. This interaction was motivated as the cause of the slow drifts in the TLS energy. In related work, Burnett [75] found that the frequency of superconducting resonators was not stable, with the instability scaling stronger than $1/T$. This frequency instability was attributed to the interaction between TLS, which produces a time dependence of the permittivity. The time-variation of the TLS energy

has an important consequence on the dielectric loss: if the TLS energy shifts to become non-resonant, then it cannot absorb microwave photons from the resonator. In this case, Faoro [76] showed that the microwave-power dependence of the dielectric loss becomes logarithmic. In such a situation, since the logarithmic power dependence of loss is so weak, the temperature dependence of the permittivity is the more reliable measure of dielectric loss.

Logarithmic TLS Model

The logarithmic power dependence of the dielectric loss introduced in the previous paragraph is formally given by [76]

$$\frac{1}{Q_i} = F \tan\delta^i_{TLS} P_\gamma \ln\left(\frac{cn_c}{\langle n\rangle} + \delta'_0\right) \tanh\left(\frac{hf_r}{2k_BT}\right) \tag{3.24}$$

Here, F is the *filling factor* (also known as *participation ratio*), which is the ratio of electric field threading the TLS host volume to the total electric field and $\tan\delta^i_{TLS}$ is the intrinsic TLS loss tangent (found from an independent measurement of the permittivity), sensitive to the complete TLS spectrum. Additionally, P_γ is the TLS switching rate ratio, defined by $P_\gamma = 1/\ln(\gamma_{max}/\gamma_{min})$ where γ_{max} and γ_{min} are the maximum and minimum rate of TLS switching respectively. c is a large constant, n_c is the number of photons generating the electric field saturating a TLS and δ'_0 is the log-scaled next dominant loss rate. The temperature dependent hyperbolic tangent scaling highlights the thermal saturation of TLS. A typical curve obtained by this model is shown in Fig. 3.6(left).

Intrinsic Loss Tangent - Temperature Dependent Permittivity

The intrinsic loss tangent, sensitive to any thermally varying TLS, can be measured by studying the frequency of a microwave resonator as a function of temperature: as the temperature decreases, TLS desaturate and start exchanging energy with the resonator, leading to a decrease of the resonance frequency. Once all TLS are thermally desaturated, an upturn in frequency is observed as TLS resonantly exchange energy with the resonator. This frequency shift is described by [15]

$$\Delta f = F\delta^i_{TLS}\left(\ln\left(\frac{T}{T_0}\right) - [g(T,f) - g(T_0,f)]\right) \tag{3.25}$$

where $\Delta f = (f_r(T) - f_r(T_0))/f_r(T_0)$, $g(T,f) = \mathrm{Re}\left(\Psi\left(\frac{1}{2} + hf/2\pi i k_B T\right)\right)$, T_0 is a reference temperature and Ψ is the complex digamma function. We see from Eq. 3.25 the frequency shift is directly proportional to $F\tan\delta^i_{TLS}$. For a given $\tan\delta^i_{TLS}$, this means that an increased filling factor F will correspond to an increase in loss.

When the physical dimensions of a resonator are reduced, the concentration of electrical field increases and leads to an increase in the filling factor [15]. Because of this, small

dimension resonators have an unfavorable scaling of the filling factor and will lead to additional dissipation due to TLS as highlighted in Fig. 3.6(right).

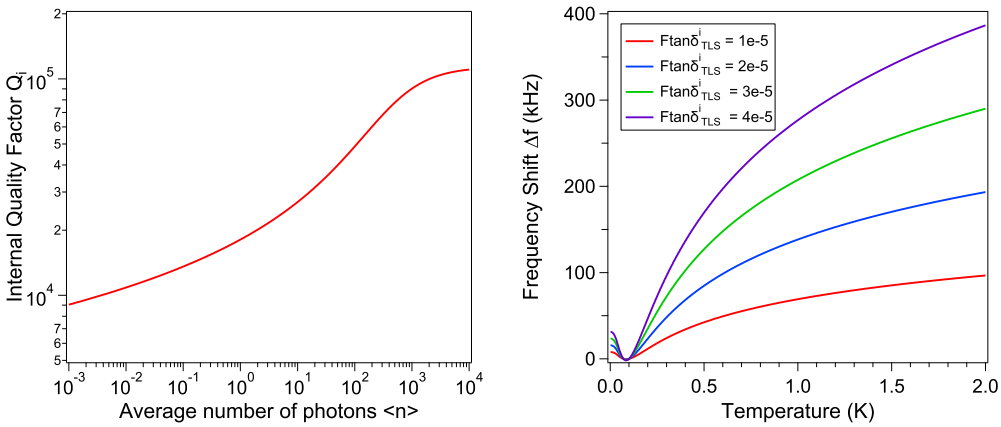

Figure 3.6: **(left)** Eq.3.24 log dependence of TLS related loss calculated at 10 mK and $F \tan \delta^i_{TLS} = 8 \times 10^{-6}$. At high microwave excitation, the TLS are saturated and the loss in the resonator are governed by the next dominant loss rate (δ'_0 in Eq.3.24). As the number of photons in the resonator decreases, TLS start to desaturate and exchange energy with the resonator, leading to the logarithmic loss described by Eq. 3.24. **(right)** Frequency shift as a function of temperature for different values of $F \tan \delta^i_{TLS}$. Larger filling factors correspond to larger losses and hence larger frequency shifts.

3.4.3 Radiation Loss

An additional loss mechanism that may hinder performances of superconducting resonators is known as *radiation loss*. A general definition of radiation loss is the energy that is lost by radiating away from the circuit and into the surrounding environment. In other words, radiation loss is the energy radiating into free space rather than being confined in the resonant structure.

Radiation losses are highly dependent on the geometry and are non-trivial to precisely calculate, however, for CPW and microstrip structures, they are usually very small and can be neglected. We estimate the radiation loss in our device to be $\alpha_r = 1/Q_{rad} < 1 \times 10^{-6}$ [58, 77].

3.4.4 Generalized Loss Model

We showed in the previous section that several different mechanism can contribute to the loss of energy in the resonator. We can define a generalized loss model where all the different contributions are accounted for. This generalized expression for the internal

quality factor is given by

$$\frac{1}{Q_i} = \frac{1}{Q_{TLS}(T,P)} + \frac{1}{Q_{qp}(T)} + \frac{1}{Q_{disorder}(t)} + \frac{1}{Q_{rad}(w)} + \dots \tag{3.26}$$

From this last equation, we see that the internal quality factor of a resonator will be limited by the largest loss mechanism in the device. To distinguish between the loss mechanisms, we can examine the response of our devices against various parameters, such as temperature, excitation power, device geometry or film thickness. Because each loss mechanism is entirely dependent on a specific set of parameters, by comparing the data with the models described in this section, the dominant loss mechanism can be determined.

Chapter 4

Nanofabrication Techniques

This chapter presents an in-depth description of the various micro- and nanofabrication techniques used in this work. Our devices were fabricated using a conventional top-down approach relying on the patterning of thin films via planar lithography and dry etching.

4.1 Fabrication Challenges

As described previously, the devices used in this work are long and narrow nanowires made of a highly disordered superconductor. Due to their dimensions, nanowires are inherently difficult devices to fabricate. Fabricating uniform high-aspect-ratio nanowires, with a length of the order of a millimeter, but a thickness and width of a few nanometers, poses a specific set of constraints on the techniques available. Additionally, because of their microscopic nature, disordered superconductors are not well-behaved materials and present many challenges from a fabrication point of view. Most importantly, disordered superconductors are compound materials and their properties are extremely dependent on the growth conditions, which limits the available deposition techniques and requires very careful process optimization.

Combining the constraints of nanowire fabrication with the requirements of disordered superconductors leads to a unique challenge for the researcher and requires an in-depth understanding of nanofabrication in order to find the appropriate process flow at the intersection of both parameter spaces.

Traditionally, nanowires are fabricated by a *lift-off* process (see section 4.2) where a trench at the dimensions of the nanowire is opened in a resist mask before the desired material is deposited (i.e. the resist mask is the negative of final pattern). This approach ensures mechanical stability of the resist mask by only having large areas of resist on the sample. Unfortunately, none of the deposition techniques suitable for disordered superconductors are compatible with such process (see section 4.3).

The alternative approach is therefore to use an *etching* process, where a highly optimized disordered thin film is first deposited on the substrate and then patterned into nanowires using a novel method (see section 4.4). This approach, however, requires the resist mask to be the positive image of the final pattern (i.e. a free-standing, high-aspect-ratio nanowire-shaped resist mask), which is significantly more challenging to fabricate.

After careful process development, by using a combination of ultra-high resolution negative-tone lithography and a tailored etching process (see section 4.5), we can reliably and reproducibly fabricate high quality disordered superconducting nanowires (see section 4.6).

4.2 Lithography Techniques

Any top-down micro- or nanofabrication relies on transferring geometric patterns into the bulk substrate or thin-layers of various materials in a process called *lithography*. For that purpose, a thin-layer of a photon- or electron-sensitive *resist* is spin-coated on the substrate and the casting solvent is evaporated by heating the resist layer in a so-called *baking* step. A pattern is then exposed in the resist with one of the lithography techniques described in this section, and subsequently developed by a dedicated chemical (the *developer*). After a certain amount of energy per unit area is reached (the *exposure dose*), parts of the resist become soluble in the developer and after the development, the resist is only covering parts of the substrate, enabling the transfer of the pattern into the underlying material.

4.2.1 Additive and Subtractive Patterning

Lithography processes can be divided into two different families: subtractive patterning (*etching*) and additive patterning (*lift-off*). In an etching process, a previously deposited layer is spin-coated with resist. After exposure and development, the material in the areas not covered anymore by the resist is etched away (see section 4.4 and Fig. 4.1 (right)). In a final step, the remaining resist is removed. The resulting pattern is therefore the direct image of the areas opened in the resist mask.

In a lift-off process (see Fig. 4.1 (left)), on the other hand, the resist is first spin-coated, exposed and developed. Afterwards, a thin-layer of material is deposited atop. The sample is then immersed in a bath of remover that washes away the resist and the material on top: the thin-layer remains only in the areas where the resist mask was opened, forming this time the negative image of the exposed pattern. It is worth noting that lift-off generally involves two different resists: a so-called *lift-off resist* coated directly on the substrate and a regular resist on top. As shown in figure 4.2, the role of the lift-off resist is to form an undercut under the top resist once developed. Once a new layer is deposited, the presence of the undercut allows remover to enter and dissolve the resist. While an undercut also naturally occurs in most resists, the layer is usually too thin for the undercut to be relevant.

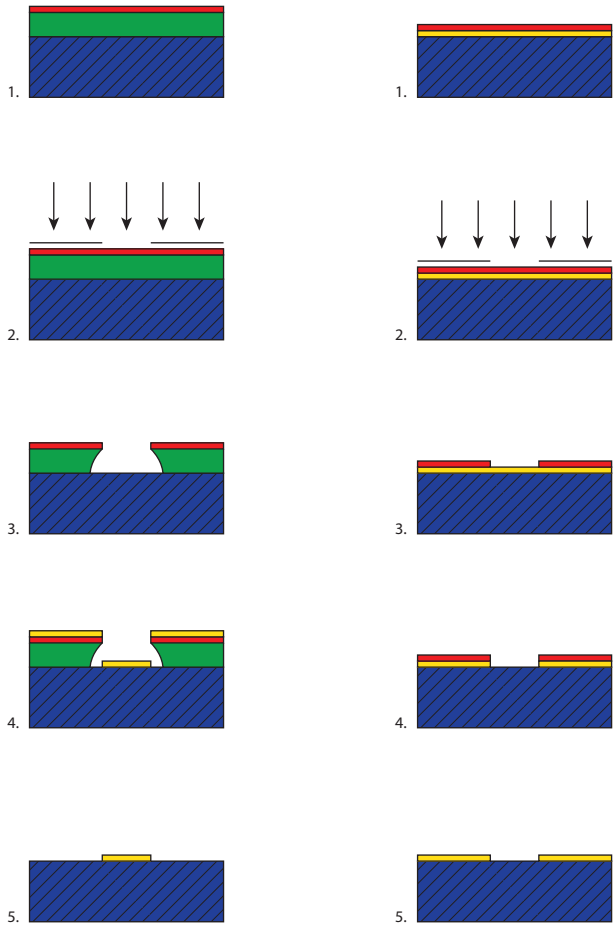

Figure 4.1: **(left)** Lift-off process: Lift-off resist (green) and a positive photoresist (red) are spin-coated on a substrate (blue) (1). The resist is then exposed through a mask (2) and developed (3). A metal layer (yellow) is then deposited on top (4). After the substrate is placed in remover, metal remains only where the resist was originally exposed (5). **(right)** Etching process: A positive photoresist is spin-coated on a substrate covered with a thin film (1), the resist is then exposed through a mask (2). After development, only the unexposed resist remains (3). The uncovered metal is then removed in an etching process (4). Finally, the remaining resist is removed and metal remains in the unexposed area (5).

4.2.2 Resists

Resists come in two different flavours: *positive* and *negative*. In the positive case, the solubility in the developer of the exposed resist is greatly increased. In the negative case, the resist is cross-linked in the exposed regions, greatly reducing its solubility.

An important metric of a resist is its *contrast* and is measured by exposing large structures

Figure 4.2: **(left)** With the presence of the undercut, the metal layer (yellow) is not continuous and allows the remover to access the resist. **(right)** Without the undercut and lift-off layer, the metal forms a continuous layer on top and remover can't access the resist.

with varying doses. After development for a fixed time (and at a fixed temperature), the remaining resist thickness is measured. The normalized resist thickness against the exposure dose (see Fig. 4.3) is called the contrast curve. The contrast γ of the resist is defined as the slope of the contrast curve by

$$\gamma = \left[\log\left(\frac{D_1}{D_0}\right)\right]^{-1} \tag{4.1}$$

where D_0 is the threshold dose at which the exposure first begins to have an effect. For a positive resist, D_1 is the clearing dose: the minimum exposure dose required to completely remove the resist. In the case of a negative resist, D_1 represents the dose at which the resist has a useful working thickness. It is important to note that γ is not a constant for a particular resist, but rather depends on the process parameters, such as the development chemistry, bake times and temperatures before and after (if applicable) exposure, etc...

Contrast curves find their origin over one hundred years ago when Hurter and Driffield (H-D) measured the optical density of photographic negatives as a function of log-exposure [78]. Micro- and nanolithography processes evolved from photographic science and borrowed many of its concepts, including H-D contrast curves. Fig. 4.3 shows typical H-D contrast curves for both positive and negative resists. These curves are calculated with the simple - yet accurate - theoretical model proposed by Ziger and Mack [79, 80]. For positive resists, the colored region illustrates a phenomenon known as *dark erosion* where the dose is too small to properly define features in the resist but enough for it to start being dissolved by the developer. For a negative resist, the colored zone corresponds to the *bright erosion* region, where the resist is entirely cross-linked by the exposure, yet still dissolved by the developer. Because dark erosion (bright erosion) translates into a loss of thickness of the resist (and reduced contrast), it is generally an unwanted effect. It can however be mitigated by carefully optimizing the resist baking procedure and developer composition.

Understanding the contrast curve, contrast and exposure doses of a resist for given process parameters is of paramount importance to ensure a high quality reproducible lithography.

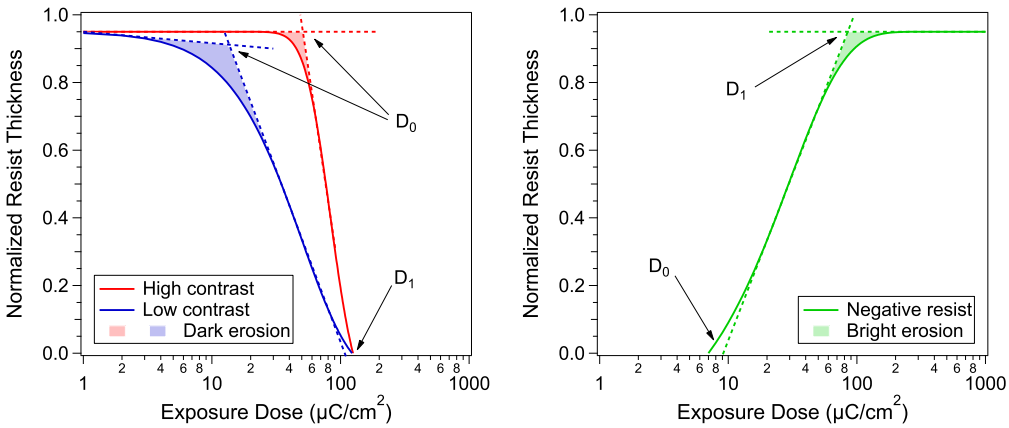

Figure 4.3: **(left)** Contrast curves for a typical high contrast (red) and low contrast (blue) positive resist. **(right)** Contrast curve for a negative resist. In both pictures, the contrast defined by Eq. 4.1 is given by the slope of the contrast curve between D_0 and D_1.

Organic resins

The most common positive photoresists are based on a mixture of DNQ (Diazonaphthoquinone) and Novolac resin (Phenol formaldehyde resin). The DNQ inhibits the dissolution of the Novolac resin, however, upon exposure to ultra-violet (UV) light, the DNQ undergoes a Wolff rearrangement and forms a ketene [81]. The ketene, in turn, reacts with ambient water to form an indene carboxylic acid, soluble in aqueous base. In these regions, the dissolution of the Novolac is no longer prevented and is therefore also washed away by an aqueous base. Novolac resins can also be used as negative-tone resists, where the exposure directly cross-links the resin, sometimes with the aid of a cross-linking agent to enhance the sensitivity of the resist.

Novolac-based resists are developed by dissolution in a basic solution. Most commonly, metal ion free TMAH (tetramethylammonium hydroxide) aqueous solutions or metal ion bearing KOH and NaOH concentrate aqueous alkaline solutions are used.

Alternatively, organic resins are used in conjunction with a so-called photoacid generator. When exposed to short wavelength particles, the photoacid generator decomposes into an acid. When the resist is subjected to a post-exposure bake, the acid diffuses in the resist and reacts with blocking groups in the polymer resin, causing it to become soluble in a basic solution. Because of this intermediate reaction step compared to DNQ-Novolac resists, these resists are called *chemically amplified resists* (CAR). CAR resists are commonly used for positive deep-UV (DUV) and low resolution electron beam lithography.

For high-resolution lithography, PMMA (poly(methyl methacrylate)) is by far the most popular positive-tone electron beam lithography resist. Exposure of PMMA causes scission of the polymer chains, increasing their solubility in the developer - typically a mixture of

MIBK (methyl isobutyl ketone) and Isopropanol. PMMA is often used in conjunction with copolymer MMA. The vastly different development speeds allow the formation of controlled undercuts for lift-off processes (see section 4.2.1 below) or, for example, the formation of T-shaped gates for HEMT applications. Fig. 4.4 (left) shows a typical contrast curve for PMMA.

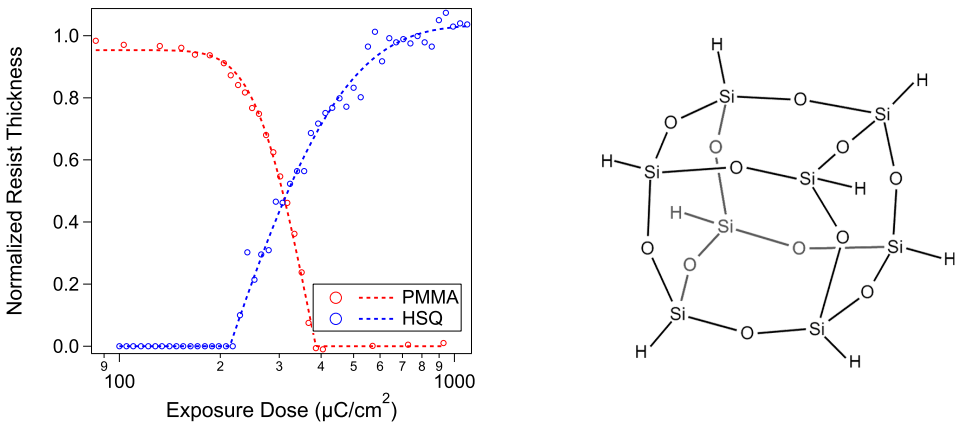

Figure 4.4: **(left)** Experimentally measured contrast curve, with fits, of PMMA (red) and HSQ (blue) used in this work. The corresponding spinning, baking and development parameters can be found in appendix A. **(right)** Schematic picture of the cage-like HSQ molecule.

Hydrogen Silsesquioxane (HSQ)

Hydrogen silsesquioxane (HSQ) is a well-investigated negative tone inorganic resist [82, 83] known for its high contrast, ultra high-resolution ($< 10\,\mathrm{nm}$) electron beam lithography (EBL) capabilities [84] and its stability against dry etching [85]. Like many high-resolution resists, HSQ requires a very high exposure dose - of the order of $8\,\mathrm{mC/cm^2}$[1] - which makes its use unrealistic for large features. However, thanks to its very high contrast and chemical composition, HSQ will not be subject to over development, therefore, prior to any etching step, one can spin another resist and do a subsequent lower resolution/lower dose lithography step.

The HSQ molecules consist of a cage-like structure with a silicon atom at each corner with a hydrogen atom covalently bonded to them. The edges of the cage are formed by oxygen atoms resulting in the stoichiometric formula $\left(\mathrm{HSiO}_{3/2}\right)_8$ for a unit cell as depicted in Fig. 4.4 (right). The high resolution capabilities of HSQ result from its small molecule size and exposing HSQ with accelerated electrons leads to cross-linking of the unit cells via breaking Si-H and Si-O bonds and forming new Si-O-Si bridges [86].

Three different processes are commonly used to develop HSQ. The first two consist of TMAH aqueous solutions, either a low concentration (less than 3%) or high concentration

[1] This dose is one to two orders of magnitude larger than typical exposure doses.

(more than 25%), respectively known as low- and high-contrast developers. Lastly, HSQ can also be developed by the so-called salty developer, consisting of aqueous solution of sodium hydroxide (NaOH 1%) and sodium chloride (NaCl 4%). Fig. 4.4 (left) shows a typical contrast curve for HSQ.

Because of the extremely high exposure dose required to form the hardened cross-linked HSQ mask and the proximity effect (see section 4.2.5 for more details), a common problem with HSQ is the formation of small agglomerates of partially exposed resist that are not completely dissolved during development. These small particles tend to accumulate on the edges of developed structures and act as micro-masks when the pattern is etched. Due to the inorganic nature of HSQ, these agglomerates cannot be removed by descumming in an oxygen plasma (see next section), but their formation can be mitigated by a careful optimization of the resist development [87].

Resist Descumming (Ashing)

When using organic resists, it is not uncommon to find resist residues in the developed areas or on resist edges. Such residues can greatly affect the quality of the etching by acting as small "micro-masks": the residues locally protect the surface to be etched, leading to a large surface roughness of the etched layer. Fig. 4.5 (left) shows a typical example of the effect of micro-masking on an etched layer. In a lift-off process, these residues will get trapped under the subsequently deposited layer. If the device is heated again, the residues will reflow and greatly affect the uniformity of the layers deposited atop as depicted in Fig. 4.5 (right).

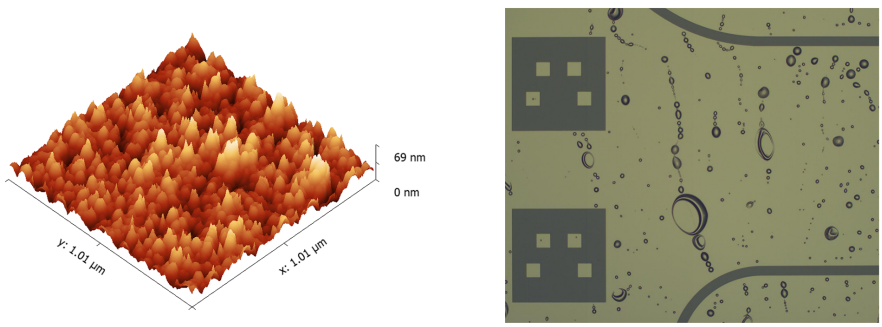

Figure 4.5: **(left)** Atomic force microscope micrograph highlighting the high surface roughness of a Si substrate after micro-masking. **(right)** Optical microscope picture of bubbles of reflowed resist underneath a gold layer after an improper substrate cleaning.

To prevent these unwanted situations, right after development, the wafer is placed in a mild oxygen plasma (10 W to 50 W) for a few seconds. The oxygen ions strongly react

with any organic material, effectively removing the residues. However, this process affects the entire resist layer: it is therefore important to consider the resist etching rate and carefully choose the duration of the ashing step for an optimal result. Alternatively, for extremely thin layers of resist or sensitive materials, resist can be ashed in an ozone chamber instead.

In the specific case of HSQ and other spin-on glass resists, an oxygen plasma step can be done to strengthen the resist mask against reactive ion etching: the oxygen ions in the plasma increase the density of the silicon oxide mask.

Resist Removal

A strong oxygen plasma ($> 100\,\mathrm{W}$) can be used to strip organic resists very efficiently, however this is not always suitable if other parts of the device are sensitive to oxygen or oxidation (for example in the case of graphene based devices). Alternatively, most exposed and unexposed organic resists can be washed away using certain solvents.

NMP (N-methyl-2-pyrrolidone) based removers offer the greatest effectiveness for removal of most organic resists, however, NMP is highly toxic and is listed as a Substance of Very High Concern (SVHC) by the European Union [88]. Therefore, several safer alternatives have been developed, however with greatly reduced effectiveness for the removal of strongly cross-linked resists. For sensitive devices, a more gentle (but less efficient) resist removal can be done using acetone.

In the specific case of HSQ and other spin-on glass resists, the silicon oxide mask can be removed either by dry etching in fluorine chemistry or by wet etching using hydrofluoric acid (HF).

4.2.3 Contact Photolithography

Contact lithography is performed in a tool called *mask aligner*. Such a system consists of an intensive UV light source, an optical microscope, a mask holder and a precision stage on which the substrate to be exposed is located. The microscope and the stage can be used to align the mask to preexisting features on the sample. Masks are typically made of a thin chromium layer patterned with the desired circuit layout on top of a soda lime or quartz glass substrate. During the exposure, the UV light shines on the mask and exposes the resist in the areas opened in the chromium mask.

The theoretical minimum feature size d_{min} is given by [89]

$$d_{min} = \frac{3}{2}\sqrt{\lambda\left(g + \frac{1}{2}h\right)} \tag{4.2}$$

where λ is the wavelength of the UV light source, g is the gap between the mask and the photoresist and h is the thickness of the resist.

At a resist thickness of 500 nm and assuming a perfect contact between the mask and the resist ($g = 0$), for $\lambda = 365\,\text{nm}$ (i-line), we obtain $d_{min} \simeq 450\,\text{nm}$. Realistically, accounting for imperfections in the resist thickness and mask contact, resolutions of the order of 700 nm to a micrometer are achievable in contract lithography. In a similar way, for DUV lithography, at $\lambda = 240\,\text{nm}$, $d_{min} \simeq 350\,\text{nm}$. Once again, taking into account imperfections in the aligner and the process, a practical resolution is of the order of 500 nm.

These resolutions are suitable for most microfabrication processes, however, while contact lithography excels in speed (an exposure is done in a matter of seconds), it severely lacks in flexibility: masks are costly to produce and only last for a limited number of exposures. Moreover, in a research environment where designs often change, it is unrealistic to make a new mask every time.

4.2.4 Maskless Photolithography

A popular alternative to mask aligners for optical lithograhy are the so-called *direct write* system where a high resolution laser is used to expose photoresist. Laser writers are typically used for photomasks and stepper reticles production, but can also be used for maskless direct patterning of substrates. Because they eliminate the need for a mask, laser writers offer tremendous flexibility and are of great interest in a research environment.

The minimum achievable feature size is comparable to standard UV contact lithography ($\sim 1\,\mu\text{m}$) and writing speeds are typically around $100\,\text{mm}^2/\text{min}$.

4.2.5 Electron Beam Lithography

While photolithography is a fast and cost-effective process, it is however limited in resolution as detailed in the previous sections. To overcome this resolution limit, an e-beam lithography (EBL) system can be used. An EBL system consists of an electron gun, a collimator, magnetic lenses, beam blanker and deflecting coils [90]. In the electron gun, electrons extracted from a filament are accelerated by an electric field. This stream of electrons is then focused by the collimator and magnetic lenses. The position of the focused electron beam can then be controlled using the deflecting coils. By raster or vector scanning the beam over the surface of a substrate covered with a resist sensitive to electrons, a pattern can be directly written without the need of any mask.

The wavelength of the electrons is given by the de Broglie's relation [91]

$$\lambda_e = h/p_e = \frac{h}{\sqrt{2m_e\varepsilon_{kin}}} \tag{4.3}$$

where $p_e = \sqrt{2m_e\varepsilon_{kin}}$ is the momentum of the electrons, m_e the mass of the electron and ε_{kin} the kinetic energy of an electron. At an acceleration voltage of 100 kV (ie. a kinetic

energy $\varepsilon_{kin} = 100\,\text{keV}$), the wavelength of the electrons is on the order of $\lambda_e = 4\,\text{pm}$. This makes electrons the ideal candidate for ultra-high resolution applications. In fact, in practice, resolution in an EBL system is not limited by the wavelength of the electrons but by technical limitations of the collimator and coils to focus the beam spot size below a few nanometers.

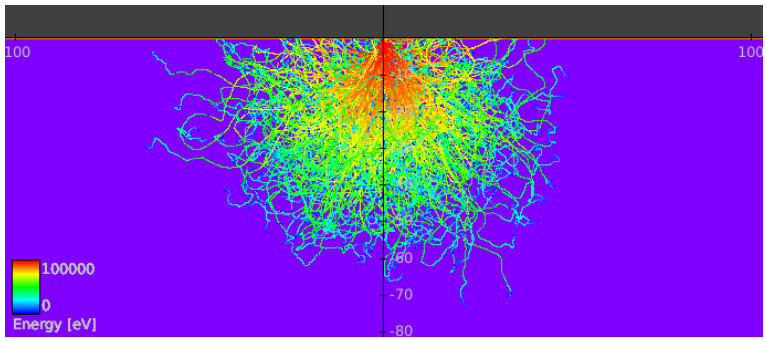

Figure 4.6: Simulated trajectories of electrons penetrating a 400 nm thick PMMA 950k A6 layer on top of a Silicon substrate. The simulation is carried out for an acceleration voltage of 100 kV. The color scale represents the electrons energies.

When the beam electrons (primary electrons) reach the sample, they scatter inelastically with the resist or substrate atoms and generate secondary electrons that cause a beam broadening (forward scattering). Electron trajectories in the resist and substrate can be simulated using Monte Carlo simulations as shown in Fig. 4.6. The low energy ($\sim 50\,\text{eV}$) secondary electrons are responsible for the exposure of the resist.

Higher acceleration voltages reduce the forward scattering angles and therefore increase the resolution, however at high kinetic energies, the primary electrons are likely to elastically scatter on the substrate atoms at large angles. Because of their high energies, these backscattered electrons can in turn scatter into secondary electrons and expose the resist outside of the intended region. This unwanted exposure is known as the *proximity effect*.

In an EBL system, the deflecting coils are used to direct the beam off-axis, but the maximum deflection distance is limited since any motion too far from the center causes aberrations that deteriorates the spot geometry and affects resolution. The maximum area within which the system can write without any appreciable decline in resolution is called a *write field*. The deflection system is generally controlled by the pattern generator, usually at a resolution of 16 bits or higher, and each possible position within the write field is placed on a grid on which the beam can jump. The *beam step* δ is an integer multiple of the grid size and corresponds to the distance between each beam movement during a given exposure. The exposure dose received by the resist, defined as the total charge deposited in the resist per unit area, can therefore be calculated by

$$D = \frac{I_{beam}\tau_{dwell}}{\delta^2} \tag{4.4}$$

where I_{beam} is the beam current and τ_{dwell} is the exposure time of a single pixel. By controlling the dwell time τ_{dwell}, the exposure dose received by the resist can be changed.

If one is able to accurately predict the effective dose received by a given area of resist, the proximity effect due to the beam broadening and backscattering can be compensated by adjusting the exposure dose on the fly. Simulations of the electron trajectories as depicted in Fig. 4.6 allows the calculation of the *point spread function* which describes the deposited energy induced by forward and backward scattered electrons. Because Monte Carlo simulations are computationally intensive, the point spread function has traditionally been approximated by the sum of two Gaussian functions, however this model is limited and does not describe well the behaviour of modern systems with high acceleration voltages. Fig. 4.7 (left) shows an example of the effective contributions of both traveling and backscattered electrons in the two-Gaussian approximation. Fig. 4.7 (right) gives a comparison between the point spread function calculated using a Monte Carlo simulation and the two Gaussian model: while good agreement is obtained for small and large radii, the middle region is not correctly captured by the model.

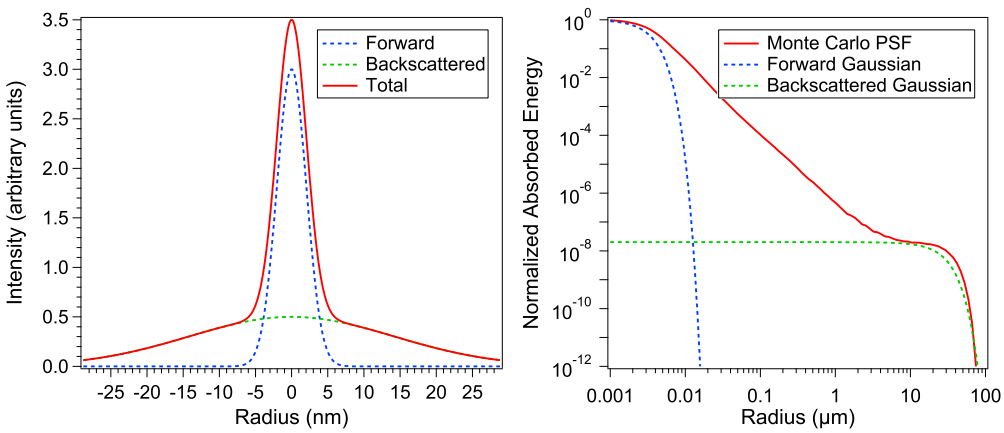

Figure 4.7: **(left)** Example of a double Gaussian distribution approximation of both forward traveling and backscattered electrons. **(right)** Monte Carlo simulation at 100 kV of the point spread function normalized to the absorbed energy at $r = 0$ for a stack of 400 nm PMMA / 20 nm NbN / 250 µm Si. The dashed lines represent the corresponding double Gaussian approximation.

The simulated point spread function can be taken into account during the pattern preparation in a step called *proximity effect correction* where the dose at every beam step is modulated accordingly. Fig 4.8 shows examples of a pattern exposed with proximity correction. Each colored region corresponds to a different modulated exposure dose.

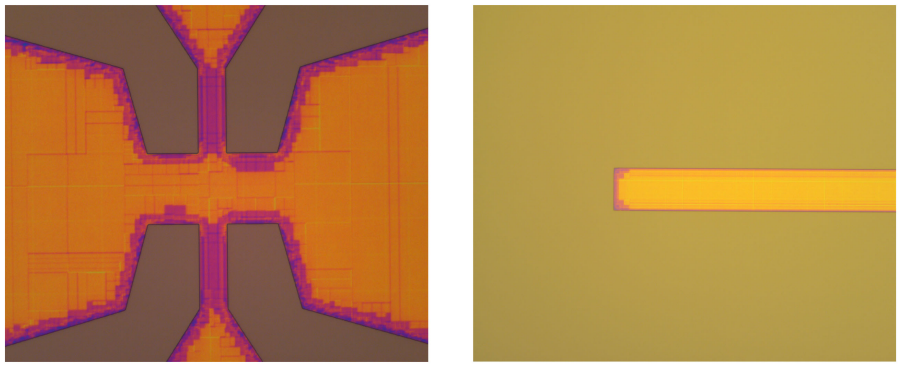

Figure 4.8: Optical micrograph examples of electron beam lithography resist exposed with proximity effect correction. Each colored region corresponds to a different exposure dose in the resist.

4.3 Thin-film Deposition: Sputtering

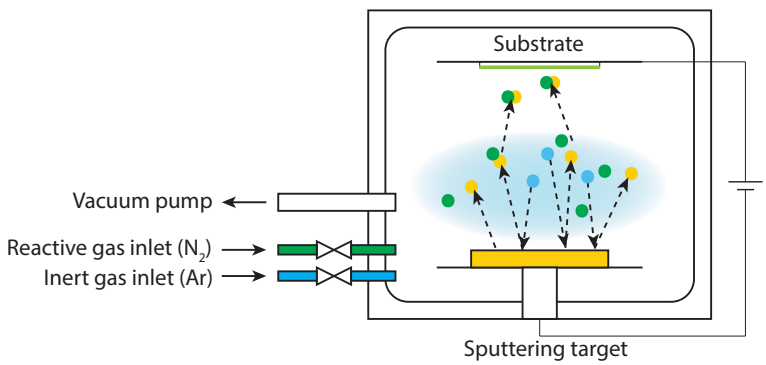

Figure 4.9: Schematic diagram of a typical DC magnetron sputtering system. The argon ions (blue dots) collide with the sputtering target and eject niobium atoms (yellow dots). The niobium atoms react with the nitrogen ions (green dots) and form niobium nitride that then deposit on the substrate.

Sputtering is a common thin-film deposition technique suitable for a broad selection of materials, ranging from metals to dielectics. As with any thin-film deposition technique, sputtering offers both advantages and drawbacks. For example, sputtering allows for the uniform deposition of ultra-thin films - down to a thickness of a few nanometers - but the substrate significantly heats up during the process, making it virtually impossible to deposit a film on resist mask for a lift-off process. Sputtering offers a unique range of parameters that can be tuned to affect the properties of the resulting thin film: thickness,

stoichiometry, epitaxial to disordered layers, compound materials...

The substrate is loaded in a vacuum chamber and placed directly in front of the source of the material to be deposited (the *sputter target*). A controlled flow of a high-Z neutral gas (typically argon) is let in the chamber and a DC voltage bias is applied, creating a plasma above the target. In the plasma, the argon ions are bombarded in all directions at high velocities. When an ion collides with the sputter target, it transfers its momentum to the surface and one or more atoms of the target are ejected. If the substrate is in the path of the ejected atoms, they will nucleate on the surface and form a thin film. In addition to the sputtering gas, a reactive gas can be introduced in the chamber. The reactive gas is ionized as well and the ions reacts with the ejected atoms, forming compounds, before they reach the substrate. This process is called *reactive sputtering* and the stoichiometry of the deposited film can be controlled by manipulating the partial pressure of the reactive gas in the chamber.

A metallic lid (the *shutter*) is used to obstruct the path between the target and the substrate to prevent deposition. The shutter is used at the start of the process, until the conditions in the chamber are stable, and once the target thickness is achieved. Fig. 4.9 shows a schematic view of a typical DC-magnetron sputtering chamber with a reactive gas inlet.

4.4 Etching Techniques

4.4.1 Ion Milling

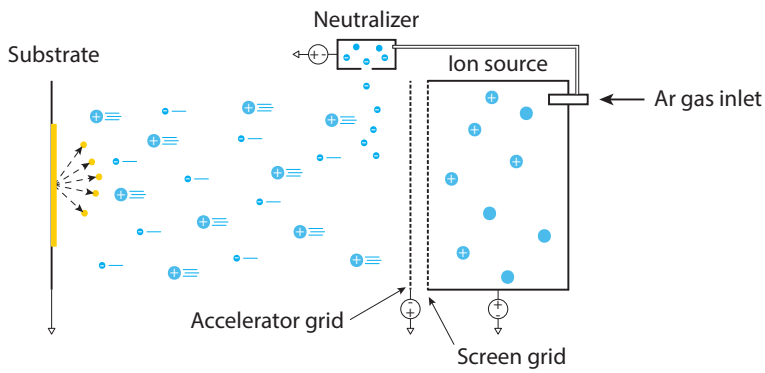

Figure 4.10: Schematic diagram of a typical ion beam etching system. The argon atoms are ionized in the source and accelerated toward the substrate. The neutralizer emits electrons to balance the charge in the beam. When the argon atoms reach the substrate, the surface atoms are sputtered away.

Ion milling is a physical etching technique in which ions of an inert gas (typically Ar) are used to remove material from a substrate to some desired depth. When leaving the source,

the ions are collimated into a wide beam by the *screen grid* and accelerated toward the surface of a substrate by the *acceleration grid*. When reaching the surface, the atoms from the material to be etched are sputtered away. In a naive picture, ion milling can be compared to sandblasting with ions.

Because of the directionality of the beam, ion milling is a highly anisotropic etching technique. Moreover, due to the mechanical nature of the process, ion milling does not suffer from potential unwanted chemical reactions and is a suitable etching method for any material, however at the cost of a low selectivity to the mask. Additionally, the main drawback of ion milling is the redeposition of the sputtered atoms on the sidewalls of the resist mask, leading to the formation of "fences" after the resist is removed (see Fig. 4.11). This can be mitigated by rotation the substrate and etching at an angle, but at the cost of sloped etch profile.

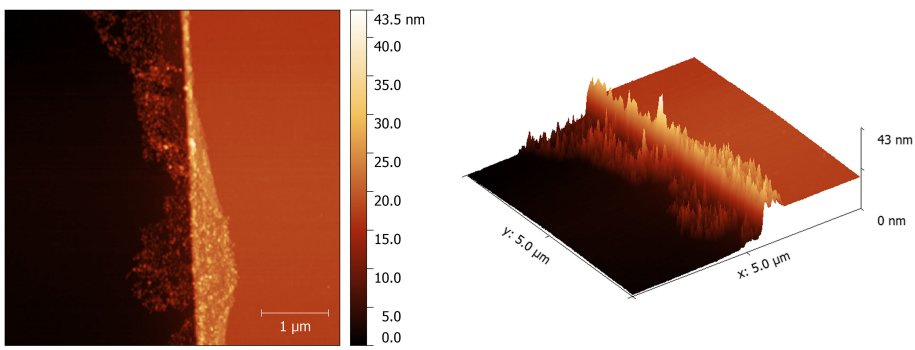

Figure 4.11: AFM micrographs of redeposition after ion milling of NbN. The large surface roughness observable near the side wall are redeposition fences that collapsed when the resist was removed.

4.4.2 Reactive Ion Etching

Reactive ion etching (RIE) is a popular type of dry etching that uses chemically reactive plasma to remove material on substrates. A RIE system consists of a vacuum chamber equipped with parallel electrodes AC coupled to a voltage source through a matching network. The substrate to be etched is loaded on the bottom electrode (the *platen*). A small inlet lets in the chamber a controlled flow of one or more process gas. During a process, the pressure in the chamber is of the order of a few mTorr and is controlled by a throttle valve placed in front of the vacuum pump. A plasma is initiated in the chamber by applying a strong radio frequency (RF) electromagnetic field to the platen.

The oscillating electric field ionizes the process gas molecules by stripping them of electrons. In each cycle of the field, the electrons are electrically accelerated up and down in the

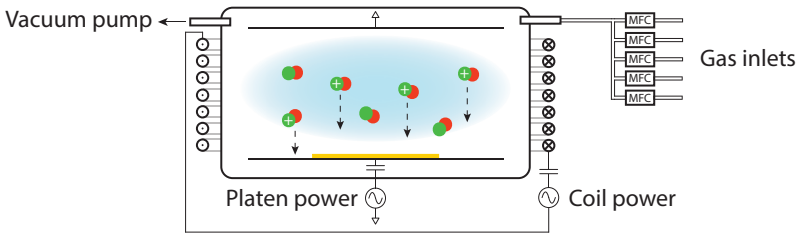

Figure 4.12: Schematic diagram of a typical reactive ion etching chamber. The reactive gas flows are controlled by several mass flow controllers (MFC) and the vacuum pump regulates the pressure in the chamber. The platen and ICP sources provide the necessary RF power to create a plasma. Due to the negative charge build up on the substrate platen, the ions drift toward the substrate and react with the surface, etching it away.

chamber and at the same time, the much more massive ions move relatively little in response to the RF electric field. When electrons are deposited on the substrate platen, this causes the electrode to build up a charge due to its DC isolation. This charge build up translates to a large negative voltage on the platen, typically around a few hundred volts, while the plasma itself develops a slightly positive charge due to the higher concentration of positive ions compared to free electrons.

Because of the large voltage difference, the positive ions tend to drift toward the wafer platen, where they collide with the samples to be etched and react chemically with the materials on the surface of the samples. Heavy ions can also sputter some material by transferring some of their kinetic energy. Due to the mostly vertical delivery of reactive ions, reactive ion etching can produce highly anisotropic etch profiles.

Additionally, a coil can be wound around the chamber and the plasma can be generated by an RF powered magnetic field inductively coupled into the chamber. Inductively coupled plasma (ICP) can be much denser than platen generated plasma, however, due to the lack of negative charge build up, the etch profiles produced will be isotropic. ICP and platen plasma can be combined to benefit from the high density of the ICP and the directionality due to the bias.

Etch conditions and profiles in an RIE system depend strongly on the many available process parameters, such as pressure, gas flows, and RF power. Fig. 4.12 shows a schematic view of a typical RIE system.

4.4.3 Etching of disordered NbN

Disordered materials such as niobium nitride are challenging to etch. Traditionally, nitrides are dry etched in RIE using fluorine chemistry gas such as SF_6, NF_3 or CHF_3. However, the etching rates of Nb and NbN with these chemistries greatly differ (by almost a factor of 10). In the case of disordered NbN, grains may have slight variations in

stoichiometry, resulting in small to large variations in the etching speed. In a similar way to improperly cleaned resist, this manifests itself by a micro-masking effect and leads to a large surface roughness. Ion milling is not suitable either due to redeposition and the need for sharp etch profiles

To overcome these issues, we developed a "best of both worlds" etch process of disordered NbN using an in-situ combination of a highly anisotropic physical Ar etch with a mild RIE at a low concentration of Cl_2. Low gas pressures allow for good anisotropy due to a high DC bias in the RIE chamber. Additionally, with careful tuning of the reactive gas partial pressure, the redeposition due to the Ar physical etch can be mitigated and a good control of the etch profile can be achieved as depicted in Fig. 4.13.

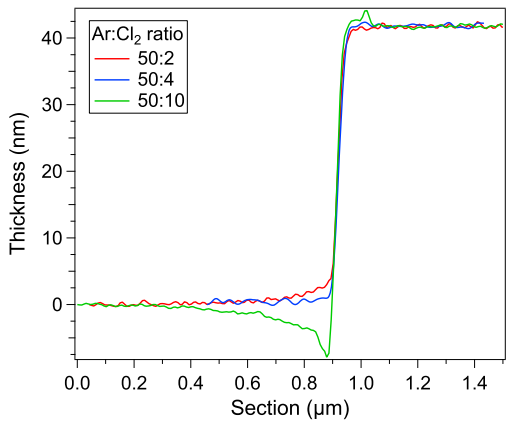

Figure 4.13: Cross section of AFM scans of the etched profile of NbN on top of a Si substrate for various Ar : Cl_2 ratios. At too low/high Cl_2 partial pressures (red/green), bunching/trenching of material is observed at the base of the etch profile.

4.5 Device Fabrication

This section describes a generic fabrication process flow for the devices used in this work. Details of the fabrication recipes can be found in appendix A.

Samples are fabricated on high-resistivity ($\rho \geq 10\,\mathrm{k\Omega\,cm}$) (100) intrinsic silicon substrates. Before processing, the substrate is dipped in hydrofluoric acid (HF) for 30 s to remove any surface oxide. Within 5 min, the wafer is loaded into a DCA MTD 450 near-UHV sputtering system where a 20 nm thick NbN thin film is deposited by reactive DC magnetron sputtering from a 99.99 % pure Nb target in a 6:1 Ar:N_2 atmosphere.

A 500 nm-thick layer of PMMA A6 resist is spin-coated and then exposed with either a JEOL JBX-9300FS 100kV or a Raith EBPG5200 100kV electron beam lithography system to define the microwave transmission lines and alignment marks. After development, the

pattern is transferred to the film by reactive ion etching in an Oxford Plasmalab 100 RIE system with a 50:4 Ar:Cl_2 plasma at 50 W and 10 mTorr.

The nanowires are then patterned in a subsequent EBL exposure using a 50 nm layer of hydrogen silsesquioxane. After development, and since HSQ is a negative resist, only the nanowires are covered by the resist mask. Therefore, in order to protect the patterns defined in the previous exposure, before any further etching, a 500 nm-thick layer of S1805 photoresist is spin-coated and exposed in an Heidelberg DWL2000 laser writer. The photoresist is only open in a 150 µm × 200 µm area around each nanowire. Fig. 4.14 shows micrographs of a typical device.

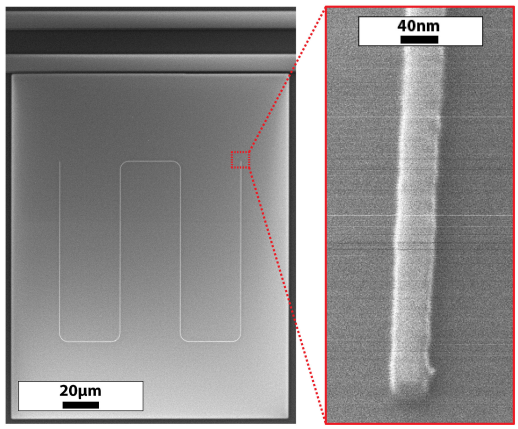

Figure 4.14: **(left)** Scanning electron microscope (SEM) micrograph of a nanowire resonator coupled to its feed line; the NbN feed line and ground plane are shown in black, the Si substrate is in gray, and the 40 nm × 680 µm nanowire is light gray. **(right)** A helium focused ion beam (FIB) image of the nanowire.

4.6 Fabrication Quality

In order to assess the quality of the fabrication, our devices have been imaged with a helium focused ion beam (FIB) microscope at the London Centre for Nanotechnology, University College London. He FIB imaging offers unmatched resolution and gives extremely valuable insight on the device geometry at the nanometer scale.

The micrographs (Fig. 4.15) reveal very sharp nanowires on a smooth substrate surface. The line edge roughness of the nanowires is of the order of a nanometer or less. Moreover, we estimate a lithographic defect rate of less than 3 defects per 10 µm.

The defects are 10 nm wide or less. Because they are transferred into the superconducting film during etching, the defects contribute to the effective surface area of the nanowire. For a typical 680 µm long and 40 nm nanowire, this translates to an uncertainty in the surface area of 1% or less.

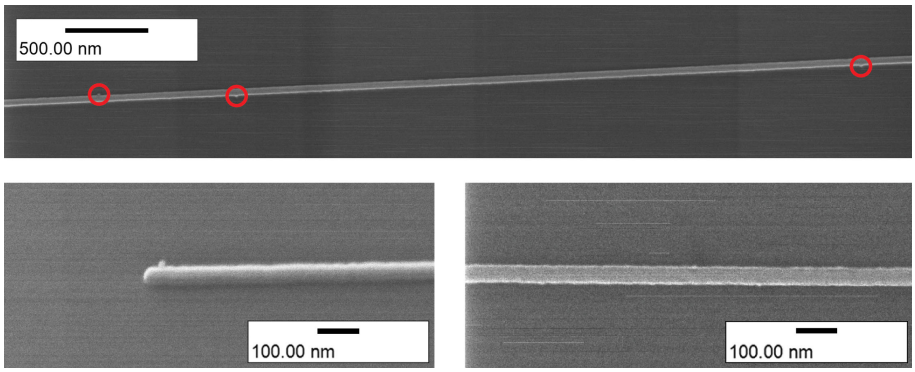

Figure 4.15: Helium FIB micrographs of a nanowire superinductor. **(top)** Shows a low magnification image of a long section (5.5 µm) of the nanowire. Lithographic defects are circled in red. **(left)** Shows a high magnification image of the end of the nanowire. Here we can see the defect is approximately 10 nm wide. **(right)** Shows a high magnification image of a section of nanowire without defects. Here we see the edge roughness is approximately ±1 nm.

Chapter 5

Measurement Techniques

5.1 Pound Frequency Locking

5.1.1 Homodyne and Heterodyne Detection Techniques

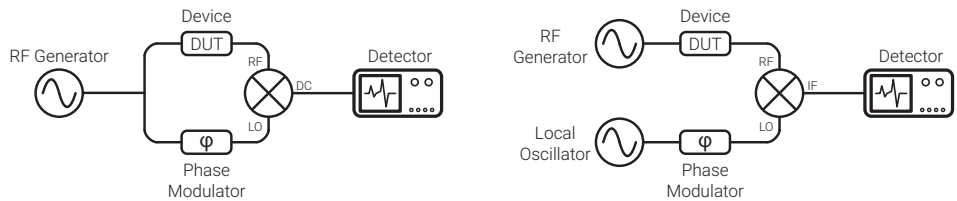

Figure 5.1: Schematic of a simple homodyne **(left)** and heterodyne **(right)** detection setup.

The two most common techniques used for measuring the amplitude and phase of a high frequency signal are called *homodyne* and *heterodyne* detection. In a homodyne detection scheme (Fig. 5.1(left)), a source signal is split into two paths, one path goes through the device under test (DUT), the other is used as a reference signal. The two signals are mixed, which allows for the recovery of the phase response of the DUT by measuring the phase difference $\delta\varphi$ between the two paths. The output signal after the mixer is a DC signal proportional to the average the amplitudes of the reference signal and response of the DUT, modulated by the cosine of the phase difference. Homodyne detection is the simplest method to implement experimentally, however it is particularly sensitive to low frequency noise.

This limitation can be overcome in an heterodyne detection scheme (Fig. 5.1(right)), in which the reference signal is generated by a second source (the local oscillator) at a frequency f_2 different from the frequency f_1 of the signal sent through the DUT. The response of the DUT is encoded in the amplitude of the signal at the output of the mixer. This signal is at a frequency $f_1 - f_2$ and can be set well above the cut-off frequency for low frequency noise by adjusting the frequency of the local oscillator.

Both these techniques, however, are limited by non-correlated fluctuations in the signal and reference lines.

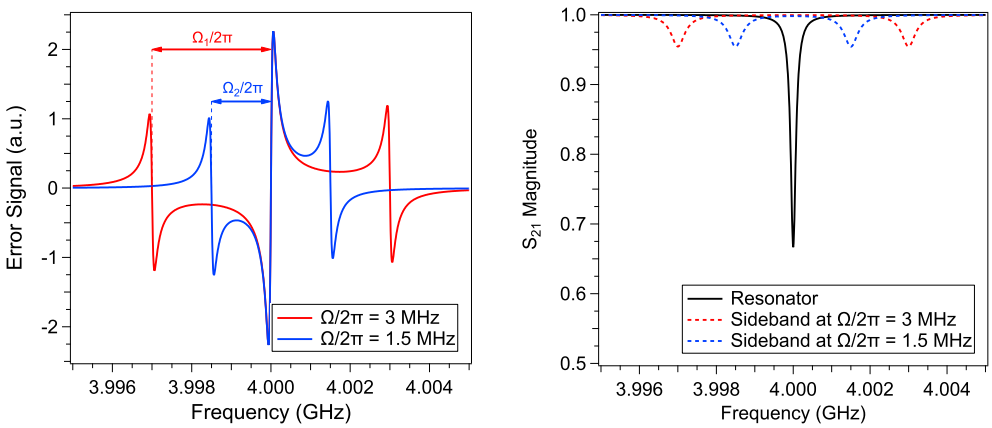

Figure 5.2: **(left)** Error signal for two different side band frequencies. **(right)** S_{21} magnitude response of the corresponding resonator. The dashed lines indicate the location of the side bands.

5.1.2 Pound Locking Theory

In this work, for the intrinsic loss tangent measurements (see chapter 6), we have used a technique called Pound frequency locking that enabled us to track the frequency changes of our nanowire resonators against temperature with unmatched accuracy. Originally developed to stabilize microwave oscillators [92], this technique is commonly used in optics for frequency stabilization of lasers [93] and has been recently used for noise [72, 94] and ESR [3, 95] measurements with superconducting microwave resonators. The major advantage of this technique is that it can be used to very accurately measure in real time the frequency of any device with a nonlinear phase response. In practice, the bandwidth is only limited by the bandwidth of the control electronics, typically working up to 100 kHz or more.

The Pound frequency locking technique can be thought of a type of heterodyne detection where a phase modulated signal is used instead of a separate local oscillator. A self-mixing power law detection results in an interference between the phase modulated side bands and the main signal. The resulting interference signal is fed through a lock-in amplifier and a PID controller that seek to obtain complete destructive interference. A major advantage of this technique (in particular in a cryogenic environment) is that any phase noise is correlated and will therefore affect the carrier and side bands in a similar way and cancel out.

In the following, we give a brief description of the governing equations of a Pound frequency-locked loop (P-FLL). We start by considering a phase modulated signal, which can be expressed as

$$A = A_0 e^{i\omega t + \beta i \sin(\Omega t)} \tag{5.1}$$

where $\Omega/2\pi$ is the phase modulation frequency and β is the modulation depth. Using the Jacobi-Anger expansion, we can rewrite Eq. 5.1 as

$$A = A_0 e^{i\omega t} \sum_{n=-\infty}^{\infty} J_n(\beta) e^{in\Omega t} \tag{5.2}$$

where $J_n(\beta)$ is the n-th Bessel function of the first kind. If β is small, higher order terms can be neglected since $\lim_{n\to\infty} |J_n| = 0$. A first order development of Eq. 5.2 leads to

$$\begin{aligned} A &\simeq A_0 \left[J_0(\beta) e^{i\omega t} + J_1(\beta) e^{i(\omega+\Omega)t} - J_1(\beta) e^{i(\omega-\Omega)t} \right] \\ &= A_0 e^{i\omega t} \left[J_0(\beta) + 2i J_1(\beta) \sin(\Omega t) \right] \end{aligned} \tag{5.3}$$

Sending this phase modulated signal through a DUT characterized by a transmission $S(\omega)$ will give the following output signal:

$$A_{out} = A_0 \left[S(\omega) J_0(\beta) e^{i\omega t} + S(\omega+\Omega) J_1(\beta) e^{i(\omega+\Omega)t} - S(\omega-\Omega) J_1(\beta) e^{i(\omega-\Omega)t} \right] \tag{5.4}$$

Feeding this signal to a self-mixing power law detector diode gives (neglecting the 2Ω terms):

$$\begin{aligned} P_{out} = |A_{out}|^2 = {} & P_0 J_0^2(\beta) S^2(\omega) + P_0 J_1^2(\beta) \left[S^2(\omega+\Omega) + S^2(\omega-\Omega) \right] \\ & + 2P_0 J_0(\beta) J_1(\beta) \Big[\mathrm{Re}\left[S(\omega) S^*(\omega+\Omega) - S^*(\omega) S(\omega-\Omega) \right] \cos(\Omega t) \\ & + \mathrm{Im}\left[S(\omega) S^*(\omega+\Omega) - S^*(\omega) S(\omega-\Omega) \right] \sin(\Omega t) \Big] \end{aligned} \tag{5.5}$$

If the DUT is a resonator and if we assume that the side bands do not enter the resonator, we have $S(\omega \pm \Omega) \simeq 1$, which leads to

$$S(\omega) S^*(\omega+\Omega) - S^*(\omega) S(\omega-\Omega) \simeq S(\omega) - S^*(\omega) = 2i\,\mathrm{Im}\left[S(\omega) \right] \tag{5.6}$$

This is purely imaginary, which means that the $\cos(\Omega t)$ term in Eq. 5.5 is negligible. After measuring the remaining $\sin(\Omega t)$ signal using a lock-in amplifier, we get the following *error signal*:

$$\varepsilon = 2P_0 G J_0(\beta) J_1(\beta)\, \mathrm{Im}\left[S(\omega) S^*(\omega+\Omega) - S^*(\omega) S(\omega-\Omega) \right] \cos(\Delta\varphi) \tag{5.7}$$

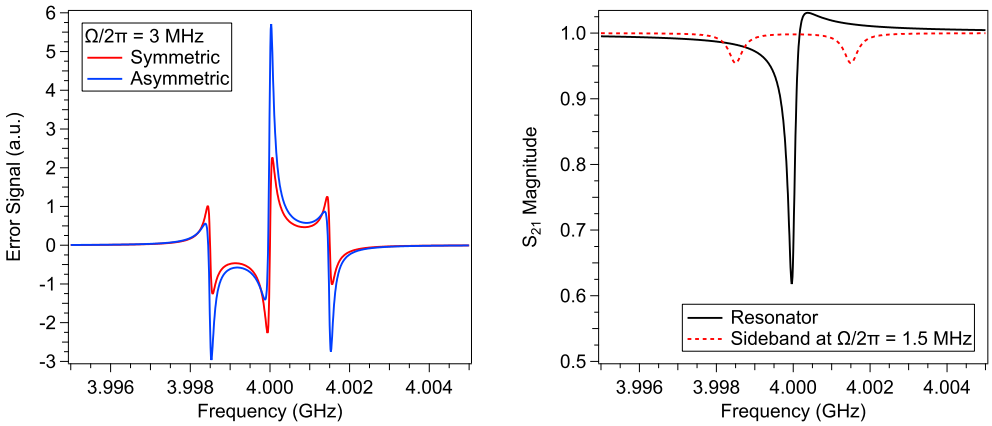

Figure 5.3: **(left)** Comparison between the error signal for a symmetric (red) and an asymmetric (red) resonator with the same side band frequency. **(right)** S_{21} magnitude response of the asymmetric resonator. The dashed lines indicate the location of the side bands.

where G is the gain of the loop and $\Delta\varphi$ represents the phase difference between the measured signal and the reference signal in the lock-in amplifier. The zero crossing of the error signal happens for $\mathrm{Im}\, S(\omega) = 0$, which corresponds to the resonance frequency of the resonator. Fig. 5.2 shows a plot of the error signal corresponding to a typical resonator. Using a PID controller locked to the zero crossing of the error signal, we can track the center frequency of the resonator by sending the output signal of the PID to the frequency generator to adjust the carrier frequency, thus closing the Pound feedback loop.

In practice, the choice of modulation frequency is not particularly important as long as the side bands are sufficiently outside of the resonance dip of the resonator as shown in Fig. 5.2(right). If the side bands are too close to the carrier, they will inject power in the resonator and lead to a reduced phase shift and gain.

If the resonator response is asymmetric (see chapter 3), this leads to a non-symmetric error signal as shown in Fig. 5.3. In an asymmetric resonator, the minimum of the real response stops occurring at the same frequency as the phase zero-crossing. This situation results in an offset between the zero locking frequency and the resonator actual resonance frequency. The offset can however be compensated by using a non-zero set point on the PID controller, at the price of a becoming gain dependent, which complicates power sweeps.

5.2 Measurement Setups

5.2.1 DC Transport

The DC measurements in this work have been carried out either in a Quantum Design Physical Property Measurement System (PPMS) or in a ^{3}He cryostat. In any case, the samples are wire bonded to a custom sample holder equipped with $\sim 300\,\mathrm{kHz}$ low pass LC filters and all measurements are done using a standard 4-point method.

Hall effect measurements are carried out in PPMS at 15 K, with magnetic fields up to 6 T and using PPMS standard built-in resistance bridges. In the case of resistance against temperature ($R(T)$) characteristics measurements, the sample is installed on the cold stage of the ^{3}He cryostat. The temperature is controlled by gradually lowering the cryostat insert inside a liquid helium bath. This method, while rather basic, allows for a very precise control of the temperature and cooling speed. In this setup, the sample is current biased using a Yokogawa 7651 and the voltage is measured using a Keithley 2000 multimeter, with the eventual help of a Stanford Research SR560 voltage amplifier.

5.2.2 Microwave Measurements

The sample is wire-bonded in a connectorized copper sample-box that is mounted onto the mixing chamber stage of a Bluefors LD250 dilution refrigerator (Fig. 5.4). The inbound microwave signal is attenuated at each temperature stage by a total of 60 dB before reaching the device under test. Accounting for cable losses and sample-box insertion loss, the total attenuation of the signal reaching the sample is 70 dB. To avoid any parasitic reflections and noise leakage from amplifiers, the transmitted signal is fed through two microwave circulators (Raditek RADI-4.0-8.0-Cryo-4-77K-1WR) and a 4-8 GHz band pass filter. Finally, the signal is amplified by a LNF LNC4_8A HEMT cryogenic amplifier (45 dB gain) installed on the 2.8 K stage. Additional amplification is done at room temperature (Pasternack PE-1522 gain block amplifiers).

This microwave setup is connected to a vector network analyzer (Keysight PNA-X N5249A or R&S ZNB20) for initial characterization and quality factor measurements of the nanowire resonators at various excitation powers (see chapter 6).

5.2.3 Pound Frequency Locked Loop (P-FLL)

As described in section 5.1 and in chapter 6, we measure the resonance frequency of our nanowire resonators against temperature using the Pound locking technique. For that purpose, the microwave setup described in the previous section is included in P-FLL. The carrier signal is generated by mixing the output of a microwave source (Keysight E8257D) and a voltage controlled oscillator (VCO - Keysight 33622A). This carrier is

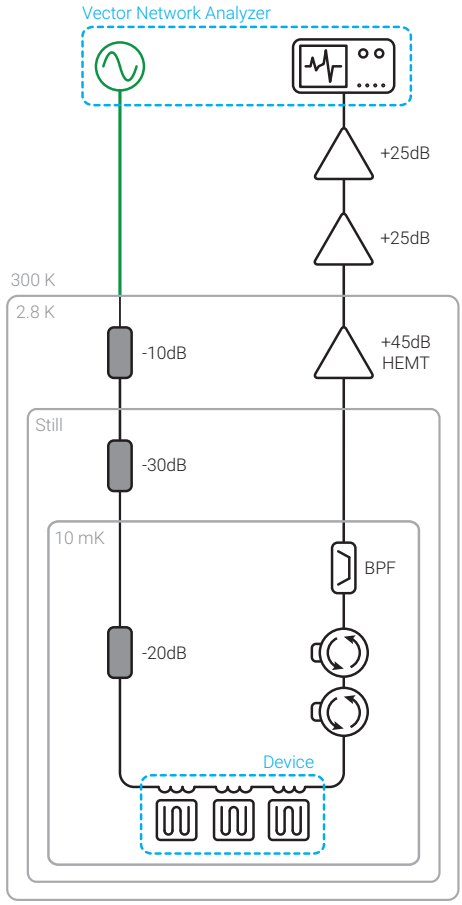

Figure 5.4: Standard cryogenic microwave measurement setup used in this work.

phase-modulated (Analog Devices HMC538) before being passed through the resonator under test. The phase modulation frequency is set so that the side bands are not interacting with the resonator. After amplification, the signal is filtered (MicroLambda MLBFP-64008) to remove the unwanted mixer image and rectified using an RF detector diode (Pasternack PE8016). The diode output is demodulated with a lock-in amplifier (Zurich Instruments HF2LI).

The feedback loop consist of an analog PID controller (SRS SIM960) locked on the zero-crossing of the error signal which gives an output directly proportional to any shift in resonance frequency of the resonator. This output signal is then used to drive the frequency modulation of the VCO, varying its frequency accordingly and enabling the loop to be locked on the resonator.

In this work, we only sample the PID output slowly ($\leq 100\,\mathrm{Hz}$) to track frequency changes (Keithley 2000), but noise in the resonator can also be studied using a frequency

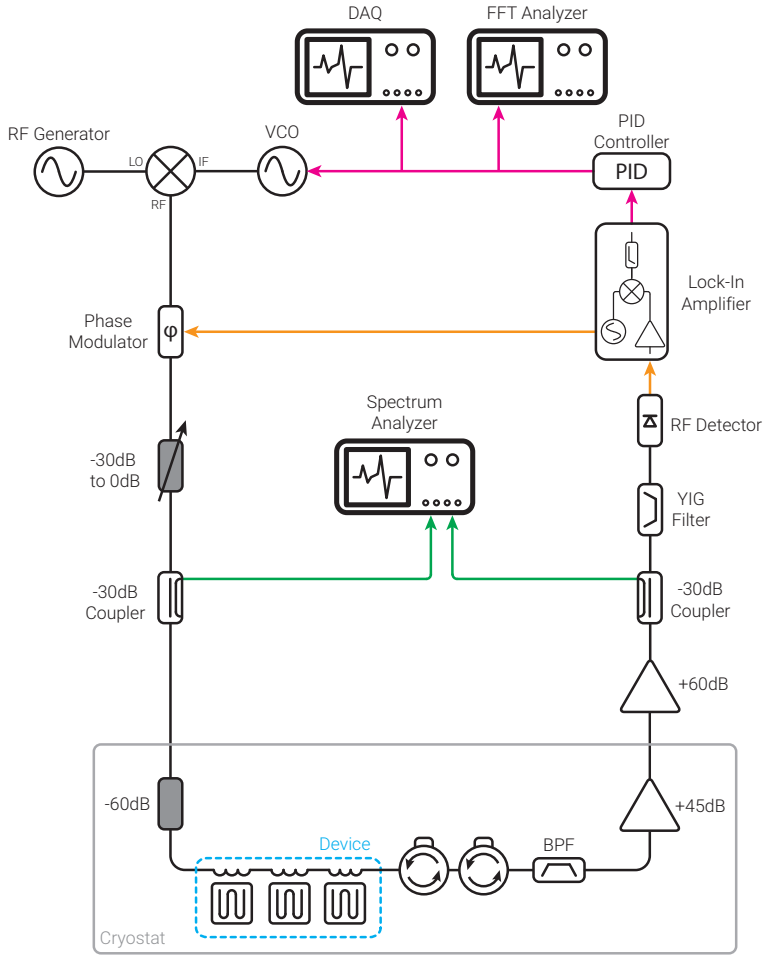

Figure 5.5: Pound frequency locked loop measurement setup.

counter (Keysight 53132A), a fast-sampling DAQ (NI PXI-6259 DAQ) or an FFT analyzer (Keysight 35670A).

Chapter 6

Nanowire Superinductors

In this chapter, we present the experimental characterization of nanowire superinductors. We start with a thorough analysis of the requirements for realizing a nanowire superinductor. We use simulations to highlight some design implications. We present experimental data on the fabrication and optimization of the high kinetic inductance disordered thin films used. Finally, we present a complete transport and microwave characterization of nanowire superinductors.

6.1 Device Design

As defined in the previous chapters, a superinductor is a low loss circuit element with an impedance larger than the superconducting resistance quantum R_Q. These prerequisites pose several constraints on the design of a successful superinductor: in the context of disordered superconductors, this implies that the thin film should have a high kinetic inductance while the fabricated structure should have a capacitance as low as possible.

In this section, we will detail the implications of these constraints on several aspects of the design of a nanowire superinductor.

6.1.1 Material Considerations

In chapter 2, we derived the kinetic inductance contribution for a superconductor in the local dirty limit (Eq. 2.46). This formula reveals that in order to achieve a highly inductive film, we need a superconductor that exhibits a high normal-state resistance R_N and a small superconducting gap (ie. a small critical temperature T_c).

However, there are several caveats in this simple interpretation. First of all, while a small gap is favourable for a high inductance, a working temperature too close to T_c leads to the presence of quasiparticles. In turn, these quasiparticles lead to significant losses, as highlighted in sections 2.2.1, 2.3.5 and 3.4. These losses would breach the low loss criterion for a superinductor, therefore this imposes a practical limit on the critical temperature of the superconductor to realize such device: for a practically obtainable temperature of 10 mK, the minimum practical critical temperature is around 1.5 K.

Additionally, while it is tempting to arbitrarily increase R_N (ie. the level of disorder) to achieve a high kinetic inductance, films exhibit loss as they get close to the SIT [68] (see section 3.4), which is once again incompatible with the low loss criterion for a

superinductor and imposes another practical limit on the superconductor: we need to fabricate a sufficiently disordered superconductor to obtain high inductance, but not so disordered as to induce dissipation.

In this work, our choice of superconductor is niobium nitride. NbN has a high bulk critical temperature (16 K), however the critical temperature is suppressed as the thickness of the film is reduced [96], which leads to a favourable scaling of the superconducting gap in Eq. 2.46.

After a careful optimization of the NbN thin film fabrication (see section 6.2 for more details), a target thickness of 20 nm, corresponding to a critical temperature $T_c = 7.20\,\mathrm{K}$ and a normal-state resistance $R_N = 503\,\Omega/\square$, is found as a good compromise between disorder and kinetic inductance, with a corresponding sheet kinetic inductance $L_k = 82\,\mathrm{pH}/\square$.

6.1.2 Geometrical Considerations

Nanowire Geometry

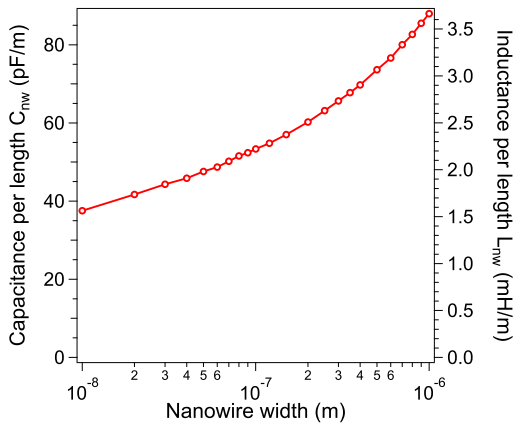

Figure 6.1: Simulated capacitance per length for nanowire widths ranging from 1 µm down to 10 nm. The right axis corresponds to the minimum required inductance per length to verify $Z_{nw} > R_Q$.

In the previous section, we established that we cannot arbitrarily increase the inductance to maximize the impedance. Therefore, to realize a superinductor, it becomes crucial to minimize the stray capacitance, which can be achieved with a nanowire geometry. We have simulated the capacitance per length for several nanowires with widths varying from 1 µm down to 10 nm. The results are shown in Fig. 6.1. This figure also shows the corresponding minimum inductance per length required for a superinductance.

Additionally, in chapter 2, we calculated the geometric contribution to the internal

inductance and find it to be entirely negligible for a thin film (see Eq. 2.35 and Fig. 2.4). Any given geometry will also have an external geometric contribution to its magnetic inductance which can be calculated, for similar nanowires, using an empirical formula [97]. It is found to be less than $1\,\mu\mathrm{Hm}^{-1}$ in every case. This number is several orders of magnitude smaller compared to the minimum inductance per length required for a superinductor (Fig. 6.1), we can therefore conclude that the nanowire inductance arises entirely from the kinetic inductance and that $L_{nw} \equiv L_k$.

For a thin film with a kinetic inductance $L_k = 82\,\mathrm{pH}/\square$, we find an inductance per length $L_{nw} = 2.05\,\mathrm{mH\,m}^{-1}$ for a 40 nm-wide nanowire. With a corresponding capacitance per length $C_{nw} = 44.4\,\mathrm{pF\,m}^{-1}$, we find $Z_{nw} = \sqrt{L_{nw}/C_{nw}} = 6.795\,\mathrm{k}\Omega > R_Q$, indicating that such nanowires are superinductors.

TLS Filling Factor

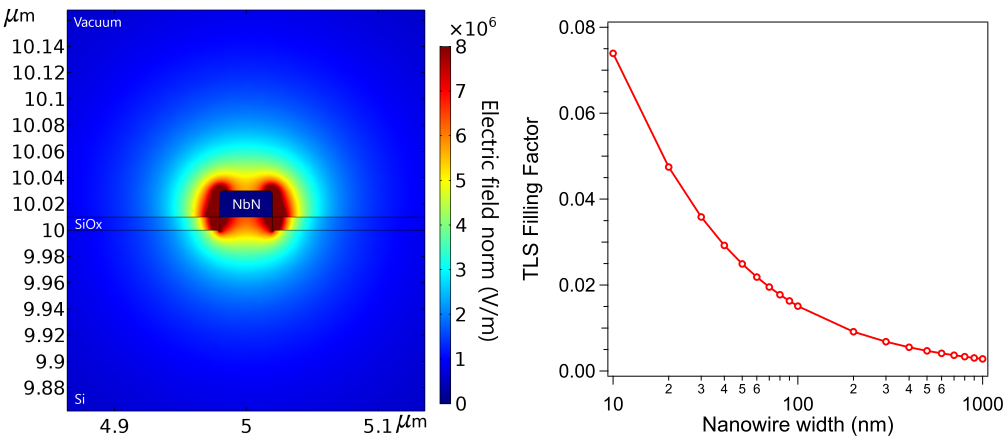

Figure 6.2: **(left)** Magnitude of the electric field for a 40 nm wide nanowire. **(right)** TLS filling factor for nanowire widths ranging from 1 µm down to 10 nm.

In chapter 3, we highlighted the role of the TLS filling factor in the losses and mentioned that reducing the physical dimensions of a resonator leads to an unfavorable scaling. We have simulated the TLS filling factor using an electrostatic simulation in Comsol for nanowires of various width. In our model, we assume a TLS host volume V_{TLS} consisting of a 10 nm thick layer of silicon oxide. The filling factor is obtained by calculating the ratio of the electric energy stored in the TLS host volume to the total electric energy [41]:

$$F = \frac{\int_{V_{TLS}} \varepsilon_{TLS} \vec{E}^2 d\vec{r}}{\int_V \varepsilon \vec{E}^2 d\vec{r}} \tag{6.1}$$

The results of the simulation are shown in Fig. 6.2. We note the significant increase of the filling factor as the width is reduced.

Meandering Parasitic Capacitance

In this section, we analyze the influence of meandering the nanowire to qualitatively study the role of any geometry dependent parasitic capacitance. For that purpose, we simulate the frequency response and current density of various nanowire resonators using Sonnet *em* microwave simulator. In order to reduce meshing and simulation times, we simulate 100 nm-wide nanowires in a simple step-impedance resonator geometry. We start by simulating a straight nanowire as a reference and then proceed to simulate nanowires in a meandered geometry with a fixed meander length $b = 20\,\mu\text{m}$ while gradually decreasing distance between meanders from $a = 30\,\mu\text{m}$ to 100 nm (see Fig. 6.3).

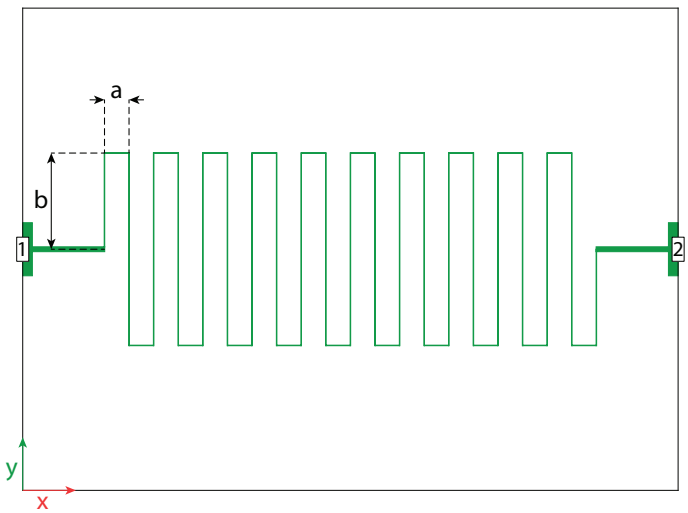

Figure 6.3: Schematic representation of a typical meandered nanowire resonator structure simulated in this section. a and b are the distance between meanders and the meander length respectively. 1 and 2 are the excitation and measurement ports and the black outline represents the grounded edge of the simulation box.

Figs. 6.4 and 6.5 show the normalized current density along the nanowires at the fundamental resonance frequency of the simulated structure. To be clear, for meandered geometries, the current density is not measured as a line cut along the x-axis, but instead the geometry is unwound and the current density is extracted at every point along the nanowire. We observe that for the straight wire and for $a > 5\,\mu\text{m}$, the current density is consistent with the expected $\lambda/2$ mode structure of such a resonator and the characteristic impedance of the nanowire resonator is well-defined to $Z_{nw} = \sqrt{L_{nw}/C_{nw}}$.

Below $a = 5\,\mu\text{m}$, we observe that, as the distance reduces between the meanders, the resonance frequency significantly diverges from the straight nanowire reference value and the current density is severely distorted. This is explained by the increasing influence of parasitic capacitance between each meander. This parasitic capacitance is equivalent to shunting the nanowire with an extra capacitance and lowering its impedance. Moreover,

the structure cannot be treated as a $\lambda/2$ resonator anymore and has therefore no well-defined wave impedance.

Based on these results, for the final devices, depending on the desired total length for the nanowire, we retain designs with 3, 5 or 7 meanders[1] and with an inter-meander distance of respectively 15 µm, 25 µm and 35 µm for which any parasitic capacitance is entirely negligible.

Phase Slip Rate

Phase slips in superinductors are unwanted as they can lead to dissipation [5]. We estimate the phase slip rate $\Gamma_S = E_S/h = E_0/h \exp(-\kappa\bar{w})$ for our device within the phenomenological model for strongly disordered superconductors. Our analysis is similar to that of Peltonen *et al.* [12]. In this model, E_S is the phase slip energy and we have $E_0 = \rho\sqrt{l/\bar{w}}$, where l and $\bar{w}$ are the nanowire length and average width respectively, $\rho = (\hbar/2e)^2/L_k$ represents the superfluid stiffness, $\kappa = \eta\sqrt{\nu_p\rho}$, $\eta \simeq 1$ and $\nu_p = 1/(2e^2 R_N D)$ is the Cooper pair density of states with $D \simeq 0.45\,\mathrm{cm^2\,s^{-1}}$.

For our device parameters ($R_N = 503\,\Omega/\square$, $L_k = 82\,\mathrm{pH}/\square$, $\bar{w} = 40\,\mathrm{nm}$), we find $\Gamma_S \simeq 7 \times 10^{-5}\,\mathrm{Hz}$. This corresponds to an average of one phase slip event every 4 hours, which is entirely negligible.

6.1.3 Practical Considerations and Device Design

Building on the conclusions of the previous section, we fabricate 40 nm wide nanowire superinductors etched in a 20 nm thick NbN thin film using the fabrication process described in section 4.5.

In order to eliminate potential cross talk between microwave feed lines, the final samples contain one single feed line on which up to 23 nanowire superinductors (with an identical coupling but different resonance frequencies) are multiplexed. Arrays of 2 µm × 2 µm flux-trapping holes are added to the ground planes to limit loss due to magnetic vortices [98].

The sample also contains separate DC transport test structures: Hall bar type structures are included to enable transport measurements on both a conventional "slab" of the superconductor and a nanowire of the same 40 nm width as the main device. Pictures of the device are shown in Fig. 6.6.

[1] We define a meander by a 180° turn in the nanowire geometry.

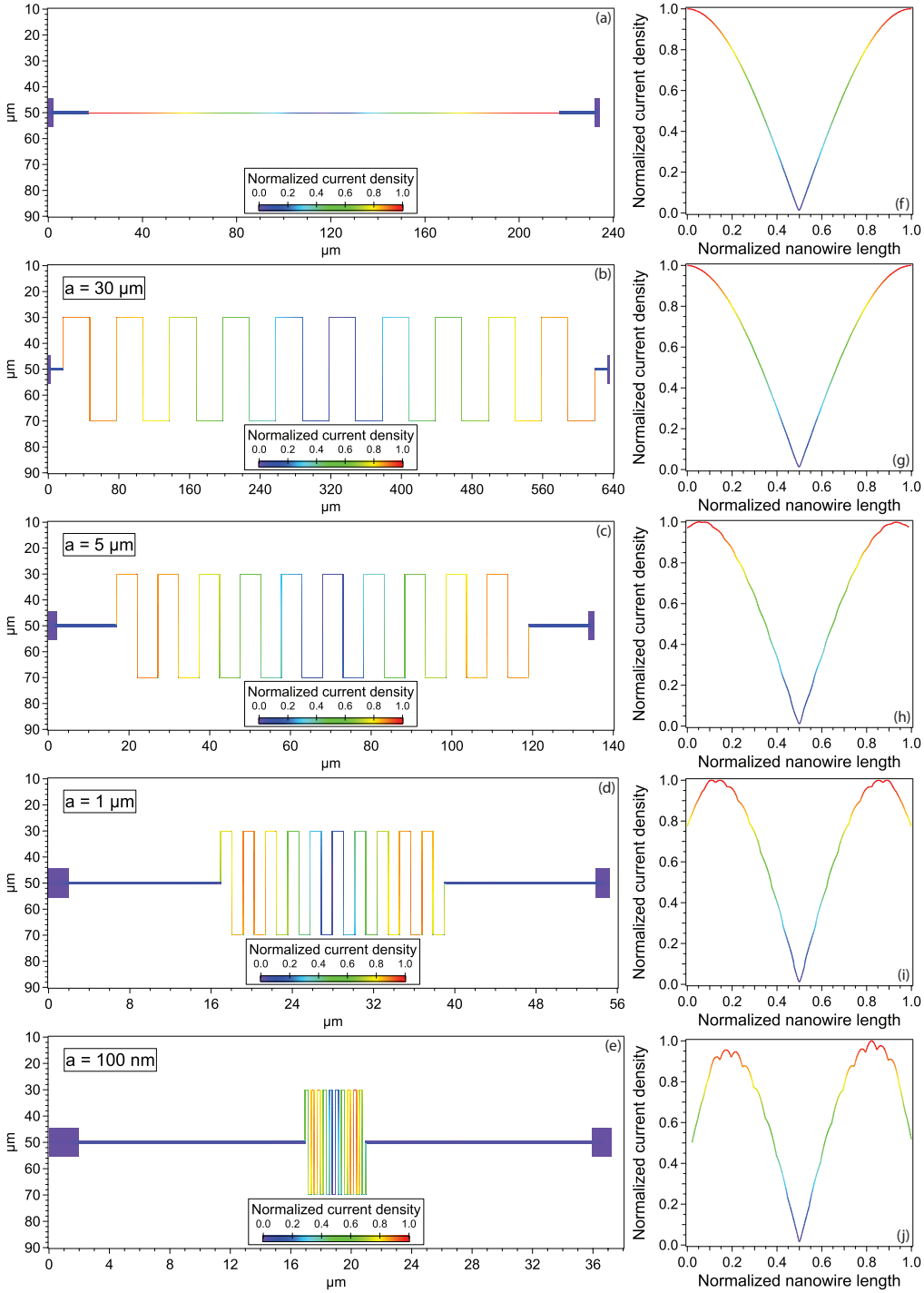

Figure 6.4: **(a-e)** Current density distribution in nanowires at several inter-meander distances. **(f-j)** Corresponding normalized current density along the nanowire.

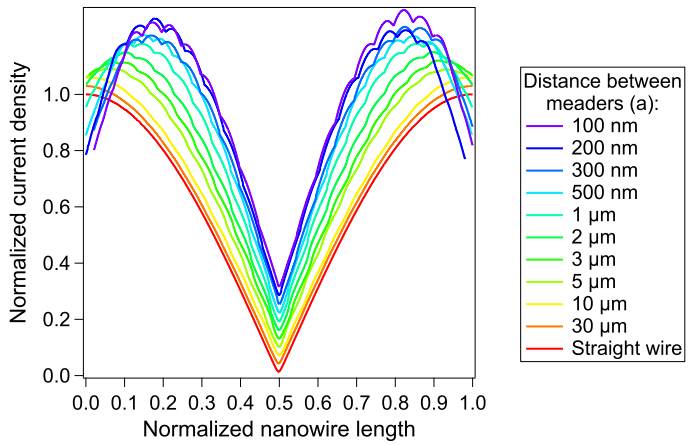

Figure 6.5: Normalized current densities at the fundamental resonance frequencies for all the simulated structures. For clarity, the curves have been offset by 0.03.

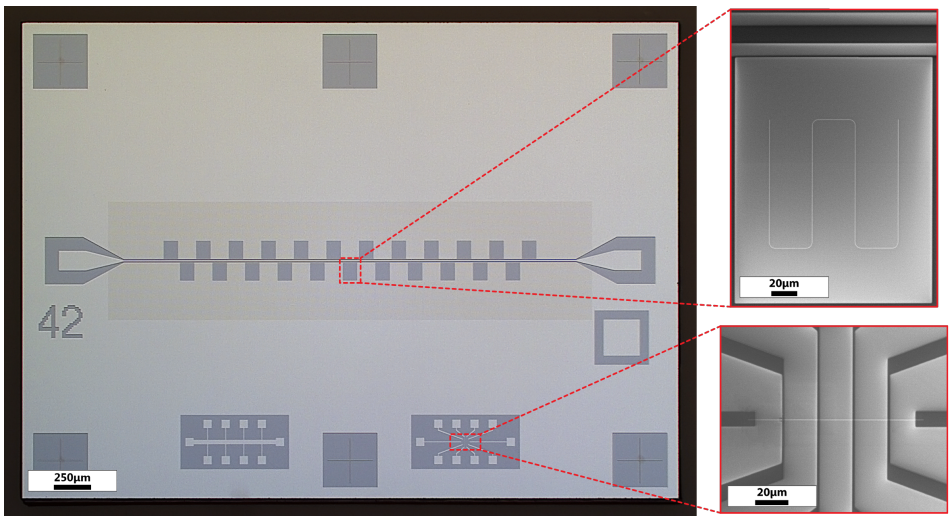

Figure 6.6: **(left)** Optical micrograph of a device used in this work. The dark grey regions correspond to the Si substrate. NbN is shown in light gray. The beige region around the feed line corresponds to the arrays of flux trapping holes opened in the NbN ground plane. **(right)** SEM micrograph of a nanowire superinductor resonator (top) and nanowire Hall bar (bottom). In both cases, the NbN feed line, ground plane and contacts are shown in black, the Si substrate is in gray, and the nanowire is light gray.

6.2 DC Transport Characterization

6.2.1 NbN Thin Film Optimization

In the previous section, we established the need for a highly disordered superconductor to fabricate our devices. This requires careful optimization of the NbN thin film fabrication process with a high level of control of the deposition parameters. In this work, NbN thin films are reactively sputtered (see section 4.3) and several "tuning knobs" are available to adjust the level of disorder in the film: as we already established in the previous chapters, the level of disorder can be tuned by adjusting the thickness of the thin film [99, 100]. Moreover, for a given thickness, the disorder in the film can be further tuned by adjusting the stoichiometry of the film [99]. This is done by adjusting the amount of nitrogen present in the chamber during deposition. This increase in nitrogen content can be regarded as doping: as more and more nitrogen is added to the film, more and more scattering sites are introduced and increase the amount of disorder in the film. Additionally, the choice of substrate is also relevant. Alumina and magnesium oxide have a very small lattice mismatch with NbN and are therefore the substrates of choice for epitaxial NbN depositions. For disordered films, however, it is preferable to use a less favourable substrate such as silicon. Finally, the substrate temperature during deposition plays a role on the level of disorder. Epitaxial films are usually sputtered at a substrate temperature ranging from 600 °C to 800 °C while films deposited at ambient temperature are inherently more disordered [101]. Fig. 6.7 summarizes the properties of NbN thin films deposited on Si substrates for various process parameters.

6.2.2 Transport Characterization

We systematically study the transport properties of our NbN thin films and nanowires using the DC test structures on each device. We measure a wide range of parameters on our films, which allows us to quantify the level of disorder and ensure that the film parameters are consistent with the local dirty limit described in chapter 2. Using a Hall effect measurement at 15 K (where the resistance is maximum, ie. for $R(T) = R_N$), we measure the Hall coefficient R_H of our film, which is calculated from the slope of the transverse resistivity ρ_{xy} against magnetic field. From the Hall coefficient, we get the charge carrier density with $n_n = 1/R_H e$. Using the free electron relations (see chapter 2), we can calculate the key parameters of our film, summarized in table 6.1.

Additionally, we measure the resistance against temperature ($R(T)$) characteristic of the nanowire. Using the models described in section 2.4, we fit the experimental data to extract the normal-state resistance R_N and critical temperature T_c. We then calculate the kinetic inductance contribution with Eq. 2.46. Once again, the values are summarized in table 6.1.

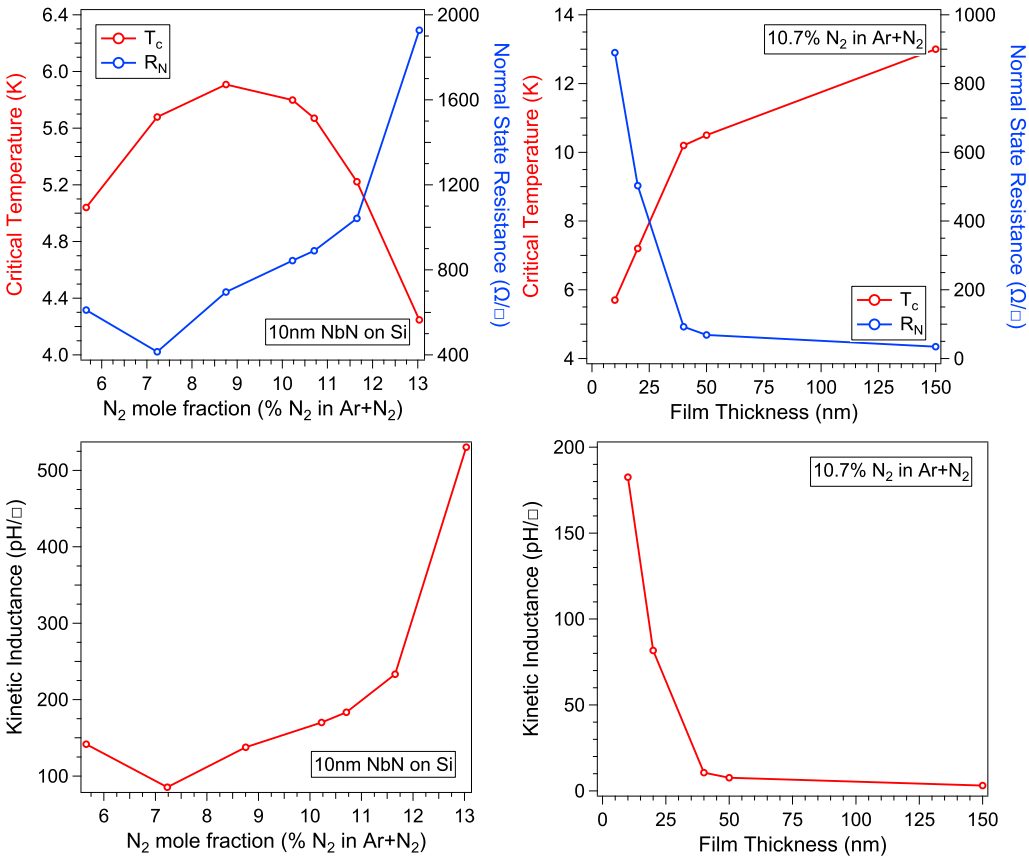

Figure 6.7: **(left)** Critical temperature T_c, normal-state resistance R_N and kinetic inductance L_k for NbN thin films as a function of nitrogen content for a fixed thickness of 10 nm. **(right)** Same parameters for NbN thin films as a function of thickness and at a fixed nitrogen mole fraction of 10.7 %.

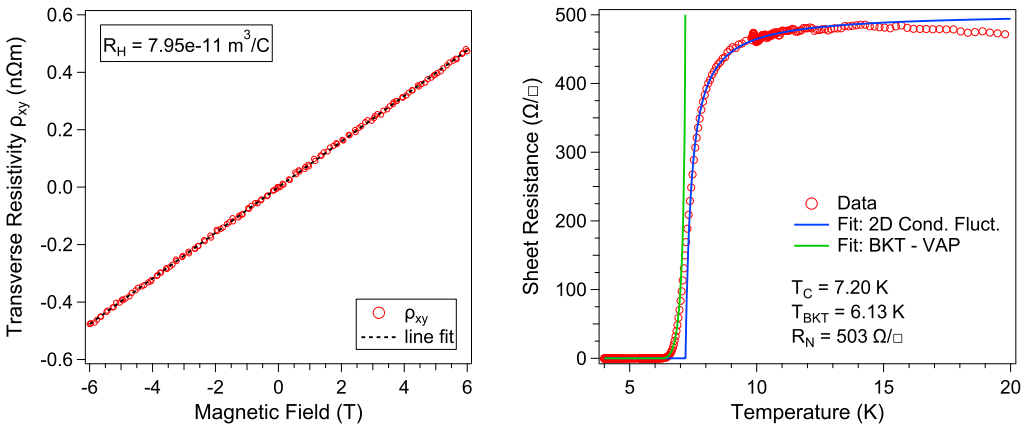

Figure 6.8: **(left)** Hall transverse resistivity as a function of magnetic field of our NbN thin film, measured at $T = 15\,\mathrm{K}$. **(right)** $R(T)$ characteristic of a NbN nanowire. The blue and green lines are fits to Eqs. 2.47 and 2.52 respectively.

Table 6.1: NbN thin film parameters calculated from Hall effect and $R(T)$ measurements.

Parameter name	Symbol	Value
Carrier density	n_n	$7.85 \times 10^{28}\,\mathrm{m}^{-3}$
Fermi wavevector	k_F	$1.32 \times 10^{10}\,\mathrm{m}^{-1}$
Fermi energy	ε_F	$1.07 \times 10^{-18}\,\mathrm{J}$
Fermi velocity	v_F	$1.53 \times 10^{6}\,\mathrm{m\,s}^{-1}$
Electron mean free path	l	103 pm
Coherence length	ξ_0	236 nm
London penetration depth	λ_{dirty}	905 nm
Effective penetration depth	Λ	82 µm
Ioffe-Regel parameter	$k_F l$	1.36
Normal-state resistance	R_N	$503\,\Omega/\square$
Critical temperature	T_c	7.20 K
Kinetic inductance	L_k	$82\,\mathrm{pH}/\square$

6.3 Microwave Characterization

6.3.1 Microwave Response

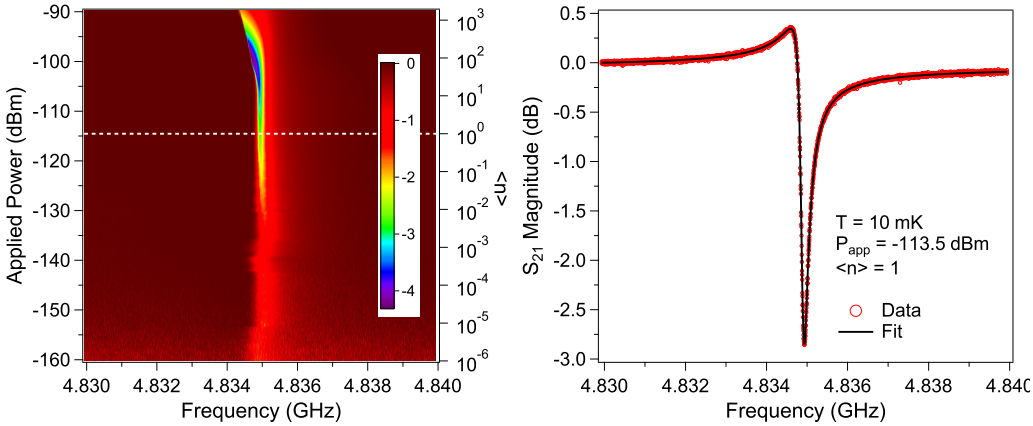

Figure 6.9: **(left)** S_{21} magnitude response across the full range of applied microwave drive for a typical nanowire superinductor. The dashed line corresponds to the single microwave photon regime. **(right)** S_{21} magnitude response of the same device in the single photon regime. The black line is a fit to determine the resonance parameters.

We study the microwave properties of our resonators at 10 mK by measuring the forward transmission S_{21} response at a wide range of excitation powers. We fit the data with the model described in section 3.3.3 to determine the resonator parameters. Due to the large impedance of our resonator, we are able to measure in the low photon regime with a high applied power. Consequently, this enables us to measure, with good signal-to-noise ratio, photon populations two to three orders of magnitude lower than in conventional resonators.

Fig. 6.9 shows the microwave response of a typical nanowire superinductor. For this device, which consists of a 692 µm long nanowire, at an average photon population $\langle n \rangle = 1$, we find a resonance frequency $f_r = 4.835$ GHz and an internal quality factor $Q_i = 2.5 \times 10^4$. We emphasize that the measured resonance frequency is within 1% of the resonance frequency estimated from the simulated capacitance and kinetic inductance obtained from transport measurements. Starting at the dashed line in Fig. 6.9 (left), as we increase power, the resonance frequency does not change until $\langle n \rangle \simeq 10$. From $\langle n \rangle \simeq 10$, as power increases, the frequency decreases until the resonator bifurcates. This is explained by the power dependence of the kinetic inductance, which behaves as a Duffing-like non-linearity [102]. We note that this non-linearity occurs at similar microwave drives as junctions embedded resonators [103, 104].

Starting again at $\langle n \rangle = 1$, as we decrease power, we see the frequency remain approximately constant. Additionally, we see a change in contrast which corresponds to a reduction in

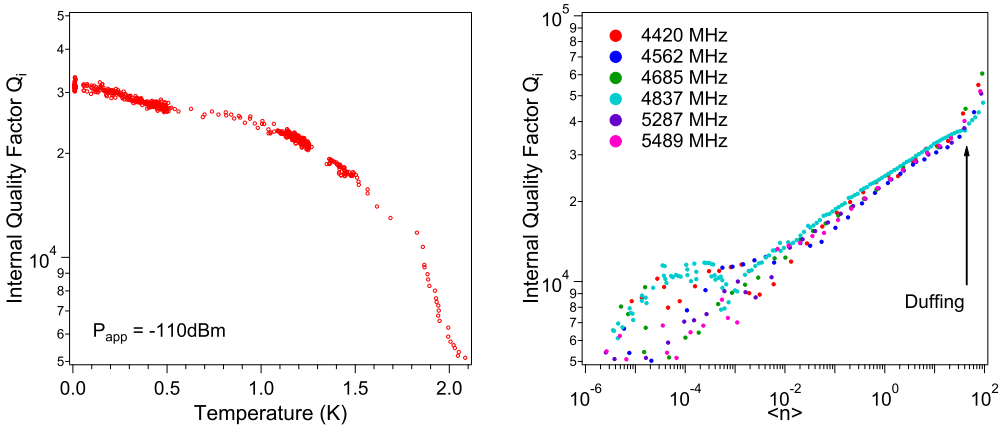

Figure 6.10: **(left)** Plot of the internal quality factor Q_i of a nanowire superinductor resonator as a function of temperature. **(right)** Internal quality factor of various nanowire superinductors.

the magnitude of the resonance dip and is examined in more detail in the next section. We also find that below $\langle n \rangle = 10^{-3}$, the resonator exhibits frequency jitter (see Fig. 6.11), consistent with TLS-induced permittivity changes [75]. This frequency noise results in spectral broadening of the resonance curve.

Additionally, we determine the range of temperatures at which we can operate our device. Fig. 6.10(left) shows a measurement of the internal quality factor Q_i against temperature. We see that from 10 mK to 1.4 K, the quality factor only marginally decreases from 3×10^4 to 2×10^4. We note that this offers a far greater range of operation that aluminium JJA-based superinductors which show significant dissipation above 100 mK [5].

Similar measurements and data analysis were carried out on several nanowire superinductors. We find good reproducibility between resonators and similar internal quality factors as highlighted in Fig. 6.10(right).

6.3.2 Loss Study

In this section, we characterize the losses in our nanowire superinductors. We start by examining the internal quality factor as a function of the applied microwave power (see Fig. 6.11). Between the range of $\langle n \rangle \simeq 10^{-5}$ and $\langle n \rangle \simeq 10^{-3}$, we find that Q_i is approximately constant, with changes in Q_i that are caused by frequency jitter-induced spectral broadening. From $\langle n \rangle \simeq 10^{-3}$, as we increase power, Q_i increases, which is consistent with depolarization of TLS. This effect is magnified in these resonators due to the large impedance which increases sensitivity to fluctuations of the electric field.

In order to fit the data, we first need to independently determine the intrinsic loss tangent $F \tan \delta^i_{TLS}$. For that purpose, we track the frequency changes of the nanowire resonator against temperature using a Pound frequency-locked loop (P-FLL - see section 5.1).

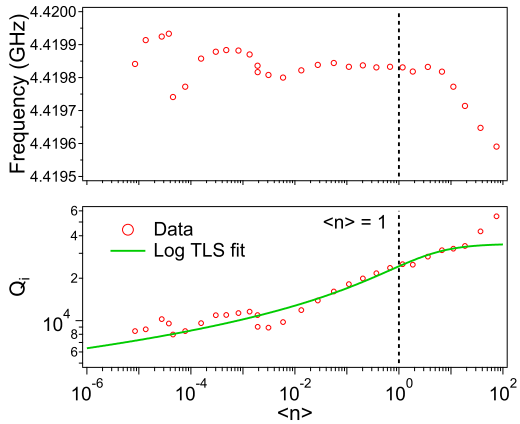

Figure 6.11: Resonant frequency (top) and internal quality factor (bottom) of a typical nanowire resonator as a function of microwave drive. The solid line is a fit to Eq. (3.24). The vertical dashed lines highlight the single microwave photon regime.

Fig. 6.12 shows the changes in resonance frequency against the natural energy scale of the TLS (hf_r/k_BT). We fit the data with Eq. 3.25. Importantly, Eq. (3.25) only fits the TLS contribution but does not fit the temperature-dependent kinetic inductance contribution which occurs below $hf_r/k_BT = 0.1$. Then, we use fitted value of the intrinsic loss tangent $F \tan \delta^i_{TLS}$ to fit the data in Fig. 6.11 to the logarithmic TLS model described in section 3.4.2. The values obtained from both fits are summarized in table 6.2. Most notably, we find values of P_γ between 0.153 and 0.218. As described in section 3.4.2, P_γ is the TLS switching rate ratio, defined by $P_\gamma = 1/\ln(\gamma_{max}/\gamma_{min})$ where γ_{max} and γ_{min} are the maximum and minimum rate of TLS switching respectively. These rates have been measured in the TLS-related charge-noise spectrum of single-electron transistors and were found to extend from $\gamma_{min} \simeq 100\,\text{Hz}$ to $\gamma_{max} \simeq 25\,\text{kHz}$ [105], which corresponds to $P_\gamma = 0.18$. Our fitted values are in good agreement with this estimate and other experimental results [4, 106, 107].

Table 6.2: Nanowire superinductance resonator parameters. $F\delta^i_{TLS}$ is obtained from fits to Eq. (3.25) and P_γ from fits to Eq. (3.24).

NW f_r (MHz)	$F\delta^i_{TLS}$ ($\times 10^{-5}$)	P_γ
4420	4.37	0.195
4562	3.84	0.183
4685	3.53	0.218
4837	4.40	0.153
5285	4.12	0.213

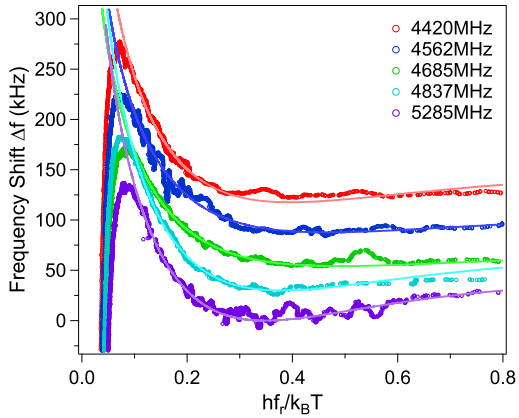

Figure 6.12: Frequency shift as a function of the normalized frequency of all the nanowire superinductor resonators. The solid lines show fits to the theory described by Eq. (3.25). For clarity, the curves have been offset by 30 kHz.

6.3.3 Discussion

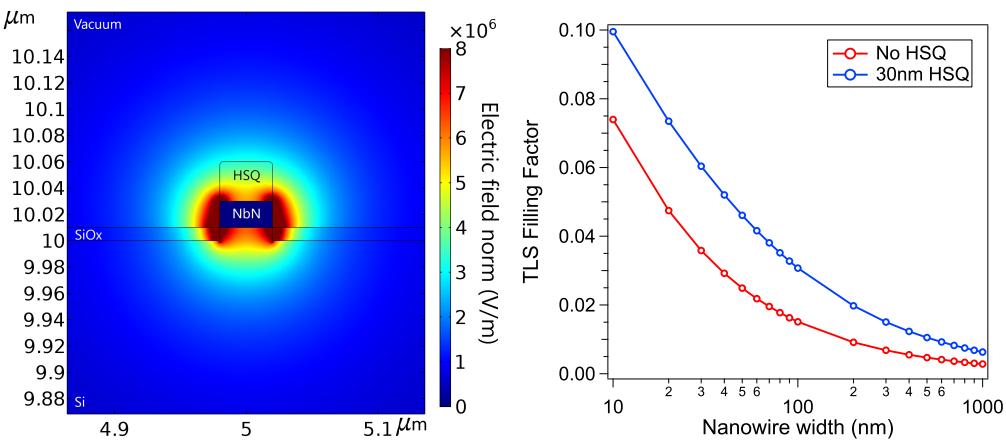

Figure 6.13: **(left)** Magnitude of the electric field for a 40 nm wide nanowire with unetched HSQ on top. **(right)** TLS filling factor for nanowire with (red) and without HSQ (blue) and for widths ranging from 1 µm to 10 nm.

The results shown in the previous sections demonstrate that dissipation in our nanowires is not an intrinsic property of disorder within the film[68, 69] but is instead caused by TLS. This is not surprising as TLS are the predominant source of dissipation and decoherence in a wide variety of quantum devices. We have also shown the role and scaling of the TLS filling factor in our devices, which leads to an unfavorable filling factor for the 40 nm width used here to produce a superinductor. This therefore leads to a much lower Q_i

than is found for wider superconducting resonator geometries.

Additionally, as described in section 4.5, the nanowire lithography relies on the use of a spin-on glass resist (HSQ) which resembles amorphous silicon oxide. Because some HSQ remains unetched atop our nanowires, we suspect this is the dominant source of TLS in our devices. Cross-linked HSQ has a complex structure [108, 109], however, working under the assumption that it can reasonably be modeled by a conventional silicon oxide layer, we have reproduced the simulations of section 6.1.2 to get a qualitative feel for the influence of the HSQ on the filling factor. We model the unetched HSQ as a 30 nm thick silicon oxide layer on top of the nanowire and the filling factor is once again calculated using Eq. 6.1. The results of the simulation are shown in Fig. 6.13. We see that the filling factor is increased by almost a factor of two for the nanowire with HSQ, which qualitatively shows that the non-trivial removal of the HSQ mask should result in a significant improvement in device performance.

Chapter 7

Conclusion and Outlook

In this work, we have fabricated and characterized nanowires made from highly disordered NbN. With an impedance of $6.795\,\mathrm{k}\Omega$ and a single photon quality factor of $Q_i = 2.5 \times 10^4$, our device is the first demonstration a nanowire superinductance.

The quality factor in our nanowire superinductors is comparable to both JJA-based superinductors [5] and the tanh-scaled TLS loss in similar nanowire-resonators [14]. We have analyzed the loss mechanisms in our devices and find TLS to be the dominant cause of loss, which is in contrast to the high rates of dissipation found in other nanowire [12, 67] or strongly disordered thin film devices [68].

We emphasize that demonstrating nanowires losses are "conventional" is a important step forward for all nanowire-based quantum circuits. Therefore, this enables the possibility of long-lived nanowire-based superconducting circuits, such as a nanowire fluxonium qubit [1, 110] or improved phase-slip qubits [12, 67]. These high inductance and high impedance circuits can also be used as photon detectors [15] or for exploring fundamental physics such as Bloch oscillations of charge for metrology applications [111], or for increasing zero-point fluctuations for detection applications [14].

Appendix A

Cleanroom Recipes

A.1 Wafer Cleaning

Wafer cleaning	
1165 Remover	60 °C for 10 min
IPA bath	circulate IPA for 2 min
QDR bath	Rinse in water and blow dry with N_2
HF bath	Dip in 2% HF for 30 s
QDR bath	Rinse in water and blow dry with N_2

A.2 NbN Deposition

NbN Sputtering	
Presputtering	Presputter for 5 min
Sputter	NbN deposition for 27 s at 200 W, 6.7 µbar 83.4 sccm of argon and 10 sccm of nitrogen

A.3 Electron Beam Lithography

PMMA A6 Positive EBL Resist	
Prebake	110 °C for 1 min
Spin PMMA A6	3000 rpm for 1 min, $t_{acc} = 1.5$ s
Bake on hotplate	160 °C for 5 min
Expose pattern	JBX-9300FS or EBPG5200, 100 kV, 800 µC cm^{-2}
Develop	MIBK:IPA 1:3, 5 min
IPA	Rinse in IPA and blow dry with N_2
Descumming	Ash in O_2 plasma at 50 W for 40 s

HSQ Negative EBL Resist

Prebake	60 °C for 1 min
Spin HSQ	5000 rpm for 1 min, $t_{acc} = 1.5$ s
Expose pattern	JBX-9300FS or EBPG5200, 100 kV, 8000 µC cm^{-2}
Develop	MF-319 for 60 s
QDR bath	Rinse in water and blow dry with N_2
Descumming/Hardening	Ash in O_2 plasma at 50 W for 40 s

A.4 Photolithography

S1805 Positive Photoresist

Dehydratation bake	110 °C for 1 min
Spin S1805 resist	3000 rpm for 1 min, $t_{acc} = 1.5$ s
Softbake on hotplate	110 °C for 1 min
Expose pattern	DWL2000 laser writer, focus 10, intensity 75 transmission 100%
Develop	MF-CD-26 for 60 s
QDR bath	Rinse in water and blow dry with N_2
Descumming	Ash in O_2 plasma at 50 W for 40 s

A.5 Etching of NbN

Reactive Ion Etching of NbN

RIE	RIE in Ar:Cl_2 50:4, 20 mTorr, 50 W for 3 min
Water	Immediately rinse in water and blow dry with N_2
Descumming	Ash in O_2 plasma at 50 W for 40 s

A.6 Complete Process Flow

1. Wafer Cleaning

- 1165 remover at 60 °C, IPA, QDR
- 30 s HF and QDR

2. NbN Deposition

- Room temperature sputtering of 20 nm of NbN at 10 sccm nitrogen flow

3. Microwave circuitry

- Dehydratation bake 110°C, Spin PMMA A6 at 3000 rpm, 360 s, bake at 160 °C, 5 min
- Expose in EBL at 800 µC cm^{-2}
- Develop in MIBK:IPA 1:3 for 5 min, rinse in IPA
- Ash 50 W for 40 s
- RIE in Ar:Cl_2 50:4, 20 mTorr, 50 W for 3 min
- Ash 50 W for 40 s
- 1165 remover at 60 °C for 2 min, rinse in IPA, QDR
- Ash 50 W for 40 s

4. Nanowires

- Dehydratation bake 110 °C, Spin HSQ at 5000 rpm, 60 s
- Expose in EBL at 8000 µC cm^{-2}
- Develop in MF-319 for 60 s
- Ash 50 W for 40 s
- Dehydratation bake 110 °C, Spin S1805 at 3000 rpm, 60 s, bake 110 °C, 60 s
- Expose in laser writer, focus 10, intensity 75, transmission 100%
- Develop in MC-CD-26 for 60 s
- Ash 50 W for 40 s
- RIE in Ar:Cl_2 50:4, 20 mTorr, 50 W for 3 min

- Ash 50 W for 40 s
- 1165 remover at 60°C for 2 min, rinse in IPA, QDR

Appendix B

Waveguide Impedance Calculation by Conformal Mapping

In this section, we present the equations used to simulate the characteristic impedance of a coplanar waveguide (CPW). In order to simulate the inductance and capacitance per unit length, the conformal mapping method is used [112]. The electric field lines between the center conductor and the ground planes of the CPW are mapped to the lines of the electric field from a parallel plate capacitor.

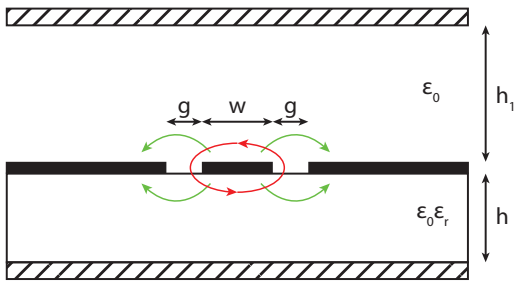

Figure B.1: Cross section of the coplanar waveguide geometry. The superconducting metal (thick black layer) is placed on top of a substrate with effective dielectric constant ε_r. The device is placed in vacuum and is surrounded by top and bottom enclosures. h denotes the thickness of the substrate and h_1 the distance to the top cover. The electric and magnetig field lines are shown respectively in green and red.

We first calculate C_{vac} and C_1, the capacitance contributions of the vacuum and of the substrate

$$C_{vac} = 2\varepsilon_0 \left[\frac{K(k_3)}{K(k_3')} + \frac{K(k_4)}{K(k_4')}\right] \tag{B.1}$$

$$C_1 = 2\varepsilon_0(\varepsilon_r - 1)\frac{K(k_3)}{K(k_3')} \tag{B.2}$$

where ε_0 and ε_r are the vacuum and relative permitivity respectively, and K the complete elliptic integral of the first kind. k_3, k_3' k_4 and k_4' are defined by

$$k_3 = \frac{\tanh(\pi w/4h)}{\tanh(\pi(w+2g)/4h)} \qquad k_3' = \sqrt{1-k_3^2} \tag{B.3}$$

$$k_4 = \frac{\tanh(\pi w/4h_1)}{\tanh(\pi(w+2g)/4h_1)} \qquad k_4' = \sqrt{1-k_4^2} \tag{B.4}$$

This allows us to define an effective dielectric constant:

$$\varepsilon_{eff} = 1 + q_2(\varepsilon_r - 1) \tag{B.5}$$

where q_2 is a partial filling factors defined by

$$q_2 = \frac{K(k_3)}{K(k_3')}\left[\frac{K(k_3)}{K(k_3')} + \frac{K(k_4)}{K(k_4')}\right]^{-1} \tag{B.6}$$

This enables us to express the phase velocity and characteristic impedance in terms of ε_{eff}:

$$v_{ph} = \frac{c}{\sqrt{\varepsilon_{eff}}} \tag{B.7}$$

$$Z_0 = \frac{1}{cC_{vac}\sqrt{\varepsilon_{eff}}} = \frac{60\pi}{\sqrt{\varepsilon_{eff}}}\left[\frac{K(k_3)}{K(k_3')} + \frac{K(k_4)}{K(k_4')}\right]^{-1} \tag{B.8}$$

Finally, we can express the inductance and capacitance per unit length of the CPW:

$$L_{CPW} = \frac{\mu_0}{2}\left[\frac{K(k_3)}{K(k_3')} + \frac{K(k_4)}{K(k_4')}\right]^{-1} \tag{B.9}$$

$$C_{CPW} = 2\varepsilon_0\varepsilon_{eff}\left[\frac{K(k_3)}{K(k_3')} + \frac{K(k_4)}{K(k_4')}\right] \tag{B.10}$$

References

1. Pop, I. M. *et al.* "Coherent suppression of electromagnetic dissipation due to superconducting quasiparticles". *Nature* **508,** 369+ (Apr. 2014).
2. Yan, F. *et al.* "The flux qubit revisited to enhance coherence and reproducibility". *Nat. Commun.* **7,** 12964 (Nov. 2016).
3. De Graaf, S. E. *et al.* "Direct Identification of Dilute Surface Spins on Al_2O_3: Origin of Flux Noise in Quantum Circuits". *Phys. Rev. Lett.* **118,** 057703 (5 Jan. 2017).
4. De Graaf, S. E. *et al.* "Suppression of low-frequency charge noise in superconducting resonators by surface spin desorption". *Nat. Commun.* **9,** 1143 (Mar. 2018).
5. Masluk, N. A., Pop, I. M., Kamal, A., Minev, Z. K. & Devoret, M. H. "Microwave Characterization of Josephson Junction Arrays: Implementing a Low Loss Superinductance". *Phys. Rev. Lett.* **109,** 137002 (13 Sept. 2012).
6. Bell, M. T., Sadovskyy, I. A., Ioffe, L. B., Kitaev, A. Y. & Gershenson, M. E. "Quantum Superinductor with Tunable Nonlinearity". *Phys. Rev. Lett.* **109,** 137003 (13 Sept. 2012).
7. Manucharyan, V. E., Koch, J., Glazman, L. I. & Devoret, M. H. "Fluxonium: Single Cooper-Pair Circuit Free of Charge Offsets". *Science* **326,** 113–116 (2009).
8. Koch, J., Manucharyan, V., Devoret, M. H. & Glazman, L. I. "Charging Effects in the Inductively Shunted Josephson Junction". *Phys. Rev. Lett.* **103,** 217004 (21 Nov. 2009).
9. Kou, A. *et al.* "Fluxonium-Based Artificial Molecule with a Tunable Magnetic Moment". *Phys. Rev. X* **7,** 031037 (3 Aug. 2017).
10. Lin, Y.-H. *et al.* "Demonstration of Protection of a Superconducting Qubit from Energy Decay". *Phys. Rev. Lett.* **120,** 150503 (15 Apr. 2018).
11. Belkin, A., Brenner, M., Aref, T., Ku, J. & Bezryadin, A. "Little–Parks oscillations at low temperatures: Gigahertz resonator method". *Appl. Phys. Lett.* **98,** 242504 (2011).
12. Peltonen, J. T. *et al.* "Coherent flux tunneling through NbN nanowires". *Phys. Rev. B* **88,** 220506 (22 Dec. 2013).
13. Burnett, J., Sagar, J., Kennedy, O. W., Warburton, P. A. & Fenton, J. C. "Low-Loss Superconducting Nanowire Circuits Using a Neon Focused Ion Beam". *Phys. Rev. Appl.* **8,** 014039 (1 July 2017).
14. Samkharadze, N. *et al.* "High-kinetic-inductance superconducting nanowire resonators for circuit QED in a magnetic field". *Phys. Rev. Appl.* **5,** 044004 (2016).

15. Gao, J. *et al.* "Experimental evidence for a surface distribution of two-level systems in superconducting lithographed microwave resonators". *Appl. Phys. Lett.* **92,** 152505 (2008).

16. Onnes, K. H. "The Superconductivity of Mercury". *Comm. Phys. Lab. Univ. Leiden* **251** (1911).

17. Meissner, W. & Ochsenfeld, R. "Ein neuer Effekt bei Eintritt der Supraleitfähigkeit". *Naturwissenschaften* **21,** 787–788 (44 Nov. 1933).

18. Rjabinin, J. N. & Shubnikov, L. W. "Magnetic Properties and Critical Currents of Supra-conducting Alloys". *Nature* **135,** 581 (Apr. 1935).

19. Gorter, C. J. & Casimir, H. "On superconductivity". *Physica* **1,** 306–320 (1934).

20. London, F. & London, H. "The electromagnetic equations of the superconductor". *Proc. Royal Soc. Lond. A* **149,** 71–88 (1935).

21. Ginzburg, V. L. & Landau, L. D. "On the Theory of superconductivity". *Zh. Eksp. Teor. Fiz.* **20,** 1064–1082 (1950).

22. Abrikosov, A. A. "On the Magnetic Properties of Superconductors of the Second Group". *JETP* **5,** 1174 (6 1957).

23. Gor'kov, L. P. "Microscopic Derivation of the Ginzburg-Landau Equations in the Theory of Superconductivity". *JETP* **9,** 1364 (6 1959).

24. Bardeen, J., Cooper, L. N. & Schrieffer, J. "Theory of superconductivity". *Phys. Rev.* **108,** 1175–1204 (5 Dec. 1957).

25. Mattis, D. C. & Bardeen, J. "Theory of the Anomalous Skin Effect in Normal and Superconducting Metals". *Phys. Rev.* **111,** 412–417 (2 July 1958).

26. Drude, P. "Zur Elektronentheorie der Metalle". *Ann. Phys.* **306,** 566–613.

27. Drude, P. "Zur Elektronentheorie der Metalle; II. Teil. Galvanomagnetische und thermomagnetische Effecte". *Ann. Phys.* **308,** 369–402.

28. Ashcroft, N. W. & Mermin, N. D. *Solid State Physics* (Saunders College Publishing, 1976).

29. Sommerfeld, A. & Frank, N. H. "The Statistical theory of thermoelectric, galvano- and thermomagnetic phenomena in metals". *Rev. Mod. Phys.* **3,** 1–42 (1 Jan. 1931).

30. Cooper, L. N. "Bound Electron Pairs in a Degenerate Fermi Gas". *Phys. Rev.* **104,** 1189–1190 (4 Nov. 1956).

31. Mühlschlegel, B. "Die thermodynamischen Funktionen des Supraleiters". *Z. Phys.* **155,** 313–327 (June 1959).

32. Romestain, R. *et al.* "Fabrication of a superconducting niobium nitride hot electron bolometer for single-photon counting". *New J. Phys.* **6,** 129 (2004).

33. Thouless, D. J. “Strong-Coupling Limit in the Theory of Superconductivity”. *Phys. Rev.* **117,** 1256–1260 (5 Mar. 1960).

34. Dressel, M. “Electrodynamics of Metallic Superconductors”. *Adv. Cond. Matter Phys.* **2013,** 104379 (2013).

35. Ioffe, A. F. & Regel, A. R. “Non-crystalline, amorphous, and liquid electronic semiconductors”. *Prog. Semicond.* **4,** 237–291 (1960).

36. Anderson, P. W. “Absence of Diffusion in Certain Random Lattices”. *Phys. Rev.* **109,** 1492–1505 (5 Mar. 1958).

37. Dynes, R. C., Garno, J. P. & Rowell, J. M. “Two-Dimensional Electrical Conductivity in Quench-Condensed Metal Films”. *Phys. Rev. Lett.* **40,** 479–482 (7 Feb. 1978).

38. Tinkham, M. *Introduction to Superconductivity* (Dover Books, 2004).

39. Pearl, J. “Current Distribution in Superconducting Films Carrying Quantized Fluxoids”. *Appl. Phys. Lett.* **5,** 65–66 (1964).

40. Doyle, S. *Lumped Element Kinetic Inductance Detectors.* PhD thesis (University of Cardiff, 2008).

41. Gao, J. *The Physics of Superconducting Microwave Resonators.* PhD thesis (California Institute of Technology, 2008).

42. Bergmann, G. “Physical interpretation of weak localization: A time-of-flight experiment with conduction electrons”. *Phys. Rev. B* **28,** 2914–2920 (6 July 1983).

43. Berezinskii, V. L. “Destruction of Long-range Order in One-dimensional and Two-dimensional Systems Possessing a Continuous Symmetry Group. II. Quantum Systems”. *Zh. Eksp. Teor. Fiz.* **61,** 1144 (3 1972).

44. Kosterlitz, J. M. & Thouless, D. J. “Ordering, metastability and phase transitions in two-dimensional systems”. *J. Phys. C: Solid State* **6,** 1181 (1973).

45. Nelson, D. R. & Kosterlitz, J. M. “Universal Jump in the Superfluid Density of Two-Dimensional Superfluids”. *Phys. Rev. Lett.* **39,** 1201–1205 (19 Nov. 1977).

46. Beasley, M. R., Mooij, J. E. & Orlando, T. P. “Possibility of Vortex-Antivortex Pair Dissociation in Two-Dimensional Superconductors”. *Phys. Rev. Lett.* **42,** 1165–1168 (17 Apr. 1979).

47. Hebard, A. F. & Fiory, A. T. “Critical-Exponent Measurements of a Two-Dimensional Superconductor”. *Phys. Rev. Lett.* **50,** 1603–1606 (20 May 1983).

48. Mooij, J. E. *Percolation, Localization and Superconductivity* (Plenum Press, 1984).

49. Blais, A., Huang, R.-S., Wallraff, A., Girvin, S. M. & Schoelkopf, R. J. “Cavity quantum electrodynamics for superconducting electrical circuits: An architecture for quantum computation”. *Phys. Rev. A* **69,** 062320 (6 June 2004).

50. Pozar, D. M. *Microwave Engineering 3rd edition* (John Wiley & Sons, New York, 2005).

51. Visser, H. J. *Antenna Theory and Applications* (John Wiley & Sons, New York, 2012).

52. Wen, C. P. "Coplanar Waveguide: A Surface Strip Transmission Line Suitable for Nonreciprocal Gyromagnetic Device Applications". *IEEE T. Microw. Theory* **17,** 1087–1090 (Dec. 1969).

53. Kajfez, D. & Guillon, P. *Dielectric Resonators* (SciTec, 1998).

54. Komatsu, Y. & Murakami, Y. "Coupling Coefficient Between Microstrip Line and Dielectric Resonator". *IEEE T. Microw. Theory* **31,** 34–40 (Jan. 1983).

55. Barends, R. *Photon-detecting superconducting resonators.* PhD thesis (TU Delft, 2009).

56. Khalil, M. S., Stoutimore, M. J. A., Wellstood, F. C. & Osborn, K. D. "An analysis method for asymmetric resonator transmission applied to superconducting devices". *J. Appl. Phys.* **111,** 054510 (2012).

57. Probst, S., Song, F. B., Bushev, P. A., Ustinov, A. V. & Weides, M. "Efficient and robust analysis of complex scattering data under noise in microwave resonators". *Rev. Sci. Instrum.* **86,** 024706 (2015).

58. Mazin, B. A. *Microwave kinetic inductance detectors.* PhD thesis (California Institute of Technology, 2004).

59. Barends, R. *et al.* "Minimizing quasiparticle generation from stray infrared light in superconducting quantum circuits". *Appl. Phys. Lett.* **99,** 113507 (2011).

60. Córcoles, A. D. *et al.* "Protecting superconducting qubits from radiation". *Appl. Phys. Lett.* **99,** 181906 (2011).

61. Levenson-Falk, E. M., Kos, F., Vijay, R., Glazman, L. & Siddiqi, I. "Single-Quasiparticle Trapping in Aluminum Nanobridge Josephson Junctions". *Phys. Rev. Lett.* **112,** 047002 (4 Dec. 2014).

62. Nsanzineza, I. & Plourde, B. L. T. "Trapping a Single Vortex and Reducing Quasiparticles in a Superconducting Resonator". *Phys. Rev. Lett.* **113,** 117002 (11 Sept. 2014).

63. Wang, C. *et al.* "Measurement and control of quasiparticle dynamics in a superconducting qubit". *Nat. Commun.* **5,** 5836 (Dec. 2014).

64. Janvier, C. *et al.* "Coherent manipulation of Andreev states in superconducting atomic contacts". *Science* **349,** 1199–1202 (2015).

65. Gustavsson, S. *et al.* "Suppressing relaxation in superconducting qubits by quasiparticle pumping". *Science* **354,** 1573–1577 (2016).

66. Grünhaupt, L. *et al.* "Quasiparticle dynamics in granular aluminum close to the superconductor to insulator transition". *arXiv preprint,* 0902.0885 (2018).

67. Astafiev, O. *et al.* "Coherent quantum phase slip". *Nature* **484,** 355–358 (2012).

68. Coumou, P. *et al.* "Microwave properties of superconducting atomic-layer deposited TiN films". *IEEE T. Appl. Supercon.* **23,** 7500404–7500404 (2013).

69. Feigel'man, M. V. & Ioffe, L. B. "Microwave Properties of Superconductors Close to the Superconductor-Insulator Transition". *Phys. Rev. Lett.* **120,** 037004 (3 Jan. 2018).

70. O'Connell, A. D. *et al.* "Microwave dielectric loss at single photon energies and millikelvin temperatures". *Appl. Phys. Lett.* **92,** 112903 (2008).

71. Macha, P. *et al.* "Losses in coplanar waveguide resonators at millikelvin temperatures". *Appl. Phys. Lett.* **96,** 062503 (2010).

72. Lindström, T., Healey, J. E., Colclough, M. S., Muirhead, C. M. & Tzalenchuk, A. Y. "Properties of superconducting planar resonators at millikelvin temperatures". *Phys. Rev. B* **80,** 132501 (13 Oct. 2009).

73. Grabovskij, G. J., Peichl, T., Lisenfeld, J., Weiss, G. & Ustinov, A. V. "Strain Tuning of Individual Atomic Tunneling Systems Detected by a Superconducting Qubit". *Science* **338,** 232–234 (2012).

74. Lisenfeld, J. *et al.* "Observation of directly interacting coherent two-level systems in an amorphous material". *Nat. Commun.* **6,** 6182 (Feb. 2015).

75. Burnett, J. *et al.* "Evidence for interacting two-level systems from the 1/f noise of a superconducting resonator". *Nat. Commun.* **5,** 4119 (June 2014).

76. Faoro, L. & Ioffe, L. B. "Interacting tunneling model for two-level systems in amorphous materials and its predictions for their dephasing and noise in superconducting microresonators". *Phys. Rev. B* **91,** 014201 (1 Jan. 2015).

77. Abouzahra, M. D. & Lewin, L. "Radiation from Microstrip Discontinuities". *IEEE T. Micro. Theory* **27,** 722–723 (Aug. 1979).

78. Hurter, F. & Driffield, V. C. "Photochemical Investigations and a New Method of Determination of the Sensitiveness of Photographic Plates". *Jour. Soc. Chem. Ind.* 455–469 (1890).

79. Ziger, D. H. & Mack, C. A. "Generalized approach toward modeling resist performance". *AIChE Journal* **37,** 1863–1874 (1991).

80. Mack, C. A., Legband, D. A. & Jug, S. "Data analysis for photolithography". *Microelectron. Eng.* **46,** 65–68 (1999).

81. De Lucas, N. C., Netto-Ferreira, J. C., Andraos, J. & Scaiano, J. C. "Nucleophilicity toward Ketenes: Rate Constants for Addition of Amines to Aryl Ketenes in Acetonitrile Solution". *J. Org. Chem.* **66.** PMID: 11463250, 5016–5021 (2001).

82. Chen, Y., Yang, H. & Cui, Z. "Effects of developing conditions on the contrast and sensitivity of hydrogen silsesquioxane". *Microelect. Eng.* **83,** 1119–1123 (2006).

83. Yang, H., Jin, A., Luo, Q. & Gu, C. "Comparative study of e-beam resist processes at different development temperature". *Microelect. Eng.* **84,** 1109–1112 (2007).

84. Tavakkoli, A., Piramanayagam, S. N., Ranjbar, M., Sbiaa, R. & Chong, T. C. "Path to achieve sub-10-nm half-pitch using electron beam lithography". *J. Vac. Sci. Technol.* **29,** 011035 (2011).

85. Grigorescu, A. E. & Hagen, C. W. "Resists for sub-20-nm electron beam lithography with a focus on HSQ: state of the art". *Nanotechnology* **20,** 292001 (2009).

86. Namatsu, H., Yamaguchi, T., Nagase, M., Yamazaki, K. & Kurihara, K. "Nano-patterning of a hydrogen silsesquioxane resist with reduced linewidth fluctuations". *Microelect. Eng.* **41-42.** International Conference on Micro- and Nanofarbication, 331–334 (1998).

87. Mohammad, M., Dew, S., Evoy, S. & Stepanova, M. "Fabrication of sub-10nm silicon carbon nitride resonators using a hydrogen silsesquioxane mask patterned by electron beam lithography". *Microelect. Eng.* **88,** 2338–2341 (2011).

88. ECHA. *NMP as a substrance of very high concern because of its CMR properties*. `https://echa.europa.eu/documents/10162/1c4e3474-34ee-4c15-aaef-dafd1cb47779` (2011).

89. Mack, C. *Fundamental Principles of Optical Lithography: The Science of Microfabrication* (John Wiley & Sons, Nov. 2007).

90. Campbell, S. A. *The science and engineering of microelectronic fabrication* 2nd (Oxford University Press, 2001).

91. De Broglie, L. *Recherches sur la théorie des quanta.* PhD thesis (Ann. Phys. (Paris), 1924).

92. Pound, R. V. "Electronic Frequency Stabilization of Microwave Oscillators". *Rev. Sci. Instrum.* **17,** 490–505 (1946).

93. Black, E. D. "An introduction to Pound–Drever–Hall laser frequency stabilization". *Am. J. Phys.* **69,** 79–87 (2001).

94. Lindström, T., Burnett, J., Oxborrow, M. & Tzalenchuk, A. Y. "Pound-locking for characterization of superconducting microresonators". *Rev. Sci. Instrum.* **82,** 104706 (2011).

95. De Graaf, S. E., Danilov, A. V., Adamyan, A., Bauch, T. & Kubatkin, S. E. "Magnetic field resilient superconducting fractal resonators for coupling to free spins". *J. Appl. Phys.* **112,** 123905 (2012).

96. Ivry, Y. *et al.* "Universal scaling of the critical temperature for thin films near the superconducting-to-insulating transition". *Phys. Rev. B* **90,** 214515 (21 Dec. 2014).

97. Mohan, S. S., del Mar Hershenson, M., Boyd, S. P. & Lee, T. H. "Simple accurate expressions for planar spiral inductances". *IEEE J. Solid-St. Circ.* **34,** 1419–1424 (Nov. 1999).

98. Chiaro, B. *et al.* "Dielectric surface loss in superconducting resonators with flux-trapping holes". *Supercond. Sci. Technol.* **29,** 104006 (Aug. 2016).

99. Hossain, M. S., Yoshida, K., Kudo, K., Enpuku, K. & Yamafuji, K. "Enlargement of Kinetic Inductance of NbN Superconducting Thin Films for Device Applications". *Jpn. J. Appl. Phys.* **31,** 1033 (1992).

100. Kang, L. *et al.* "Suppression of superconductivity in epitaxial NbN ultrathin films". *J. Appl. Phys.* **109,** 033908 (2011).

101. Krause, S. *et al.* "Ambient Temperature Growth of Mono- and Polycrystalline NbN Nanofilms and Their Surface and Composition Analysis". *IEEE Trans. Appl. Supercond.* **26,** 1–5 (Apr. 2016).

102. Swenson, L. J. *et al.* "Operation of a titanium nitride superconducting microresonator detector in the nonlinear regime". *J. Appl. Phys.* **113,** 104501 (2013).

103. Osborn, K. D., Strong, J. A., Sirois, A. J. & Simmonds, R. W. "Frequency-Tunable Josephson Junction Resonator for Quantum Computing". *IEEE T. Appl. Supercond.* **17,** 166–168 (June 2007).

104. Krantz, P. *et al.* "Investigation of nonlinear effects in Josephson parametric oscillators used in circuit quantum electrodynamics". *New J. Phys.* **15,** 105002 (2013).

105. Kafanov, S., Brenning, H., Duty, T. & Delsing, P. "Charge noise in single-electron transistors and charge qubits may be caused by metallic grains". *Phys. Rev. B* **78,** 125411 (12 Sept. 2008).

106. Burnett, J., Faoro, L. & Lindström, T. "Analysis of high quality superconducting resonators: consequences for TLS properties in amorphous oxides". *Supercond. Sci. Tech.* **29,** 044008 (2016).

107. Kirsh, N., Svetitsky, E., Burin, A. L., Schechter, M. & Katz, N. "Revealing the nonlinear response of a tunneling two-level system ensemble using coupled modes". *Phys. Rev. Mat.* **1,** 012601 (1 June 2017).

108. Chung, S.-W., Shin, J.-H., Park, N.-H. & Park, J. W. "Dielectric Properties of Hydrogen Silsesquioxane Films Degraded by Heat and Plasma Treatment". *Jpn. J. Appl. Phys.* **38,** 5214 (1999).

109. Qianghua, Y., Guiqin, Y. & Zhaoyuan, N. "Effect of Oxygen Plasma on Low Dielectric Constant HSQ (Hydrogensilsesquioxane) Films". *Plasma Sci. Technol* **15,** 86 (Jan. 2013).

110. Kerman, A. J. "Metastable Superconducting Qubit". *Phys. Rev. Lett.* **104,** 027002 (2 Jan. 2010).

111. Guichard, W. & Hekking, F. W. J. "Phase-charge duality in Josephson junction circuits: Role of inertia and effect of microwave irradiation". *Phys. Rev. B* **81,** 064508 (6 Feb. 2010).

112. Rainee, N. S. *Coplanar Waveguide Circuits, Components and Systems* (John Wiley & Sons, New York, 2001).